NONLINEAR STEADY AND UNSTEADY AERODYNAMICS OF WINGS AND WING-BODY-COMBINATIONS

by

ESSAM H. ATTA

Dissertation submitted to the Graduate Faculty of the
Virginia Polytechnic Institute and State Univeristy
in partial fulfillment of the requirements for the degree of
DOCTOR OF PHILOSOPHY
in
Engineering Science and Mechanics

APPROVED:

Ali H. Nayfeh
A. H. Nayfeh, Chairman

Osama A. Kandil
O. A. Kandil, Co-Chairman

D. T. Mook

John E. Kaiser
J. E. Kaiser

Kenneth B. Hansgen
K. B. Hansgen

May, 1978

Blacksburg, Virginia

ACKNOWLEDGEMENTS

The auther would like to thank his committee members, Drs. A. H. Nayfeh, O. A. Kandil, D. T. Mook, J. E. Kaiser and K. B. Hansgen for their contribution to his education and for their help during the course of this research. Thanks also are due to Ms. Janet Bryant for and excellent typing job.

This research was sponsored by the NASA-Langley Research Center under Grant NSG 1262 and by the U.S. Army Research Center under Grant DAAG 29-76-G-0034.

TABLE OF CONTENTS

LIST OF FIGURES

PAGE

PAGE

PAGE

CHAPTER I

INTRODUCTION AND LITERATURE REVIEW

1.1 Introduction

Over the years, high angle-of-attack aerodynamics has become increasingly important for modern aircraft, especially those designed for transonic and supersonic flight which requires the use of slim bodies combined with delta, arrow or other highly swept wings as in Fig. 1. The advent of these aircraft makes it mandatory to predict the low-speed aerodynamic characteristics in take-off, approach and landing as well as in any flight manouvers. At the same time the search for improved missile performance often requires their operation at high angles of attack. In addition flight disturbances of various kinds may cause a missile to inadvertently reach a high angle of attack. Moreover, some missiles such as the cruise missiles (Fig. 1) operate subsonically during their whole range. The prediction of the flight characteristics of these configurations (aircrafts and missiles) requires not only a knowledge of the steady aerodynamic characteristics but also the time-dependent aerodynamic characteristics as well. The latter are of vital importance in flutter and stability analysis.

A principle distinguishing feature of high angle-of-attack aerodynamics is that the lift and pitching moment are no longer linear functions of the angle of attack (Fig. 2). This is attributed to the separation of the flow from the upper side of the body (fuselage, missile body) and from the edges of the lifting surfaces (wing, canard,

tail surface); in this manner, vortex sheets that roll up into strong vortices are formed (Fig. 3) and induce the nonlinear behaviour.

The purpose of this work is to develop reliable techniques to predict the aerodynmaic loads, steady or unsteady, symmetric or asymmetric, for wings, bodies and wing-body combinations at low Mach numbers in the nonlinear range of the angle of attack. Only the delta planform will be considered because it is of primary interest in modern aerodynamics for its flight properties, which include a fairly smooth transition from the subsonic to the supersonic flight regime. Furthermore, the flat-plate delta wing has been more amenable to theoretical considerations and consequently much of the recent research has been directed to the delta-type geometries. The delta wing configuration also demonstrates most of the characteristics of the vortex flow near the wing, and logically it will lead to extensions to more complex planforms.

1.2 Literature Review

The literature review is divided into three sub-sections: longitudinal motions of delta wings, general motions of delta wings and symmetrical motions of wing-body combinations.

1.2.1 Longitudinal Motions of Delta Wings

This section is concerned only with unsteady flows. Comprehensive reviews of steady flows can be found in Refs. 1-5.

At present, several methods exist to treat unsteady incompressible, inviscid, three-dimensional flows. Generally, they can be classified

into the kernel-function approach and the discrete-element approach. They are considered in order.

Kernel-Function Approach

The kernel-function approach is developed for both subsonic and supersonic speeds. It begins with an integral equation relating the unknown pressure distribution ΔC_p to the prescribed normal velocity V_n of the lifting surface as

$$\frac{V_n}{U_\infty}(x,y) = \int_A \Delta C_p(x',y',t)K(x - x', y - y',t)dx'dy' \qquad (1)$$

Since the pressure distribution appears implicitly in Eq. (1), it is expressed in terms of a series of preselected loading functions, thereby reducing the problem to the determination of the unknown coefficients in the series expansion. A solution is obtained by satisfying the tangency condition at just as many points on the lifting surface as there are unknown coefficients (i.e., collocation procedure). Appreciable gain in accuracy is achieved by choosing functons that allow an adequate loading representation, especially near the edges. This approach was used extensively by many researchers[6-13]. However, it is restricted to the linear regime (nonlinear effects of the shape of the wakes are ignored and an approximate geometry is prescribed), and it can handle only small oscillations.

Discrete-Element Approach

A large number of methods exists under this category. In the doublet-lattice method developed by Giesing, Kalman and Rodden[14-16],

the pressure distribution is generated by lifting elements composed of steady horseshoe vortices and oscillatory doublets distributed over a large number of panels. The strengths of these vortices and doublets are determined by solving an integral equation analogous to that in the kernel-function method.

Djojodihardjo and Widnall[17] developed a numerical method based on the solution of an integral equation which relates the velocity potential to the normal velocity of the lifting surface. A step-by-step procedure is used to obtain the solution. The resulting surface integrals are evaluated numerically by dividing the lifting surface into a number of elements and assuming a distribution of doublets on these elements. Morino and co-workers[18-21] used a Green's function approach to derive an integral equation that relates the velocity potential to the prescribed motion of the surface. They solved this equation numerically by dividing the surface of the wing into a number of finite elements and assuming that within each element the velocity potential is constant and equal to the value of the potential at the centroid. They ended up with a set of linear algebraic equations which they solved for the velocity potential distribution. The above methods are restricted to small oscillations.

Belotserkovskii[22] and Belotserkovskii and Nisht[23] presented a numerical method based on modeling the lifting surface with a system of horseshoe vortices whose strengths vary with time. The continuous variation of the boundary conditions is replaced by a step-by-step process in which free vortices are shed at the end of each time step and

travel downstream along the surface of the wing and the wake. The strengths of the horseshoe vortices as well as the free shed ones are determined by satisfying the tangency condition over the wing and the condition of spatial conservation of circulation. The second version of this method and the present model are similar, but were developed independently. Summaries of this work were published in Refs. 24 and 25. Summa[26] applied a similar technique to impulsively starting rectangular wings of relatively high aspect ratios.

1.2.2 General Motions of Delta Wings

Hanin and Mishne[27] and Cohen and Nimri[28] treated the case of a steadily rolling delta wing by using a modified version of the Brown and Michael theory[29], where the two spiral vortices separated from the leading edges are represented by concentrated line vortices; these vortices are connected to the leading edges by feeding sheets. The positions and strengths of the line vortices are determined from the requirements that the flow velocity at the leading edge is finite and the net forces on the concentrated vortices and their feeding sheets are zero. Their results showed poor agreement with the experimental work of Harvey[30]. Pullin[31] and Jones[32] treated the case of a yawed delta wing by using the model of Mangler and Smith[33,34]. Their calculated pressure distribution agrees only with the low angle-of-attack results of Harvey[35]. The unsatisfactory results of these methods is due to their inaccurate modeling of the three-dimensional flow. The flow is assumed to be conical[34] and consequently the Kutta condition is violated. More-

over, use is made of slender-body theory which requires the axial-flow gradients to be small compared with the transverse-flow gradients.

For unsteady lateral motions, the flow conditions are more complicated and the wakes of the wing are no longer symmetric. Moreover, in the case of rolling motions, the leading-edge vortices may be situated on opposite sides of the wing, depending on the roll rate and the angle of attack. Kalman, Rodden and Giesing[36] studied unsteady lateral motions; however, their study is restricted to small oscillations and small angles of attack. In the present work the vortex-lattice technique is extended to treat arbitrary motions of delta wings. A summary of this work was published in Ref. 37. Thrasher et al[38] treated the case of rectangular wings executing general motions.

1.2.3 Wing-Body Combinations

Most of the available methods for wing-body combinations are limited to the linear range of the angle of attack. The early developments start with slender wing-body theory[39-41], whose application is severely restricted to a small class of configurations. Nevertheless, slender-body theory was used extensively for both subsonic and supersonic flows because of its simplicity.

Giesing[42] developed a general lifting-surface theory for wing-body combinations by using the method of images. His basic idea is to match each singularity external to the body with one internal to the body; the images are used to cancel the flow through the body surface generated by the external singularities. The strength and location of an image are

directly related to the strength and position of its external singularity and the body shape, thereby introducing no new unknowns. The image system is not completely effective in reducing the body surface to a stream surface since it is based on two-dimensional theory. Often additional singularities derived from a so-called residual potential are needed to render the body a stream surface. The lifting surface is represented by its image system and an axial doublet system, and the residual potential is accounted for by using a piecewise constant doublet distribution.

Later Giesing et al[43] used a combined slender-body theory, lifting-surface theory and the method of images to handle complex configurations. Woodward[44] and Kalman et al[36] replaced the body by an axial distribution of doublets and an annular wing of constant cross-section and obtained good agreement with experimental data. Hess and Smith[45], Hess[46,47], Rubbert and Sarris[48] and Tulinius[49,50] used a distribution of vorticity on either the wing camber line or surface and a distribution of sources or doublet elements on the wing and body surfaces. None of these methods accounts for the nonlinear effects due to the separation from the lifting surfaces and/or the body surface; moreover numerical instabilities arise in the intersection region of the body and the wing where sources are used to represent the body and vortices to represent the wing[46,48]. References 51 and 52 discuss these linear methods and their applications for subsonic and supersonic flow regimes. Maskew[53] presented a numerical method based on a surface distribution of quadrilateral vortex rings. Each quadrilateral element has a control point at

which the no-penetration boundary condition is satisfied. Although nonlinear effects arising from the wing tips are accounted for, separation at the leading edges is not treated. Moreover, all the numerical results presented are for wings of relatively high aspect ratios (5 and 3.2) for which nonlinear effects are negligible. Furthermore, his representation of the body by either a ring wing or an infinite vortex tube is not justifiable.

Otto[54] used the nonlinear model of Gersten[55] to account for the wing nonlinear effects. However, this model violates the force-free wake condition because it does not predict the wake shape; thus, its application to interfering lifting surfaces (wing-canard or wing-tail surface) will lead to serious errors. Furthermore, the wing area is increased to replace the mid-section of the body that intersects with the wing; thus, the configuration consists of the nose section and the tail section of the body and the wing. Using this composite representation and taking into account the effects of the body boundary layer, he obtained very good agreement with the experimental cases he considered.

Mendenhall and Nielsen[56] used the leading-edge-suction analogy of Polhamus[57-59] to account for the nonlinear effects of the lifting surfaces. A cross-flow theory combined with empirical formulas is used to handle the body nonlinear effects arising from the separation along the body surface. Only total loads are predicted; however, this method is able to handle body separation effects, though in an approximate fashion.

1.2.4 The Present Method

The present method is based on a surface distribution of quadrilateral vortices on the wing and body surfaces. Separation from the lifting surfaces (wing, canard and tail) is modeled by free vortex sheets, while separation from the body is ignored. The strengths of these vortices as well as the positions of the free vortex sheets are obtained simultaneously, thereby accounting for all interference effects. The vortex-lattice technique was used previously to treat far and close coupled wings[60,61]. The method is extended to treat unsteady flows by modifying the steady vortex model. The method is general and can treat arbitrary body shapes, wings and wing-body combinations at high angles of attack.

The present method is used to develop computer codes for the following cases:

1. Steady and unsteady symmetric motions of wings.
2. Steady and unsteady asymmetric motions of wings.
3. Steady symmetric motions of bodies.
4. Steady symmetric motions of wing-body combinations.

Total distributed loads are predicted and computer plottings of the free vortex sheets are presented.

CHAPTER II

METHOD DESCRIPTION

2.1 Problem Formulation

We consider a wing-body configuration executing a general motion in an incompressible fluid. The configuration surface is described by $F(\vec{r},t) = z - f(x,y,t) = 0$ in an inertial frame of reference. The perturbation velocity potential of an inviscid, irrotational, incompressible, steady or unsteady flow is governed by Laplace's equation

$$\nabla^2\phi = 0 \tag{2.1}$$

subject to the following boundary conditions:

(i) The fluid particles cannot penetrate the impermeable surface; that is,

$$\frac{DF}{Dt} = \frac{\partial F}{\partial t} + \vec{V} \cdot \nabla F = 0 \quad \text{at} \quad F(\vec{r},t) = 0 \tag{2.2}$$

If the flow is steady Eq. (2.2) reduces to the vanishing of the normal velocity at the fixed surface, namely

$$\vec{V} \cdot \vec{n} = 0 \quad \text{on} \quad F(\vec{r}) = 0 \tag{2.3}$$

where $\vec{n}$ is the unit vector normal to the surface.

(ii) The wakes emanating from the leading and trailing edges of the wing are force-free stream surfaces; that is

$$\Delta p = 0 \quad \text{across} \quad W(\vec{r},t) = 0$$

$$\frac{\partial W}{\partial t} + \vec{V} \cdot \nabla W = 0 \quad \text{on} \quad W(\vec{r},t) = 0$$

where Δp is the pressure jump across the wakes of the wing and $W(\vec{r},t) = 0$ is the equation of the wake. Here, we note that the function describing the wing wake $W(\vec{r},t) = 0$ is not known a priori and must be obtained as part of the solution. Treatment of the body wake is less clear and usually most potential models assume wake-free bodies. In the present method, the body wake is modeled by semi-infinite vortex lines tangent to the surface while at the same time keeping the option of a wake-free body.

(iii) The Kutta condition must be satisfied along the edges of the wing where separation occurs. This condition requires that no pressure discontinuity exists across the leading and trailing edges of the wings.

(iv) Whatever the nature of the disturbance produced by a wing-body combination, it must die out with increasing distance away from the configuration and its wakes. Equation (2.1) and the above boundary conditions constitute a well-posed problem for the perturbation velocity potential.

2.2 Wing Vortex Model in Steady Flow

The vortex model for wings alone follows that of Belotserkovskii[62], Kandil et al[3] and Maskew[53]. The wing is replaced by a bound vortex sheet with unknown strength. This continuous vortex sheet is approximated by a lattice of quadrilateral vortices. The wakes are represented by a series of discrete non-intersecting vortex lines. In Fig. 4, the vortex model for the delta wing is shown schematically. The wing is divided into rectangular and trapezoidal elements such that the spanwise

vortex segments are placed at the quarter-chord length for each rectangular element. The vortex segments for the trapezoidal elements are directed normal to the leading edge so that with this choice, the induced velocities of these segments are tangent to the leading-edge surface, thus partially satisfying the Kutta condition. The length of the segments directed normal to the leading edge is the same as that of the other spanwise elements; thus they extend slightly beyond the leading edge. Associated with each element is a control point taken as the centroid of each element where the boundary conditions are satisfied. The model is completed by adding free-vortex lines representing the continuous free-vortex sheets adjoining the trailing and leading edges where separation occurs. Each line is divided into series of small straight segments (near-wake field) and semi-infinite vortex lines (far-wake field). The upstream end of each segment represents a control point of the wake surface where the wake conditions are satisfied.

2.3 Wing Vortex Model in Unsteady Flow

The starting condition for unsteady flows can be a steady flow as represented by the steady vortex model discussed in Sec. 2.2 or no flow at all (i.e., starting from rest). Here, we consider the former. When conditions change with time, starting vortices form along the sharp edges, then they are shed and convected downstream with the local particle velocity. Thus, an ever-growing portion of the wake must also be represented by a lattice, not a series of non-intersecting lines as in the steady case. The continuous variation with time is approximated

by considering the motion to be a series of impulsive changes occurring at evenly spaced time intervals; thus the motion becomes smoother as the time intervals become smaller.

In Fig. 5 a schematic representation of the unsteady lattice is shown. The first arrangement corresponds to the first time step; hence, there is one shed vortex in the wake. The next arrangement corresponds to the second time step; hence, there are two shed vortex lines in the wake. The last arrangement shown corresponds to the third time step. Consequently, we have three shed vortex lines. With an incompressible model of the flow the instant the angle of attack changes, the vorticity on the wing and the position of the entire wake (i.e., the direction of the vorticity in the wake) change. A starting vortex forms along the sharp edges and subsequently is shed. But the strength of individual vorticity elements in the wake does not change; these vorticity elements are convected downstream with the fluid particles. Such a model of the flow is realistic only when the particle velocity is small compared with the speed of sound (low Mach number). In terms of the present discrete-line representation, the instant the angle of attack changes, the circulations in the lattice representing the surface and the directions of the finite vortical segments representing the wake change. But the circulations around the finite segments in the wake do not. When the cause of the unsteadiness whether it is rigid-body rotation or an oscillation around a mean angle of attack stops, vortex lines continue to be shed; however, the strengths of these lines decrease and a steady-state situation is achieved.

2.4 Vortex Model for Wing-Body Combinations in Steady Flow

Wing-body combinations are modeled by combining the vortex model for the wing discussed in Sec. 2.2 with a vortex distribution on the body surface. Thus, the wing and body surfaces are divided into a number of quadrilateral vortex panels (elements) of constant strength. The wing wakes are modeled as discussed previously in Sec. 2.2. The wake of a blunted end body is modeled by straight vortex lines that are tangent to the aft-end of the body and extend to infinity; otherwise, no trailing vortices from the body are used.

This vortex model is equivalent to a piecewise constant distribution of doublets over the configuration surface and the wakes[56]. The centroid of each panel or element is taken as a control point where the no-penetration condition is enforced. Figure 6 shows a schematic representation of a wing-body combination. Since the wing thickness is not considered, the intersection of the wing with the body is a curve rather than a surface making the geometric description relatively easy.

The use of quadrilateral vortices offers some advantages over the usual horseshoe vortices, due to the canceling effect of the adjacent parallel sides. Thus, the induced velocity from such vortices decreases rapidly with distance from the control point. Hence, limits can be put on the significant volume of influence of a quadrilateral vortex. Moreover, the resulting influence coefficient matrix is strongly diagonal making it easier to handle numerically.

2.5 Solution Procedure

2.5.1 Steady Flows

The boundary-value problem for wings or wing-body combinations as formulated in Sec. 2.1 is nonlinear because the shapes of the separated vortex sheets as well as their strengths are unknown. The solution procedure chosen in this study is iterative. The procedure of Belotserkovskii[62] and Kandil et al[3] is modified and generalized to treat wings in asymmetric flow and wing-body combinations. A summary of the procedure follows.

Using the geometries of the wing and/or wing-body combination either in analytic or discrete-data form, we divide the configuration surface into a number of rows and columns that define the surface panels or elements. Associated with each panel or element is a number of parameters (area, control point, unit normal) which are dealt with in detail in Appendix A. The wakes emanating from the leading and trailing edges of the lifting surface are assigned a certain direction which serves as an initial guess for the actual position. The choice of this initial guess is discussed in Sec. 2.6.2.

The influence coefficients of the induced velocity at each control point are calculated for all the quadrilateral vortex elements by using the Biot-Savart law combined with a viscous core relationship to overcome the singularity associated with using a potential vortex model. Appendix B contains the detailed formulas used in this step.

The circulation around each quadrilateral vortex element (loop circulation) is determined by simultaneously satisfying the no-penetra-

tion conditon and the spatial conservation of circulation. This involves the setting up of the influence coefficient matrix and selecting a suitable solver for the simultaneous algebraic equations. This is discussed in Appendices C and D.

The vortex segments in the wakes of the lifting surface are rendered force-free while the circulations are held constant. This is done by aligning each segment with the local velocity vector at its upstream end.

The preceding two steps are repeated until the wake shape does not change; that is, the maximum difference in the position of any wake vortex segment is less than a prescribed value. Convergence is obtained when two conditions are satisfied; first, the iterative procedure must converge for a given number of elements; and second, the predicted aerodynamic loads must converge as the number of elements is increased.

The total loads and pressure distribution are calculated by using Bernoulli's equation and/or the Kutta-Joukowsky theorem expressed in the appropriate frame of reference. The details of these calculations can be found in Appendix E.

2.5.2 Unsteady Flows

We start the numerical solution from a rest position or a steady solution. The continuous time variation is discretized. At each discrete time step, the solution is obtained in a manner similar to that used in obtaining the solution of the steady problem, taking into consideration the fact that the boundary conditions are time dependent and

vorticity is being shed from the separation edges. The convection of the shed vorticity downstream with the particle velocity is accomplished by moving the ends of the vortical segments of the shed lines according to

$$\vec{r}(t + \Delta t) = \vec{r}(t) + V(\vec{r},t)\Delta t$$

We note that the ever growing portions of the wakes complicate the influence coefficient matrix considerably (Appendix C). The strengths of the shed vortices are calculated by applying conservation of circulation at the wake nodal points (Appendix C).

The preceding step is repeated until the strengths of the currently shed vortices vanish and the previously shed vortices which have appreciable strengths are already convected far downstream so that their influence on the configuration is negligible. Then a steady state is achieved. The number of time steps required to achieve this steady state depends on the particular type of unsteadiness in the flow.

At each time step, the total and distributed loads are calculated by using the unsteady Bernoulli equation (Appendix E). Thus, a complete history of the flowfield during transient and steady-state periods is obtained.

2.6. Factors Affecting the Numerical Results

Attention has been given to several factors that affect the quality of the numerical results. Understanding the nature of these factors whether purely numerical or governed by some physical phenomenon is essential for obtaining high accuracy results and avoiding numerical troubles. These factors are discussed below.

2.6.1 Number and Distribution of Elements

For all finite-element problems, the quality of the solution depends on the number and distribution of elements used. In the present method it is found from numerical experimentation that using less than 50 elements to represent the wing surface will result in a low-quality solution. On the other hand, the computation time as well as the number of iterations required for convergence will increase with an increase in the number of elements. For steady flows, the number of segments in the trailing vortices has little effect on the total and distributed aerodynamic loads. In most instances, three such segments are used, with the last one being semi-infinite. But for unsteady flows, the length of each segment of each trailing vortex is determined by the position of the vortices shed at the discrete time steps. These segments must be retained to a distance of at least one chord length behind the trailing edge; beyond this distance a single semi-infinite segment is adequate. For the wing-body combination, the situation is more severe as many elements are needed to represent the body. Thus, relatively simple geometries are considered (cone-cylinders, ogives) to minimize the number of elements required to satisfactorily define the configuration. Approximately between 300 to 400 elements were used for most of the bodies considered. In each case, the convergence criteria were met (loads converge with iterations and number of elements).

We note that using a large number of elements is not sufficient for a high-quality solution. The element shapes and distribution is also important. Adjacent elements must not differ greatly in size and regions

of high flow gradients (wing tips, body-nose, wing-body junctions) must be represented by a finer lattice, therefore more elements. The present code uses the same number of rows and columns which makes it inapplicable to aspect ratios muct less than 1. The body lattice is general. As a rule of thumb, square or nearly square elements provide the best-quality solutions.

2.6.2. Free Vortex Lines and Convergence

The iterative scheme described in Sec. 2.5 is very sensitive to the initial geomertry of the wakes emanating from the leading and trailing edges of the lifting surface. Convergence can be accelerated or decelerated, depending on the initial guess for the wake geometries. An inappropriate starting guess may prevent convergence. From numerical experiments, it is found that for symmetric flows, the best choice is setting the leading-edge free vortex lines at half the angle of attack and the trailing edge vortex lines at one-third the angle of attack[2]. For steady rolling at a zero angle of attack, an appropriate initial guess for the orientation of the free vortices is to place them parallel to the x-z plane directed at an angle to the plane of the wing of $\frac{1}{2}\tan^{-1}\frac{|\vec{\omega}x\vec{r}|}{U_\infty}$ on the advancing side of the wing and $-\frac{1}{2}\tan^{-1}\frac{|\vec{\omega}x\vec{r}|}{U_\infty}$ on the receding side; $\vec{r}$ denotes the position vector from the centerline of the wing to the point at which the free vortex begins[37]. Furthermore, use of viscous-core relations is essential for avoiding the singularities associated with the application of the Biot-Savart law. If a free vortex comes in close proximity to another free vortex or to a

bound vortex, the large induced velocities that occur without a viscous core will lead to instabilities and convergence will not be achieved. This is crucial, especially with a large number of elements and relatively low angles of attack. Using computer plotting for the configuration under study is strongly recommended for its value in detecting errors in the geometry of the configuration, tracing the free-vortex lines during iteration, and locating numerical troubles arising when two or more vortex lines are very close.

2.6.3 Time Step Size

For unsteady flows, the time step size is an important factor. A coarse step size will yield crude results for the time histroy of the flow but will require less storage and computation time. On the otherr hand, a very fine step size will yield better results at the expense of increasing storage and computation time. A limited number of numerical experiments were conducted. It is found that a non-dimensional time step proportional to the size of the bound vortex lattice element is the best choice. This is supported by the work of Belotserkovskii[22] and Belotserkovskii and Nisht[23].

2.6.4 Computer Limitations

In all finite-element solutions computer storage and computation time place an upper limit on the size of the problem under consideration. For delta wings in steady symmetric flow, a typical case with 60 wing elements and 24 wake elements requires approximately 5-8 minutes

on an IBM 370/158 computer. For asymmetric cases (steady roll rates, constant angles of yaw and pitch), the computation times are about 2-3 times those of the symmetric cases. For unsteady flows the computation time is long, being directly proportional to the number of time steps used. Generally, the computation time ranges from 1/2 to 2 hours. For wing-body combinations in steady flow, the computation time ranges from 3/4 to 3 hours.

Most of the computation time is spent in calculating the induced velocities (i.e., influence coefficients). Since the influence of a quadrilateral ring vortex is negligible when it is far away (about 5 to 10 times the element size) from a control point, ring vortices are more advantageous than the usual horseshoe vortices.

Computer storage does not present a serious problem for wings in steady or unsteady flows, but it is serious for wing-body combinations because a large number of elements are needed to represent the configuration. To alleviate this problem in all the calculations presented here, we used single precision and considered relatively simple geometries having at least one plane of symmetry. Utilizing a CDC machine instead of an IBM 370/158 will reduce considerably the requried computation time, thereby making it possible to handle more complex configurations.

2.6.5 Vortex Breakdown

Development of the present method is based on the assumption that vortex-breakdown (bursting) does not occur on the wing surface. This

phenomenon is characterized by a sudden change of the structure of the vortex core. Downstream of the breakdown point the vortex core will diffuse and become larger owing to viscous dissipation. This results in lower pressure peaks and consequently in lower overall aerodynamic loads and moments. In symmetric flows, the position of the breakdown point depends on the angle of attack and the wing aspect ratio. At relatively low angles of attack, the breakdown point is located far downstream of the wing trailing edge. Increasing the angle of attack or the aspect ratio moves the breakdown point upstream. The decrease in the aerodynamic loads is felt as the breakdown point crosses the wing trailing-edge. This loss in the aerodynamic loads and moments decreases with decreasing aspect ratio. The angle of attack at which the breakdown point crosses the wing trailing-edge places an upper limit on the validity of the present method. Figure 7 shows the experimental results of Hummel[63], Earnshaw and Lawford[64] and Poisson-Quinton and Erlich[65] for the variation of the angle of attack at which vortex-breakdown occurs with the aspect ratio for delta wings. Disagreement of the data reflects the need for more work in this area. References 4 and 66 contain more complete reviews of numerical and experimental works dealing with vortex breakdown.

CHAPTER III

NUMERICAL RESULTS

3.1 Unsteady Longitudinal Motions of Wings

Figure 8 shows the development of the unsteady wake for a delta wing undergoing a sinusoidal variation in the angle of attack. It depicts actual solutions in which the position of each vortex segment is determined; accurate location of the wake is critical to the study of interacting lifting surfaces. In Figs. 9 and 10 the pressure distributions for a rectangular and a delta wing are shown at different chordwise stations. These figures show the common rise in the pressure as the outboard region is approached; this is due to the strong effect of the separation at the tips of the rectangular wing and the leading edge of the delta wing. Figure 11 shows the pressure distribution at successive time steps at a given chordwise station for a delta wing undergoing a sinusoidal variation in the angle of attack. It is noted that the peak of the pressure distribution moves inboard as the angle of attack increases. This behavior was observed experimentally by Lambourne, et al[60] when they examined the behavior of the leading-edge vortices for a delta wing undergoing a sudden change in the angle of attack. They found that, following an increase in the angle of attack, the strengths and heights of the leading-edge vortices at any spanwise section will increase, while the secondary vortices will grow. Thus, the pressure peak will increase and it tends to be broadened later on.

Figure 12 show the transient behavior of the normal force and pitching moment coefficients for a rectangular wing of an aspect ratio of one as the angle of attack increases linearly to a maximum and then decreases to its initial value. The variation shows a hysteretic behavior, in agreement with the experimental observation of Lambourne, Bryer and Mayberry[67] that the movement of the leading-edge vortices for a delta wing is not reversible during an increase and a decrease in the angle of attack. Consequently, the pressure, forces and moments exhibit this hysteretic behavior. Furthermore, this irreversible behavior was also observed by Hunt, Roberts and Walker[68] in their investigation of the effect of a gust on increasing and decreasing the lift. The hysteretic loops shown in Fig. 12 are asymmetric because of the variation of the flow field with angle of attack.

Figure 13 shows the variation of the normal-force and pitching-moment coefficients for a delta wing undergoing a sinusoidal variation in the angle of attack. It shows that there is a marked phase lag during the transient period before the periodic solution is achieved. Keating[69] found from his experimental measurements on a delta wing oscillating in heave that there is a cyclic phase lag in the pressure over the wing surface due to the movement of the vortex field over the wing and that this phase lag is correlated with a frequency parameter based on the distance from the apex. Also, Randall's theoretical model[70] predicts a phase lag for a heaving delta wing. Moreover, the experimental results of Lambourne, Bryer and Mayberry[71] for the case of oscillatory deformation of a delta wing indicate a time-delay between

the unsteady pressure over the wing surface and the corresponding steady pressure for the static deformation case. This phase delay is approximately equal to the time required for the convection of vortices from the apex of the wing to the particular chordwise position.

In Fig. 14, convergence of the normal-force and pitching-moment coefficients as the number of elements is increased is shown for a delta wing undergoing an oscillation in the angle of attack. Convergence of the results is essential for all finite-element methods and it is dependent on the shape and distribution of the elements.

3.2 Yawed Delta Wings

Figure 15 shows the wake shape for a delta wing in symmetric steady flow at an angle of attack 15°; the resulting vortex cones emanating from the leading edges are symmetric in shape and strength. Figure 16 shows the wake shape for the same wing at the same angle of attack but yawed at an angle of 5°. In this case the vortices are not symmetric because the yawing causes the windward leading-edge vortex to move inboard and closer to the wing surface and the leeward leading edge vortex to move outboard and higher. Figure 17 shows the wake shape when the angle of yaw is increased to 10° while the angle of attack is kept at 15°; in this case, the windward vortex is increased in strength and is moved further inboard while the leeward vortex is weakened. The vortex segments of the windward leading-edge vortex show a number of kinks which can be cured by increasing the number of its vortex segments.

Convergence for all the test cases considered was difficult to achieve for large angles of yaw. The number of iterations required for

convergence varied from 7-10, resulting in an increase in the computation time. For the case with a 15° angle of attack and a 15° angle of yaw, convergence was not achieved at all.

In Fig. 18, the net pressure distribution is shown for a delta wing in a symmetric steady flow at a 15° angle of attack. There is good agreement between our results, Pullin's[31] theoretical results and Harvey's experimental results[35]. While Pullin's results overpredict the suction peaks, the present method underestimates them. However, for this case, the secondary separation is not strong enough to cause large disagreement between theory and experiment. Figure 19 shows the net spanwise pressure distribution for a delta wing at 15° angle of attack and 5° angle of yaw. Harvey's experiments[35] show that yaw alters the strength and position of the suction peaks due to the movement of the vortex cores above the wing. The strengthening of the secondary vortex at the windward leading edge produces a second suction peak outboard of that due to the main vortex. The weakening of the leeward main vortex results in a weaker and broader pressure peak. Since our model does not account for secondary separations, our results are in fair agreement with those of Harvey[34] on the leeward side, while they do not predict the two suction peaks on the windward side. However, our results are in better agreement with the experimental results than those of Pullin[31].

Figure 20 shows that increasing the yaw angle to 10° while keeping the angle of attack at 15° seems to decrease the discrepancy between our results and the experimental results. This may be due to the movement of the secondary vortex inboard closer to the main vortex.

Attempts to compare our results with the theoretical work of Jones[32] were not successful because he considered low angles of attack (i.e., 5°) for which convergence in the present method was difficult to achieve.

3.3 Delta Wings in Rolling Motion

For a delta wing rolling at an angle of attack, the vortex cones emanating from the leading edges may be both located above the wing surface or one cone may be located above the wing while the other may be located under it. This can occur asymmetrically or antisymmetrically, depending on the angle of attack and roll rate. As mentioned earlier, the present iterative scheme is very sensitive to the initial guess. Thus, a bad guess will lead to slow convergence or none at all. When the angle of attack is zero, the two vortices have the same size and strength with one of them located above the wing and the other below it, irrespective of the value of the roll rate. Moreover, Harvey observed experimentally that, for a rolling delta wing at a zero angle of attack, there is no secondary separation. Secondary separation is one of the main factors for the discrepancy between theory and experiment. Thus, it is felt that comparison with experiments at a zero angle of attack is more meaningful than at a non-zero angle of attack. Therefore, all the rolling cases considered are at a zero angle of attack.

Figures 21-23 show typical solutions of the free-vortex lines representing the two vortex cones on each side of a delta wing (AR = 0.7). The wing is rolling steadily at zero angle of attack and a roll rate of 0.2, 0.4 and 0.6, respectively. In each figure, a three di-

mensional view and a plan view are given. The two vortex cones are located antisymmetrically on each side of the wing. These figures show that the size and strength of the spiral cones increase with increasing roll rate in agreement with Harvey's experimental results[30].

Figure 24 shows the spanwise pressure distribution on the upper and lower surfaces of a delta wing at the chordwise station $x/c_r = 0.779$. The present results are compared with the experimental results of Harvey and the theoretical models of Hanin and Mishne[27] and Cohen and Nimri[28]. The present method shows better agreement with the experiments. The results of Hanin and Mishne[27] and Cohen and Nimri[28] overpredict by large amounts the suction peak on the receding side of the wing; this is a result of their use of a simplified separation-flow model[29]. The present method predicts a slightly lower value for the suction peak at a position closer to the leading edge. The absence of secondary separation produces a single sharp peak in the pressure at the leading edge instead of the two peaks associated with the main and secondary separation vortices.

Figure 25 shows the free-vortex lines at three successive time steps for a delta wing undergoing an unsteady rolling motion given by $\omega_x = 0.6 + 0.1 \sin(\frac{\pi t}{6})$. The vortices shed from the edges of separation and later convected downstream are shown. Convergence in these cases was obtained without difficulty when the inclinations of the free-vortex lines were assumed initially to be $-\frac{1}{2}\tan^{-1}(\frac{|\vec{\omega}x\vec{r}|}{U_\infty})$ for the advancing side and $\frac{1}{2}\tan^{-1}(\frac{|\vec{\omega}x\vec{r}|}{U_\infty})$ for the receding side.

Figure 26 shows the time history of the spanwise pressure distribution of the chordwise station $x/c_r = 0.65$. It show that increasing the roll rate increases the value of the suction peak which remains at a positon about 20% inboard of the leading edge. This behavior is different from the case of a delta wing at an angle of attack without rolling where the suction peak lies approximately 30% inboard of the leading edge and where increasing the angle of attack causes the suction peak to move inboard. These differences are caused by the centrifugal acceleration due to the rotation of the wing.

Figure 27 shows the effect of the frequency of the varying part of the roll rate on the rolling-moment coefficient, while Fig. 28 shows also the effect of varying the magnitude of the steady part of the roll rate. The rolling-moment coefficient decreases with increasing frequency, while it increases with increasing roll rate. Although the rate of convergence for the rolling cases is better than that for the yawing cases, the number of cases presented here was limited by the large computation time, especially for large number of time steps.

3.4 Bodies Alone (Steady Symmetric Motions)

Before applying the present method to wing-body configurations, we felt it necessary to show that it can be applied to bodies alone.

Figure 29 and 30 show the pressure distributions for two tangent-ogives of a fineness ratio of 3.5 and 5.0, respectively, at a zero angle of attack. Comparison is made with the experimental results of Fox[72]

and the theoretical model of woodward[73]. The agreement is quite good except at the tail region where viscous effects dominate. Figure 31 shows the pressure distribution for a cone-cylinder of fineness ratio 2.25 at a zero angle of attack. The results are compared with the experimental results of Johnson[74] and the numerical results obtained by using the Douglas-Neumann program[75]. The good agreement achieved in Figs. 29-31 is due to the fact that at a zero angle of attack separation occurs at or very near the tail region of the body surface. Thus, viscous effects are minimized on the forward part of the body. Also, due to the symmetry of the flows and of the bodies considered, only one quadrant of the actual body was considered, making it possible to use a large number of elements and consequently resulting in a high accuracy.

As the angle of attack is increased from zero, separation will occur first near the aft-end of the body surface and then it will move forward. This will be accompanied by the shedding of vortices which will be symmetric for low and moderate angles of attack and will be asymmetric at high angles of attack even in the absence of a side-slip. These viscous effects tend to deteriorate the quality of the results obtained by the present potential model. Figure 32 shows the pressure distribution for a cone-cylinder of a fineness ratio of 2.25 at a 20° angle of attack. The results are for the two circumferential stations $\theta = 45°$ and $\theta = 135°$. Comparison is made with numerical results obtained by using the Douglas Neumann program[75] and the experimental results of Johnson[74]. The results are in good agreement in the nose region where viscous effects are small but not in the aft-region. From

this it is concluded that satisfactory results can be obtained forward of the separation region as also shown in Fig. 33. It shows the pressure distribution for a tangent-ogive of a fineness ratio of 10.7 at a 10° angle of attack. Figure 33 shows that our results are in good agreement with the experimental results of Tinling and Allen[76] at the first three stations x/d = 2, 4.5 and 6. However, at the station x/d = 10, there is a large discrepancy because separation starts approximately at x/d $\simeq$ 7 according to them. Thus, large discrepancies are expected downstream of the station x/d $\simeq$ 7.

Figure 34 compares our calculated pressure distribution with that calculated by using the Douglas-Neumann program[75] and the experimental data of Johnson[74] for a cone-cylinder of a fineness ratio of 2.25 at a 20° angle of attack. At the forward station x/d = 1.36 the agreement is very good. However, at the downstream station x/d = 2.96 near the shoulder of the cone cylinder, there is a large discrepancy because the flow separates in this region.

3.5 Wing-Body Combinations (Steady Symmetric Flows)

Figure 35 shows the variation of the lift coefficient with angle of attack for a wing-body combination representing a supersonic aircraft model. This figure also shows the experimental results of Henderson[77] at different Reynolds numbers, theoretical results based on the Polhamus suction analogy and the linear results of Lamar[78]. Both the leading-edge suction analogy and the present method agree well with the experimental data although body separation is not taken into account. This may be due to the breakdown of the wing vortices which tends to reduce

the aerodynamic loads and hence counteracts the lift generated by body separation. As expected, the experimental results show that the aerodynamic loads are independent of the Reynolds number. Since the wings have sharp edges, the flow separates at the edges, irrespective of the value of Reynolds number. This is an important point because in the present method separation is assumed to occur at the sharp edges (leading or trailing). Since the taper ratio of the wing is high, the clipped delta wing was approximated fairly accurately by a delta wing. Figure 35 shows that the linear results are satisfactory only for small angles of attack (i.e., 0-5°) and that the nonlinear effects increase with increasing angle of attack. At an angle of attack of 15°, the linear results underpredict the lift by about 30%.

Figures 36 and 37 show the variation of the induced drag and pitching-moment coefficients with the lift coefficient for the same configuration shown in Fig. 35. Our results, as well as these based on the suction analogy, are in good agreement with the experimental results at moderate values of the lift coefficient. However, at higher values of the lift coefficient, our results are in better agreement with the experimental pitching-moment coefficient, while the results of the suction analogy are in better agreement with the experimental drag coefficients. The discrepancy between our results and the experimental data at the higher values of the lift coefficient may be due to separation over the body. The relatively good results obtained for this wing-body configuration are partly due to the fact that the ratio of the body diameter to the wing span is about 10%. Therefore, the contribution

of the body to the total aerodynamic loads is small[39,79]. Also it is due to the minimized effect of secondary separation in the experimental data because Henderson used strip wires to ensure a turbulent flow over the wing surface[80].

Figures 39-41 depict the flow pictures as obtained from the present computer code. The shapes and positions of the vortex lines emanating from the sharp edges are shown, which are important in the case of interaction problems such as wing-body or wing-tail or wing-canard. As the angle of attack increases, the centroids of the two spiral vortices move away from the wing. Comparisons with the cases involving wings alone show that the presence of the body tends to shift the vortex cones or spirals away from the wing surface. Computer storage and time limit the downstream extent in which the wake field is accounted for. In all cases considered, the body wake is represented by semi-infinite straight-vortices inclined at half the angle of attack.

Figure 41 shows the variation of the lift and pitching-moment coefficients with angle of attack for the missile configuration considered by Otto[54]. Otto modeled this configuration by extending the wing area to cover the parts of the body adjoining it. Our results fall half way between the values obtained from the linear theory and the experimental results, whereas Otto's results[54] agree very well with the experimental results. For this configuration, the ratio of the body diameter to the wing span is nearly 50%; consequently, the body contribution to the aerodynamic loads which is not fully accounted for in our model is appreciable.

Figures 42-44 show the vortex lines for this configuration and the development of the vortex spirals with increasing angle of attack.

Figures 45 and 46 show the variation of the lift and pitching-moment coefficients with angle of attack for two wing-body combinations with delta wing planforms. These results are in good agreement with the experimental data of Hall[81] because the body contribution is small. Figure 47 compares the converged shapes of the free vortex lines with the initial guess, for the configuration of Fig. 45. For this configuration, the aspect ratio is 2 and the fineness ratio is 12.5. We note the presence of the body resulted in the divergence of the vortex lines. Figure 48 shows that the outward divergence of the vortex lines increases with increasing angle of attack.

Figure 49 shows the effect of the presence of a body for two wing-body combinations. The presence of a body results in an increase in the overall lift coefficient (carry-over lift) as expected. The wing circulation must in part extend around the body itself, thereby producing an increase in the lift due to the interference between the wing and the body; this effect increases with increasing angle of attack.

Figure 50 shows the convergence of the total aerodynamic loads (C_L, C_M and C_D) with increasing the number of elements. It shows that the number of elements required for convergence is around 500 for such a simple configuration.

3.6 Concluding Remarks

A modified vortex-lattice method is developed to solve for non-linear steady and unsteady flows past wings, bodies and wing-body com-

binations. The method uses a distribution of constant strength quadrilateral vortices on the wings and body surfaces. The time-dependent flows are dealt with by descretizing the continuous time variation and allowing for free vortices to be shed from the sharp edges at each time step. The use of quadrilateral vortices is more efficient than the usual horseshoe vortices because of their limited region of influence. Furthermore, the use of vortices to represent the body avoids numerical difficulties in the intersection region of the body and the wing when sources are used to represent the body and vortices to represent the wing. Also the use of vortices to represent the body will simplify the inclusion of body separation.

The present method is based on the following assumptions:

1. Vortex break-down on the wing surface is neglected, this phenomenon is accompained by a decrease in the aerodynamic loads. However, body separation which tends to increase the aerodynamic loads is also neglected, thus, the two effects counteract each other and application of the method to wing-body configurations in situations where vortex break-down is shown to occur still gives good results.

2. The wings have sharp edges; thus, the separation positions are defined. Moreover, only primary separation is modeled (secondary and tertiary separations are neglected).

3. The flow is assumed to be incompressible although compressibility effects can be accounted for by using the Prandtl-Glauert and Göthert rules.

4. Body separation is neglected in the present method, though this can be taken into account once the position of separation is known from either experiment or numerical viscous codes.

The method is applied first to delta wings in unsteady motion (symmetric). The results show good agreement with available experiments and the observed hysteretic behavior of the unsteady loads is predicted by the present method. Unsteady asymmetric motions are considered and the results are in a much better agreement with experimental data than other numerical methods. Also the method has the advantage of treating transient flows without the restriction of small disturbances.

For bodies alone the present method shows good agreement with the experimental data ahead of the separation region. The results are as good as those obtained by using the Douglas-Neumann program, which is based on sources and sinks.

For wing-body combinations the agreement with available experimental data and other numerical methods is good as long as the angle of attack is not very high and the ratio of the body diameter to wing span is small.

Implementation of the present method requires large computation time and storage, especially for unsteady flows and for flows past wing-body combinations. Optimizing the present codes and utilizing a faster computer than the IBM-370/158 will alleviate this constraint considerably.

The following is a list of areas for improving and extending the present method:

1. Using higher-order distributions (linear, quadratic) for the vortex elements, thus reducing the number of elements required to represent the configurations for the same accuracy.

2. Accounting for compressibility effects by using a Prandtl-Glauert type transformation based on freestream or local conditions.

3. Generalizing the present code to handle planforms other than the delta and rectangular planforms.

4. Including the thickness and camber effects.

5. Coupling the present code with a viscous code to determine the separation line and hence handle a general class of problems including body-separation effects.

6. Coupling the present code with a stress and/or deflection code, to enable the calculation of the deformations of wings, bodies and wing-body combinations under aerodynamic loads; these are essential in aero-elastic analyses.

REFERENCES

1. Parker, A. G., "Aerodynamic characteristics of slender wings with sharp leading edges - A review" J. Aircraft, 13, 1976, 161-168.
2. Kandil, O. A., Prediction of the steady aerodynamic loads on lifting surfaces having sharp-edge separation", Ph.D. Thesis, VPI & SU, 1974.
3. Kandil, O. A., Mook, D. T. and Nayfeh, A. H., "Nonlinear prediction of the aerodynamic loads on lifting surfaces", J. Aircraft, 13, 1976, 22-28.
4. Matoi, T. K., "On the development of a unified theory for vortex flow phenomenon for aeronautical application", M.I.T. Technical Report, 1975.
5. Razak, K. and Snyder, M. H., "A review of the planform effects on the low-speed aerodynamic characteristic of triangular and modified triangular wings", NASA CR-421, 1966.
6. Ashley, H., Widnall, S. and Landahl, M., "New directions in lifting surface theory", AIAA J., 1, 3-16, 1965.
7. Landahl, M. and Stark, V. T., "Numerical lifting surface theory (Problems and Progress)", AIAA J., 6, 2049-2060, 1968.
8. Runyan, H. L. and Woolston, D. S., "Method for calculating the aerodynamic loading on an oscillating finite wing in subsonic and sonic flow", NACA Report 1322, 1957.
9. Watkins, C. E., Runyan, H. L. and Woolston, D. S., "On the Kernel function of the integral equation relating the lift and and downwash velocity distributions of oscillating finite wings in subsonic flow", NACA Report 1234, 1955.

10. Watkins, C. E., Woolston, D. S. and Cunningham, H. J., "A systematic Kernel function procedure for determining aerodynamic forces on oscillating or steady finite wings at subsonic speeds", NACA TR 448, 1959.

11. Küssner, H. C., "A general method for solving problems of the unsteady lifting surface theory in the subsonic range", J. of Aero. Sci., 17-26, 1954.

12. Jones, W. P., "Oscillating wings in compressible subsonic flow", R & M 2855, ARC, 1951.

13. Jones, W. P. and Moor, J. A., "Simplified aerodynamic theory of oscillating thin surfaces in subsonic flow", AIAA J., 9, 1305-1309, 1973.

14. Albano, E. and Rodden, W. P., "A doublet lattice method for calculating lift distributions on oscillating surfaces in subsonic flow", AIAA J., 7, 279-285, 1969.

15. Kalman, T. P., Rodden, W. P. and Giesing, T. P., "Aerodynamic influence coefficients by the doublet lattice method for interference nonplaner lifting surfaces oscillating in a subsonic flow", Report No. DAC-67977, 1968.

16. Rodden, W. P., Giesing, T. P. and Kalman, T. P., "Refinement of the nonplaner aspects of the subsonic doublet-lattice lifting surface method", J. of Aircraft, 9, 69-73, 1972.

17. Djojodihardjo, R. H. and Widnall, S. E., "A numerical method for the calculating of nonlinear unsteady lifting potential flow problems", AIAA J., 10, 2001-2009, 1969.

18. Morino, L., "Unsteady compressible potential flow around lifting bodies", AIAA Paper No. 73-196, 1973.

19. Morino, L. "Subsonic potential aerodynamics for complex configuration", AIAA J., 2, 191-197, 1974.

20. Morino, L., Chen, L. T. and Suciu, E. O., "Steady and oscillatory, subsonic and supersonic aerodynamics around complex configuration", AIAA J., 13, 368-374, 1975.

21. Morino, L., "A general theory of unsteady compressible potential aerodynamics", NASA CR 2464, 1974.

22. Belotserkovskii, S. M., "Gust effects on wings of complex planform at subsonic speeds", Mekanika Zhrdkosti i Craza, 4, 129-138, 1966.

23. Belotserkovskii, S. M. and Nisht, M. I., "Nonstationary nonlinear theory of a thin wing of arbitrary planform", Fluid Dynamics, 583-589, 1976.

24. Atta, E. H., Kandil, O. A., Mook, D. T. and Nayfeh, A. H., "Unsteady flow past wings having sharp-edge separation", NASA SP-405, 407-418, 1976.

25. Atta, E. H., Kandil, O. A., Mook, D. T. and Nayfeh, A. H., "Nonlinear unsteady aerodynamic loads on rectangular and delta wings", AIAA Paper No. 77-156, 1977.

26. Summa, J. M., "Potential flow about three-dimensional lifting configurations with application to wings and rotors", AIAA Paper No. 75-126, 1975.

27. Hanin, M. and Mishne, D., "Flow about a rolling slender wing with leading edge separation", Israel J. of technology, 11, 131-136, 1973.

28. Cohen, M. J. and Nimri, D., "Aerodynamics of slender rolling wings at incidence in separated flow", AIAA J., 14, 886-893, 1976.

29. Brown, C. E. and Michael, W. H., "On slender delta wings with leading-edge separation", NACA Tech. Note 3430, 1955.

30. Harvey, J. K., "A study of the flow field associated with steadily-rolling slender delta wing", J. of the Royal Aero. Sci., 68, 106-110, 1958.

31. Pullin, D. I., "Calculations of the steady conical flow past a yawed slender delta wing with leading edge separation", Imperial College of Science and Technology, Aero Report 12-17, 1972.

32. Jones, I. P., "Flow seperation from yawed delta wings", Computers and Fluids, 3, 155-177, 1975.

33. Mangler, K. W. and Smith, J. H. B., "Calculation of the flow past slender delta wings with leading edge seperation, RAE Report No. 2593, 1957.

34. Smith, J. H. B., "Improved calculation of leading-edge seperation from slender delta wings", Proc. Roy. Soc. Lond., 67-90, 1968.

35. Harvey, J. K., "Some measurements on a yawed slender delta wing with leading-edge seperation", J. of the Roy. Aero. Sci., 68, 106-110, 1964.

36. Kalman, T. P., Rodden, W. P. and Giesing, J. P., "Application of the doublet lattice method to non-planar configuration in subsonic flow", J. Aircraft, 8, 406-413, 1971.

37. Atta, E. H., Kandil, O. A. and Nayfeh, A. H., "Three-dimensional, steady and unsteady asymmetric flow past wings of arbitrary plan-

forms", AGARD Paper No. 2, AGARD Fluid Dynamics Panel Symposium, Unsteady Aerodynamics, Ottowa, Canada, 1977.

38. Thrasher, D. F., Mook, D. T., Kandil, O. A. and Nayfeh, A. H., "Application of the vortex-lattice concept to general, unsteady lifting-surface problems", AIAA Paper No. 77-1157, 1977.

39. Nielsen, J. N., "Missile Aerodynamics", McGraw-Hill Book Company, 1960.

40. Ferrari, C., "Interaction problem in high speed aerodynamics and jet propulsion, ed. H. R. Lawerence, A. F. Donovan, Section C, Vol. VII, Princeton, N. J., Princeton Univ. Press, 1957.

41. Lawerence, H. R. and Flax, A. H., "Wing-body interference at subsonic and supersonic speeds-survey and new developments", J. of Aero. Sci., 21, 289-324, 1954.

42. Giesing, J. P., "Lifting surface theory for wing-fuselage combinations", Douglas Aircraft Co., Report DAC-67212, 1968.

43. Giesing, J. P., Kalman, T. P., Rodden, W. P., "Subsonic unsteady aerodynamics for general configurations. USAF FDL-TR-71, 1971.

44. Woodward, F. A., "Analysis and design of wing-body combinations at subsonic and supersonic speeds", J. Aircraft, 5, 528-534, 1968.

45. Hess, J. L. and Smith, A. M. O. "Calculation of potential flow about arbitrary bodies", Progress in Aero. Sci., Pergamon Press, N.Y., 8, 1967.

46. Hess, J. L., "The problem of the three dimensional lifting potential flow and its solution by means of a surface singularity distribution", Computer Methods in Applied Mechanics and Engineering, 4, 1974.

47. Hess, J. L., "Review of integral-equation techniques for solving potential flow problems with emphasis on the surface-source method", Computer Methods in Applied Mechanics and Engineering, 4, 1975.

48. Rubbert, P.E. and Sarris, G. R., "A general three-dimensional potential flow method applied to V/STOL aerodynamics, SAE Paper No. 680304, 1968.

49. Tulinius, J. R., "Theoretical prediction of thick wing and pylon-fanpod-nacelle aerodynamic characteristics at subcritical speeds", North Am. Rockwell Corp. Rep. NA-71-447, 1974.

50. Tulinius, J. R., "Theoretical prediction of airplane stability derivatives at subcritical speeds", NASA CR-132681, 1972.

51. Ashley, H. and Rodden, W. P., "Wing-body aerodynamics interaction", Annual Review of Fluid Mechanics, 4, 431-472, 1972.

52. Thomas, J. L., "Subsonic finite elements for wing-body combinations", NASA SP-405, 1976.

53. Maskew, B., "Calculation of the three-dimensional potential flow around lifting non-planer wings and wing-bodies using a surface distribution of quadrilateral vortex-rings", TT-7009, Loughborough Univ. Tech. No. 1, 1970.

54. Otto, H., "A Contribution to the non-linear lift and pitching moment properties of slim wing-body combinations", DLR-F-73-66, 1973.

55. Gersten, K., "Calculation of non-linear aerodynamic stability derivatives of aeroplanes. AGARD Report No. 342, 1961.

56. Mendenhall, M. R. and Nielsen, J. N., "Effect of symmetrical vortex shedding on the longitudinal aerodynamic characteristics of wing-body-tail combinations", NASA CR-2473, 1975.

57. Polhamus, E. C., "A concept of the vortex lift of sharp-edge delta wings based on a leading-edge-suction analogy", NASA TN D-3767, 1966.

58. Polhamus, E. C., "Charts for predicting the subsonic vortex-lift characteristics of arrow, delta and diamonds wings", NASA TN D-6243, 1971.

59. Polhamus, E. C., "Prediction of vortex-lift characteristics by a leading-edge-suction analogy", J. of Aircraft, 8, 193-199, 1971.

60. Kandil, O. A., Mook, D. T. and Nayfeh, A. H., "Application of the nonlinear vortex-lattice concept to aircraft interference problems", NASA CP-2001, 1321-1330, 1976.

61. Kandil, O. A., Mook, D. T. and Nayfeh, A. H., "A numerical technique for computing subsonic flow past three-dimensional canard-wing configurations with edge separation", AIAA Paper No. 77-1, 1977.

62. Belotserkovskii, S. M., "Calculating of the flow around wings of arbitrary planforms in a wide range of angles of attack, NASA TT F-12, 1969.

63. Hummel, D., "Vortex breakdown effects on the low-speed aerodynamic characteristics of slender delta wings in symmetrical flow", J. of the Royal Aero. Sci., 71, 1966.

64. Earnshaw, P. B. and Lawford, J. H., "Low speed wind tunnel experiments on a series of sharp edged delta wings', RAE TN 2780, 1961.

65. Poisson-Quinton, Ph. and Erlich, E., "Hyperlift and balancing of slender wings", N66-24634, 1966.

66. Hall, M. G., "Vortex breakdown", Annual Review of Fluid Mechanics, 4, 1972.

67. Lambourne, N. C., Bryer, D. W. and Mayberry, J. F. M., "The behaviour of the leading-edge vortices over a delta wing following a sudden change of incidence", R & M No. 3645, 1969.

68. Hunt, Cr. K., Roberts, D. R. and Walker, D. J., "Measurements of the transient pressures on a narrow delta wing due to an upward gust", ARC C. P. 624, 1961.

69. Keating, R. F. A., "Measurement of the pressures and delta wing oscillating in heave at high angle of incidence", RAE, Aero 2924, 1967.

70. Randall, D. G., "A theoretical determination of the flow past and the airforces on an oscillating slender delta wing with leading edge seperation", R. A. E. Report Structures 284, 1963.

71. Lambourne, N. C., Bryer, D. W. and Naybrey, J. K. M., "Pressure measurements on a model delta wing undergoing oscillatory deformation", R & M No. 3693, 1940.

72. Fox, C. H., "Experimental surface pressure distribution for a family of axisymmetric bodies at subsonic speeds", NASA TM X-2439, 1971.

73. Woodward, F. A., "An improved method for the aerodynamic analysis of wing-body-tail configuration in subsonic and supersonic flow", NASA CR-2228, 1973.

74. Johnson, W. E., "Experimental investigation and correlation with theory of the surface pressure distribution on several sharp and blunted cones for incompressible flow", M.Sc. thesis, Dept. of Aero. and Astro, Univ. of Washington, 1963.

75. Hess, J. L. and Smith, A. M. O., "Calculation of the nonlifting potential flows about arbitrary three dimensional bodies", Report No. E. S. 40622, McDonnell-Douglas Co., 1962.

76. Tinling, B. E. and Allen, C. Q., "An investigation of the normal-force and vortex-wake characteristic of an ogive-cylinder", NASA TN D-1297, 1962.

77. Henderson, W. P., "Effects of wing leading-edge radious and Reynolds number on longitudinal aerodynamic characteristics of highly swept wing-body configurations at subsonic speeds", NASA TN D-8361, 1976.

78. Lamar, J. E., "Some recent applications of the suction analogy to vortex-lift-estimates", NASA SP-347, 1975.

79. Thwaites, B., "Incompressible Aerodynamics", Oxford, Clarendon Press, 1960.

80. Hummel, D., "Study of the flow around sharp edged slender delta wings with large angles of attack", NASA TT F-15, 1973.

81. Hall, C. F., "Lift, drag, and pitching moment of low-aspect-ratio wings at subsonic and supersonic speeds", NACA RM A53A30.

82. Lamb, H., Hydrodynamics, Sixth ed., Dover, 1945.

83. Bloom, A. M. and Jen, H., "Roll-up of aircraft trailing vortices using artificial viscosity", J. Aircraft, 11, 1974.

84. Kuwahara, K. and Takami, H., "Numerical studies of two-dimensional vortex motion by a system of point vortices", J. Physical Soc. of Japan, 34, 1973.

85. Yager, P. M., Holland, C. H. and Strand T., "Modified Weissinger lifting surface method for calculating aerodynamic parameters of arbitrary wing-canard configurations", Air Vehicle Corp., La Jolla, Calif. Rep. 354 354, 197

86. Etkin, B., "Dynamics of Atmospheric Flight". John Wiley, N.Y., 1972.

87. Westlake, J. R., "A Handbook of Numerical Matrix Inversion and Soluton of Linear Equations", Krieger Publishing Co., 1975.

APPENDIX A

Lattice Geometry

1. Surface Panels (Elements)

A quadrilateral surface element is described by four corner points as shown in Fig. 51. With each element, we define three parameters, a control point x_m, y_m, z_m, a unit normal $\vec{e}_n$ and an element area A. These parameters are defined as follows:

$$\begin{aligned} x_m &= \frac{1}{4}(x_1 + x_2 + x_3 + x_4) \\ y_m &= \frac{1}{4}(y_1 + y_2 + y_3 + y_4) \\ z_m &= \frac{1}{4}(z_1 + z_2 + z_3 + z_4) \\ \vec{e}_n &= e_x\vec{i} + e_y\vec{j} + e_z\vec{k} = \frac{\vec{d}_1 x \vec{d}_2}{|\vec{d}_1 x \vec{d}_2|} \end{aligned} \tag{A1}$$

where

$$A = \frac{1}{2}\left[(\vec{d}_1 x \vec{d}_2) \cdot (\vec{d}_1 x \vec{d}_2)\right]^{1/2} \tag{A3}$$

$$\begin{aligned} \vec{d}_1 &= (x_3 - x_1)\vec{i} + (y_3 - y_1)\vec{j} + (z_3 - z_1)\vec{k} \\ \vec{d}_2 &= (x_4 - x_2)\vec{i} + (y_4 - y_2)\vec{j} + (z_4 - z_2)\vec{k} \end{aligned} \tag{A4}$$

2. Body-Nose Shapes

Numerical calculations are made for bodies with three different nose shapes. If the base diameter is used as a reference length, these shapes are given by Fig. 52.

(a) Power Series

$$r = \frac{1}{2}\left(\frac{x}{\lambda}\right)^n \tag{A5}$$

where λ is the fineness ratio of the nose (ℓ/d); n = 1 for a cone, and n = 1/2 for a parabola with a vertex at x = 0.

(b) Parabolic Series

$$r = \frac{1}{2}\left[\frac{2(x/\lambda) - K(x/\lambda)^2}{2 - K}\right] \qquad \text{(A6)}$$

where K = 0 for a cone, K = 1 for a parabolic nose, K = $\frac{3}{4}$ for a $\frac{3}{4}$ power parabolic series, and K = $\frac{1}{2}$ for a $\frac{1}{2}$ power parabolic series.

(c) Tangent Ogives

$$r = \frac{1}{2}\ 1 - 2R\left[1 - \ 1 - \frac{\lambda^2}{R^2}\ (1 - x^2)^2\ ^{1/2}\right]$$

where $\lambda = (R - 1/4)^{1/2}$ and R is the nose radius.

APPENDIX B

Velocity Calculations

The induced velocity at any field point Q due to a vortex filament (Fig. 53) can be calculated by using the Biot-Savart law[82]

$$\vec{V}_Q = \frac{\Gamma}{4\pi} \int \frac{\sin\alpha}{r^2} d\vec{s} \tag{B1}$$

For a finite vortex segment, (B1) reduces to

$$\vec{V}_Q = \frac{\Gamma}{4\pi h} (\cos\theta_2 - \cos\theta_1)\vec{e}_V \tag{B2}$$

where Γ is the vortex strength, h is the normal distance between the vortex segment and the field point, θ_1 and θ_2 are the angles between the vortex segments and the lines drawn from the field point to the vortex-segment end points, and $\vec{e}_V$ is a unit vector normal to the plane formed by the field point Q and the vortex segment. The last three parameters are also defined in Fig. 53.

In terms of the coordinates of the end points of the vortex-segment and the field point Q, the terms in Eq. (B2) can be rewritten as

$$\cos\theta_1 = -\frac{\vec{\ell}_1 \cdot \vec{R}_1}{|\vec{\ell}_1 \cdot \vec{R}_1|}, \quad \cos\theta_2 = \frac{\vec{\ell}_1 \cdot \vec{R}_2}{|\vec{\ell}_1 \cdot \vec{R}_2|} \tag{B3}$$

$$\vec{h} = \vec{R}_2 - \left(\frac{\vec{R}_2 \cdot \vec{\ell}_1}{|\vec{\ell}_1 \cdot \vec{\ell}_1|}\right)\vec{\ell}_1, \quad \vec{e}_V = \frac{\vec{R}_2 \times \vec{\ell}_1}{|\vec{R}_2 \times \vec{\ell}_1|} \tag{B4}$$

The total induced velocity for quadrilateral element,

$$\vec{V}_Q = \sum_{j=1}^{4} \vec{V}_{Qj} \tag{B5}$$

where the j stands for any of the four segments. When the field point is very close to the vortex segment, Eq. (B2) which is based on an inviscid flow is singular, and it is modified by a viscous-core type relation. Several models are available and are used in Refs. 83-85; however, all of them are problem-dependent and only a boundary-layer solution can provide an accurate and reliable account of the viscous effects. In the present method the following relations are used together with those used in Refs. 82-84.

and $\hat{\vec{V}}_Q = \vec{V}_G(1 - e^{-\lambda h2})$

$\hat{v}_Q = A\vec{V}_Q$ $\qquad A = 1 \qquad h \geq h_1$

$\qquad\qquad\qquad\qquad A = 0 \qquad h_1 \leq h \geq 0$

where $\hat{V}_Q$ is the modified induced velocity at the field point Q, λ ranges from 10 - 20 and h_1/ℓ_1 ranges from .001 - .005.

APPENDIX C

Influence Coefficient Equations

1. General Motion Description

We consider a thin delta wing in a uniform stream. Let $\vec{U}_\infty$ be the freestream velocity and oxyz be a body-fixed frame of reference. The wing edges lie in the xy-plane and the xz-plane is its plane of symmetry. The Euler angles α,β,γ are used to define the attitude of the wing or the wing-body combination (Fig. 54). They are defined by starting from a position where $\vec{U}_\infty$ is parallel to the x-axis and successively allow for the positive rotations α,β,γ about the y,z and x-axes, respectively.

The unit vector $\vec{e}_\infty$ in the direction of the free-stream velocity is expressed in terms of these angles and the base unit vectors of the body-fixed frame of reference by[86]

$$\bar{e}_\infty = \begin{bmatrix} 1 & 0 & 0 \\ 0 & \cos\gamma & \sin\gamma \\ 0 & -\sin\gamma & \cos\gamma \end{bmatrix} \begin{bmatrix} \cos\beta & \sin\beta & 0 \\ -\sin\beta & \cos\beta & 0 \\ 0 & 0 & 1 \end{bmatrix} \begin{bmatrix} \cos\alpha & 0 & -\sin\alpha \\ 0 & 1 & 0 \\ \sin\alpha & 0 & \cos\alpha \end{bmatrix} \begin{bmatrix} 1 \\ 0 \\ 0 \end{bmatrix}$$

or

$$\bar{e}_\infty = (\cos\alpha\cos\beta)\bar{i} + (\sin\alpha\sin\gamma - \cos\alpha\sin\beta\cos\gamma)\bar{j} + (\sin\alpha\cos\gamma + \cos\alpha\sin\beta\sin\gamma)\bar{k} \qquad (C1)$$

If the wing or wing-body combination is rotating with the angular velocity

$$\vec{\Omega} = \dot{\gamma}\vec{i} + \dot{\alpha}\vec{j}_1 + \dot{\beta}\vec{k}_2 \qquad (C2)$$

the projection of its components onto the xyz-axes gives

$$\vec{\Omega} = (\dot{\alpha}\sin\beta + \dot{\gamma})\vec{i} + (\dot{\alpha}\cos\beta\cos\gamma + \dot{\beta}\sin\gamma)\vec{j} + (\dot{\beta}\cos\gamma - \dot{\alpha}\cos\beta\sin\gamma)\vec{k} \tag{C3}$$

Thus, at any field point P(x,y,z,t), the velocity is given by

$$\begin{aligned}\vec{V}(\vec{r},t) = {} & [\frac{\partial\phi}{\partial x}(\vec{r},t) + U_\infty\cos\alpha\cos\beta + (\dot{\beta}\cos\gamma - \dot{\alpha}\cos\beta\sin\gamma)y \\ & - (\dot{\alpha}\cos\beta\cos\gamma + \dot{\beta}\sin\gamma)z]\vec{i} + [\frac{\partial\phi}{\partial y}(\vec{r},t) + U_\infty\sin\alpha\sin\gamma \\ & - U_\infty\cos\alpha\sin\beta\cos\gamma + (\dot{\alpha}\sin\beta + \dot{\gamma})z - (\dot{\beta}\cos\gamma - \dot{\alpha}\cos\beta\sin\gamma)X]\vec{j} \\ & + [\frac{\partial\phi}{\partial z}(\vec{r},t) + U_\infty\sin\alpha\cos\gamma + U_\infty\cos\alpha\sin\beta\sin\gamma \\ & + (\dot{\alpha}\cos\beta\cos\gamma + \dot{\beta}\sin\gamma)x - (\dot{\alpha}\sin\beta + \dot{\gamma})y]\vec{k}\end{aligned} \tag{C4}$$

where ϕ is the disturbance potential.

2. Influence Equations

Application of the no-penetration boundary condition leads to the following set of simultaneous algebraic equations:

$$\begin{aligned}(\vec{\Omega} \times \vec{r} - U_\infty\vec{e}_\infty) \cdot \vec{n} = {} & \sum_{i=1}^{N_S}\vec{V}_S(\vec{r},t)\Gamma_S(\vec{r},t) \cdot \vec{n} + \sum_{i=1}^{N_L}\vec{V}_L(\vec{r},t)\Gamma_L(\vec{r},t) \cdot \vec{n} \\ & + \sum_{i=1}^{N_T}\vec{V}_T(\vec{r},t)\Gamma_T(\vec{r},t) \cdot \vec{n} + \sum_{i=1}^{N_B}\vec{V}_B(\vec{r},t)\Gamma_B(\vec{r},t) \cdot \vec{n} \\ & + \sum_{i=1}^{N_{SH}(t)}V_{SH}(\vec{r},t)\Gamma_{SH}(\vec{r},t) \cdot \vec{n}\end{aligned} \tag{C5}$$

where $\vec{V}$ is the induced velocity by an element, Γ is the circulation of the element and N is the number of elements. Here, the subscripts S, L, T, B and SH refer, respectively, to the wing surface, leading edge wake, trailing edge wake, body surface and shed vortices. We note that N_{SH} is replaced by a finite number of time steps. Equation (C5) can be rewritten in matrix form as

$$[A_{ij}][\Gamma_j] = [C] \tag{C6}$$

where $[A_{ij}]$ is called the influence coefficient matrix.

To simplify the numerical procedure, we partition the matrix $[A_{ij}]$ as

$$[A]\begin{bmatrix}\Gamma_B\\ \\ \Gamma_W\end{bmatrix} = \begin{bmatrix}BB & BS\\ \\ SB & SS\end{bmatrix}\begin{bmatrix}\Gamma_B\\ \\ \Gamma_W\end{bmatrix} = \begin{bmatrix}C_B\\ \\ C_W\end{bmatrix} \tag{C7}$$

where BB, SB, BS and SS represent, respectively, the influence of the body elements on the body control points, the body elements on the wing control points, the wing elements on the body control points and the wing elements on the wing control points.

3. Source of Unsteadiness

In general, the unsteady motion of the wing or wing-body combination can be described by a function f(t) which is assumed to be a known deterministic function of time, but need not be periodic. As an example taking a time-varying angle of attack of the form $\dot{\alpha} = f(t)$, we discretize it as

$$\alpha(t_{i+1}) = \alpha(t_i) + (t_{i+1} - t_i)f(t_i) \tag{C8}$$

where $\alpha(t_i)$ is the angles of attack at the nondimensional time step t_i.

APPENDIX D

Solvers of Simultaneous Equations

In general, all finite-element methods give rise to a system of linear algebraic equations whose solution often constitutes a major part of the computational time, thereby imposing a constraint on the complexity of the configurations which can be solved.

In Ref. 87, a detailed comparison is made between the different methods of solving simultaneous algebraic equations. A short summary follows:

1. Direct Methods

(a) In the direct methods such as the Gauss elimination, the number of operations performed is independent of the accuracy desired. Thus, the accuracy of the solution is a function of the condition and size of the matrix.

(b) The original matrix is altered as the computation proceeds and there is no particular advantage to be gained when the matrix has a large number of zeros.

(c) Most of the direct methods apply to quite general real or complex matrices.

(d) Storage requirements are almost the same for most of the general direct methods, a minimum of about $n^2 + rn$, where r is the numbers of the right-hand sides and n is the number of equations. The number of arithmetic operations is approximately $\frac{2}{3} n^3$.

(e) In most cases of a large number of equations, the round-off error tends to be large; this can be cured partially by using double-precision arithmetic.

2. Iterative Methods

(a) In general, iterative methods, such as Gauss-Seidel, are preferred for solving large systems of equations which are strongly diagonal, sparse or banded. In these cases, convergence is known to be rapid.

(b). Round-off errors in iterative methods are small compared with those of the direct methods; the accuracy of the solutions depends upon the number of iterations performed, the condition of the matrix as well as its size and the particular algorithm being used.

(c) The total number of arithmetic operations depends upon the convergence rate and the desired accuracy; slow or irregular convergence is a considerable drawback. The number of arithmetic operations is approximately $2n^2$ per iteration; thus the number of iterations needed for the desired accuracy must be less than $\frac{1}{3}$ n for this technique to be superior to the elimination method. The storage requirement varies with the matrix being used and it is roughly $n^2 + 3n$.

3. Householder Method

For rectangular matrices which arise if some constraints are imposed, the solution can only be obtained in a least-squares sense. In this case, the Householder method is the most suitable because it performs the least-square operation and triangularization simultaneously[50].

From the previous discussion, it is evident that the selection of a suitable method is problem dependent. When $n \leq 100$, the Gauss elimination is preferred. When $150 < n < 1000$, the Gauss-Siedel or a successive over relaxation method is preferred. When $n > 2000$, a Monte-Carlo type method is recommended.

APPENDIX E

Total and Distributed Loads

The distribution of the pressure coefficient is calculated by using the Bernoulli equation in terms of a body-fixed frame of reference; that is,

$$C_{p_{1,2}}(\vec{r}_j,t_k) = -[\vec{V}_{1,2}(\vec{r}_j,t_k)]^2 + 2\vec{V}_{1,2}(\vec{r}_j,t_k)\cdot[\vec{\Omega}(t_k)x\vec{r}_j - \vec{e}_\infty] - 2\frac{\partial\phi}{\partial t}(\vec{r}_j,t_k) \tag{E1}$$

where the subscripts 1 and 2 refer to the upper and lower surfaces of the configuration.

When calculating the velocity on the surface of any configuration or in the wake, one must account for the induced tangential velocity due to the local strength of the vortex sheet. In Fig. 55, we show the parameters involved in calculating the components of the local tangential velocity at a point p for a quadrilateral vortex element in the xy-plane. Using linear interpolation, we obtain

$$\vec{v}_{\tau x}(z = 0^{+}_{-}) = \pm\frac{1}{2\ell_1^2}[\Gamma_1(x - x_1 + \ell) + \Gamma_3(x - x_1)]\vec{e}_1$$
$$\vec{v}_{\tau y}(z = 0^{+}_{-}) = \mp\frac{1}{2\ell_2^2}[\Gamma_4(y + \ell_2 - y_1) + \Gamma_2(y - y_1)]\vec{e}_2 \tag{E2}$$

Thus, Eq. (E1) can be rewritten as

$$C_{p_{1,2}}(\vec{r}_j,t_k) = -[\nabla\phi(\vec{r}_j,t_k) \pm v_{\tau x}(\vec{r}_j,t_k)\vec{i} \pm v_{\tau y}(\vec{r}_j,t_k)\vec{j}]^2 + 2[\nabla + (\vec{r}_j,t_k) \pm v_{\tau x}(\vec{r}_j,t_k)\vec{i} \pm v_{\tau y}(\vec{r},\vec{t}_k)j] \cdot [\vec{\omega}(t_k)x\vec{r}_j - \vec{e}_\infty] - 2\frac{\partial\phi}{\partial t}(\vec{r}_j,t_k) \tag{E3}$$

For steady flows, the last term on the right-hand side of Eq. (E3) vanishes and all other terms are time independent. But for unsteady-flows this term needs to be calculated. It involves calculating the local rate of change of the disturbance velocity potential which is very tedious and time consuming. Therefore, only the net pressure force is calculated as follows.

$$\Delta C_p = C_{p_1} - C_{p_2} = 4[\vec{V}_{\tau x}(r_j,t_k) + \vec{V}_{\tau y}(r_j,t_k)] \cdot [\vec{\omega}(t_k)x\vec{r}_j - \vec{e}_\infty - \nabla\phi(\vec{r}_j,t_k)] - 2[\Gamma(\vec{r}_j,t_k) - \Gamma(\vec{r}_j,t_{k-1})/(t_k - t_{k-1})] \tag{E4}$$

where

$$\vec{V}_{1,2}(\vec{r}_j,t) = \nabla\phi(\vec{r}_j,t) \pm \vec{v}_{\tau x}(\vec{r}_j,t) \pm \vec{v}_{\theta y}(\vec{r}_j,t) \tag{E5}$$

From Eq. (E4), the total forces and moments acting on the configuration can then be calculated. The normal force, tangential force and pitching moment for an element are given by

$$N_i = A_i C_{p_i} \cos\theta_i \cos\delta_i \tag{E6}$$

$$T_i = - A_i C_{p_i} \sin\delta_i \tag{E7}$$

$$M_i = N_i x_i - T_i z_i \tag{E8}$$

where A_i is the elemental area, x_i and z_i are the coordinates of the control point of the element, and θ_i and δ_i are the panel or element inclination angles about the z and x axes. The total force and moment coefficients acting on the configuration are obtained by summing the panel forces and moments on both sides of the plane of symmetry; that is

$$C_N = \frac{1}{A_t} \sum_i 2N_i$$
$$C_T = \frac{1}{A_t} \sum_i 2T_i \qquad \text{(E9)}$$
$$C_M = \frac{1}{A_t \bar{c}} \sum_i 2M_i$$

Then, the lift and induced drag coefficients are given by

$$C_L = C_N \cos\alpha - C_T \sin\alpha$$
$$C_D = C_N \sin\alpha + C_T \cos\alpha \qquad \text{(E.10)}$$

Alternatively, the total forces and moments can be obtained by using the Kutta-Joukowsky theorem, which for steady flows gives the force acting on a vortex segment as

$$\bar{F}_i = 2\ell_i \vec{\Gamma}_i x \vec{V}_i \qquad \text{(E11)}$$

where ℓ_i is the nondimensional length of the segment on which the force $\vec{F}_i$ acts, $\vec{\Gamma}_i$ is the circulation around this segment multiplied by a unit vector parallel to the segment and $\vec{V}_i$ is the velocity at the midpoint of the segment. The resultant force is obtained by summing the forces on all the elements of the configuration. The lift, induced drag and the pitching moment coefficients can then be obtained by using Eqs. (E9) and (E10).

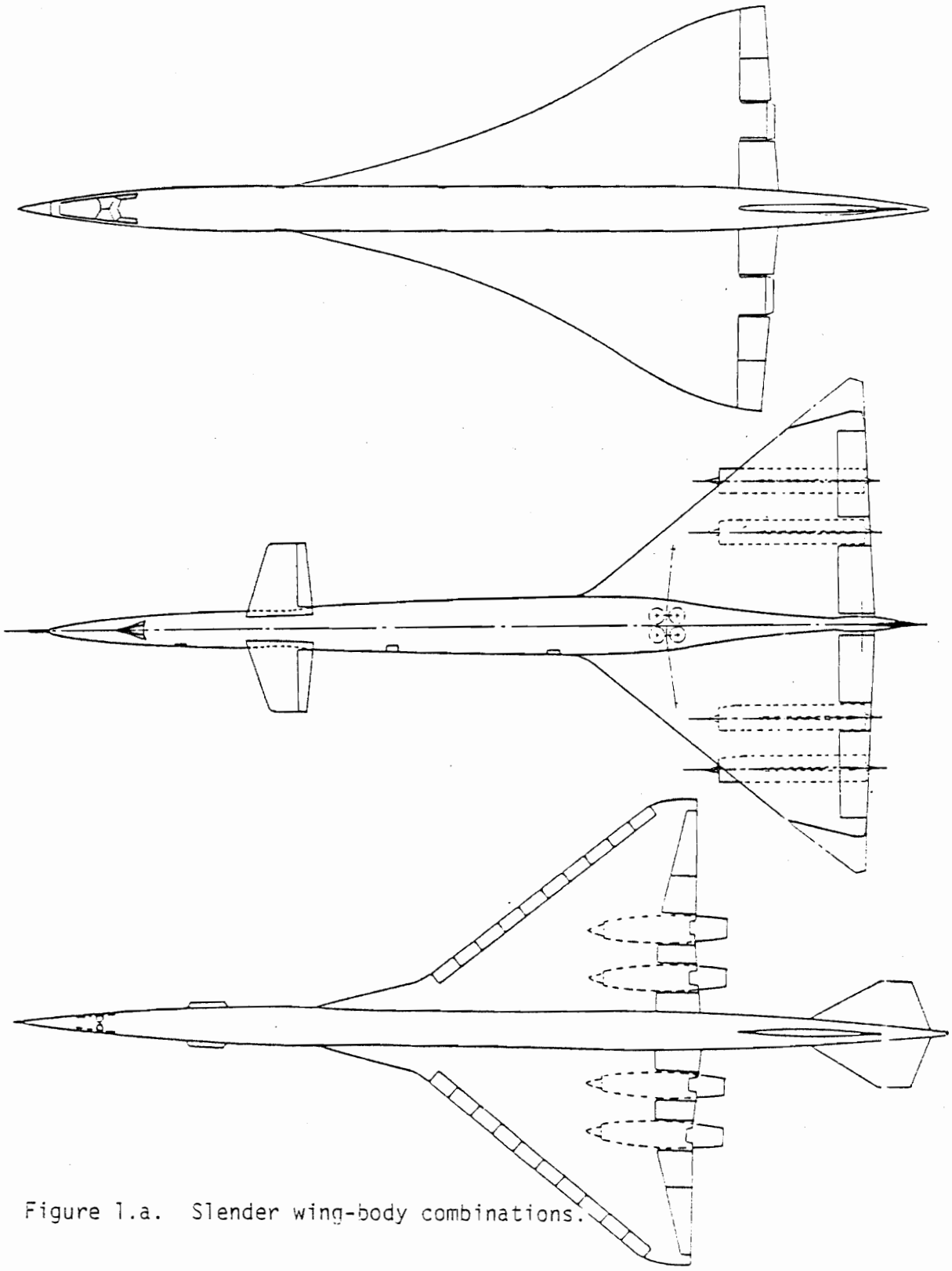

Figure 1.a. Slender wing-body combinations.

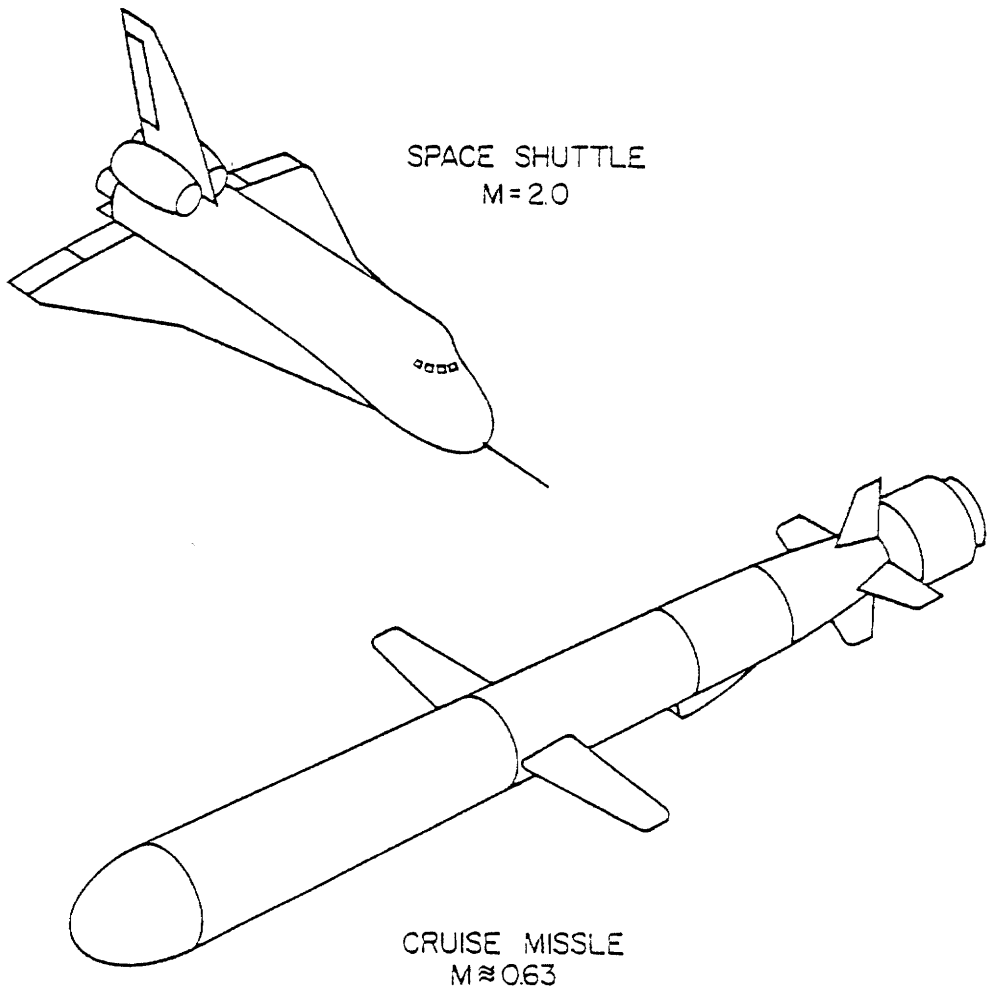

Figure 1.b. Slender wing-body combinations

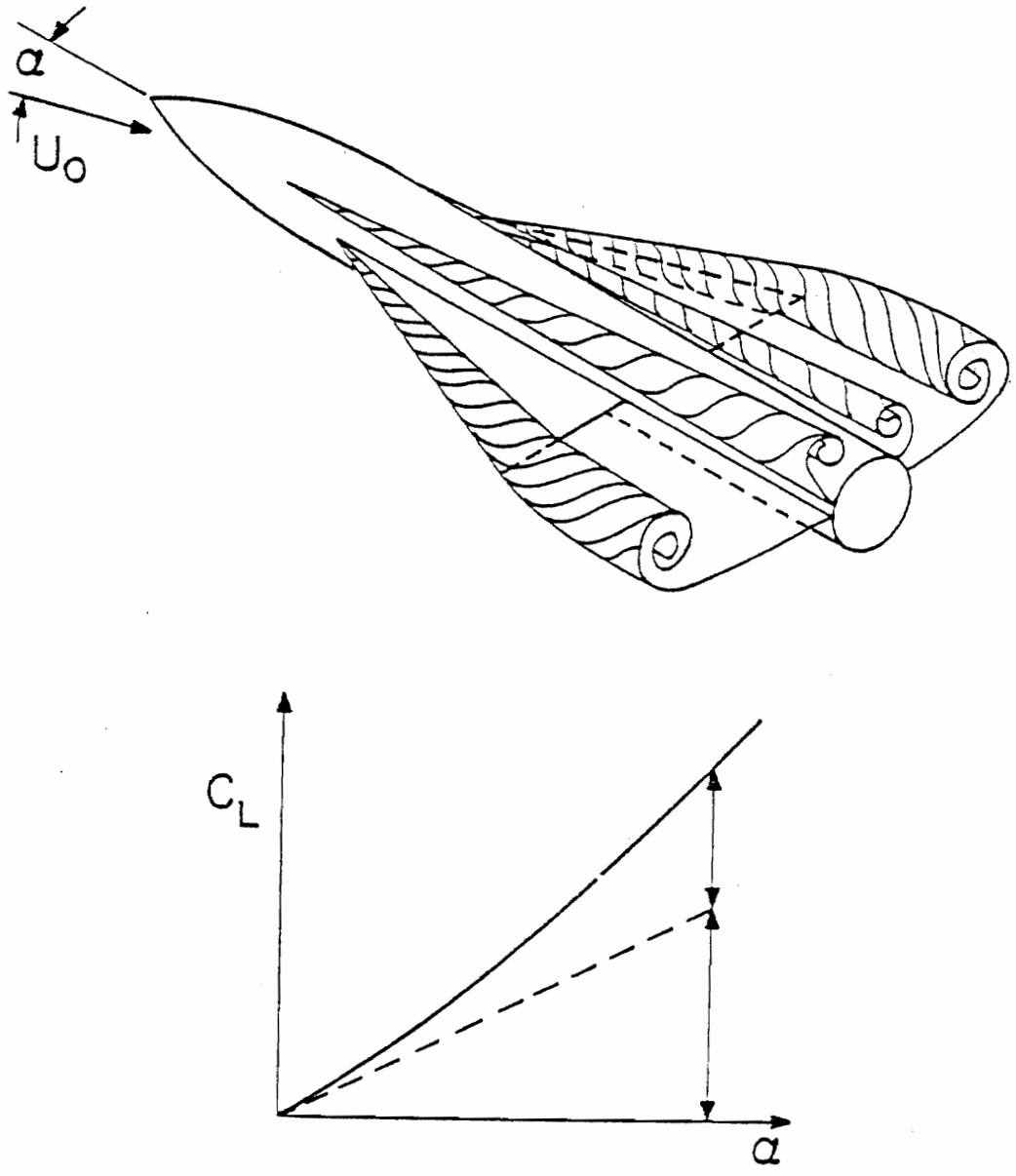

Figure 2. A wing-body combination at a high angle of attack.

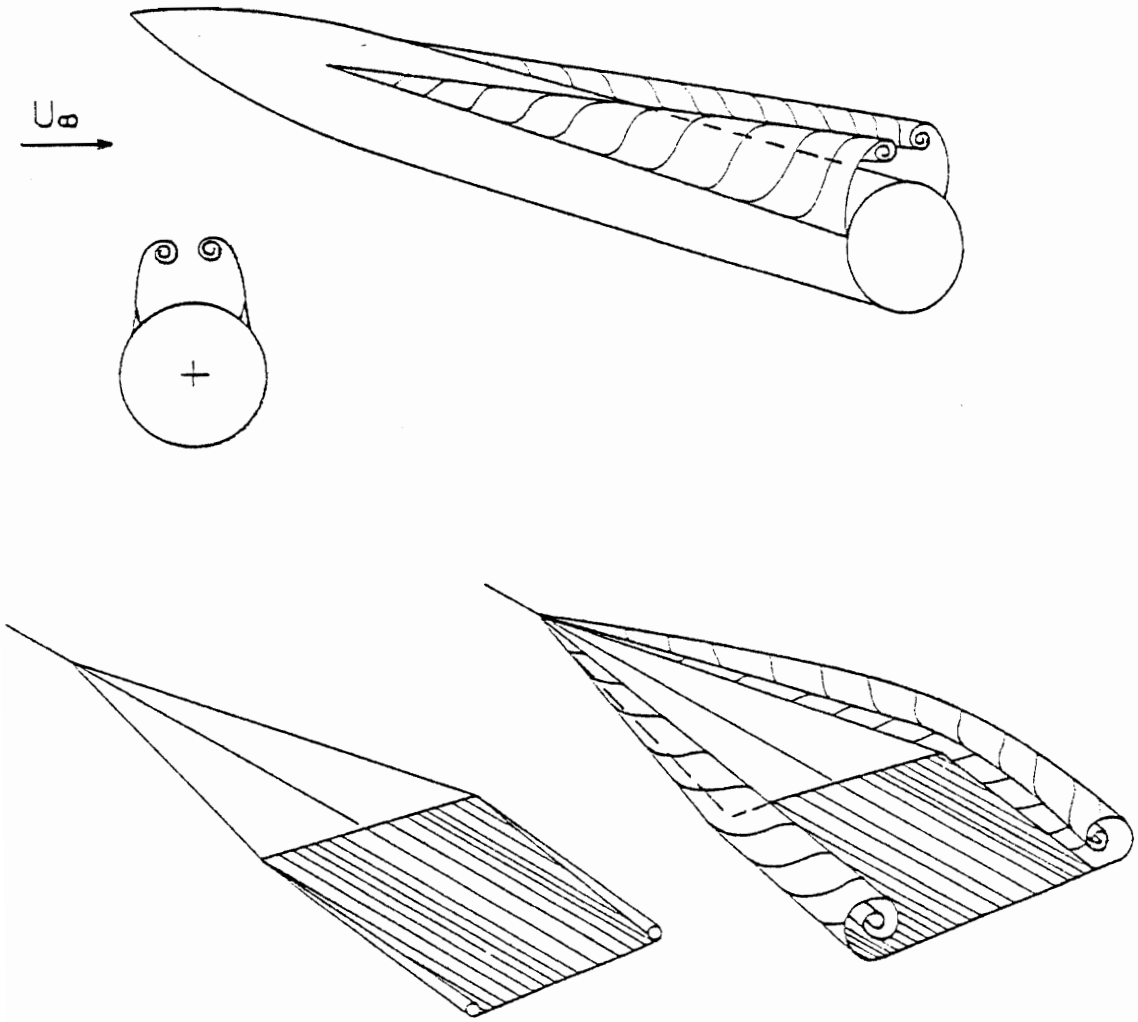

Figure 3. Flow structure at low and high angles of attack.

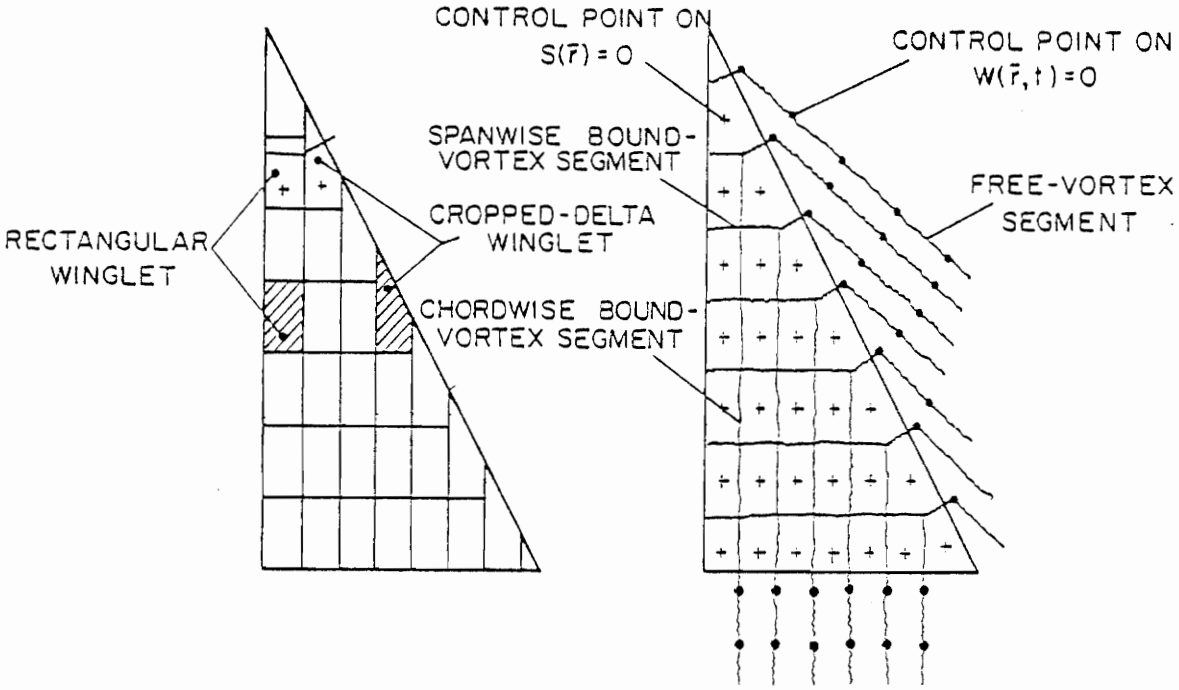

a. Discretization of wing into winglets

b. Discrete-vortex system

Figure 4. Lattice arrangement for a delta wing.

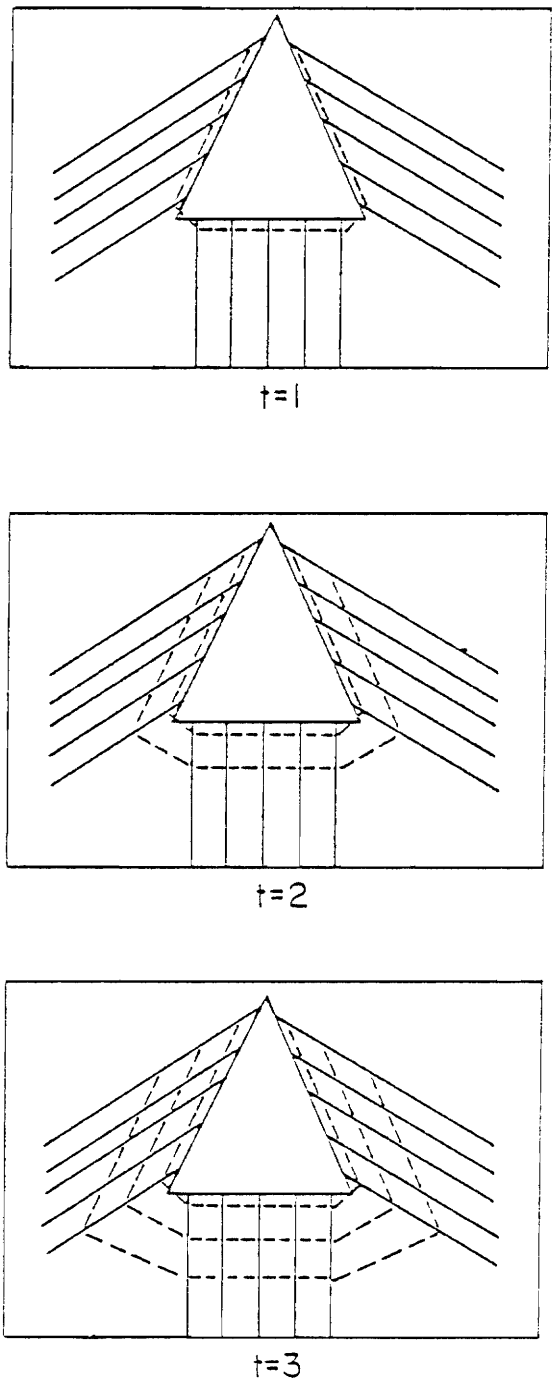

Figure 5. Schematic representation of the growth of wake for a delta wing in unsteady motion.

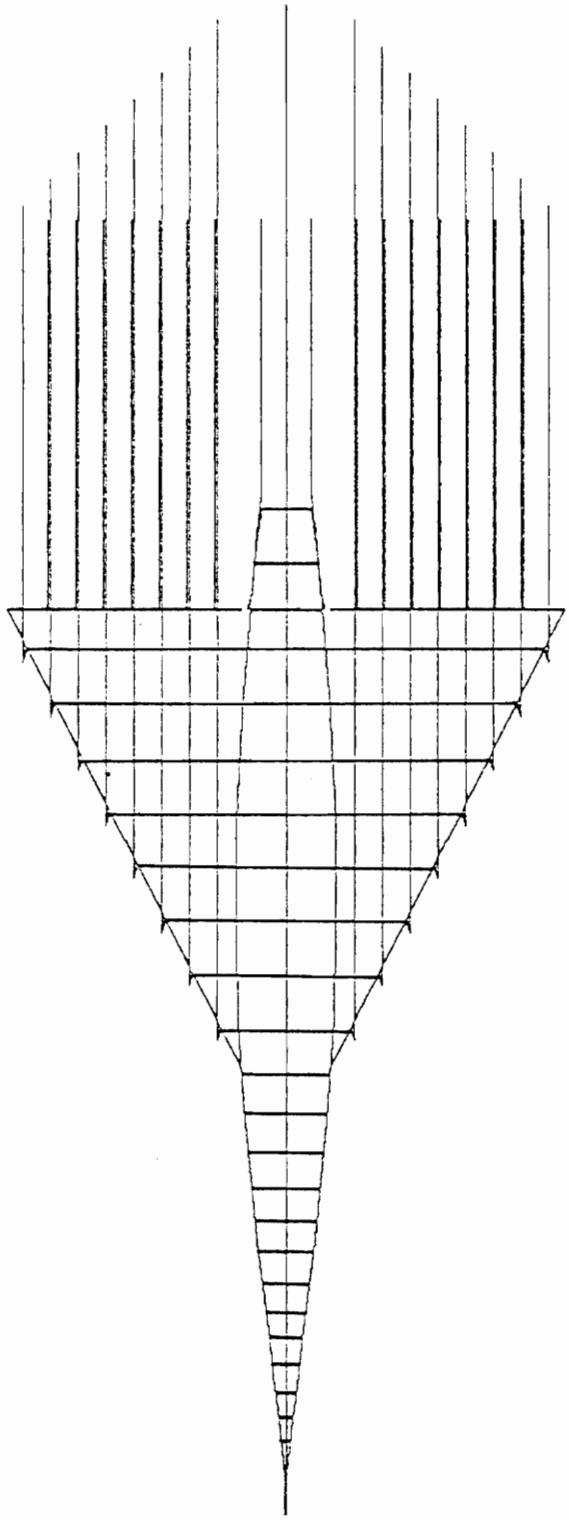

Figure 6. Vortex lattice for a wing-body combination.

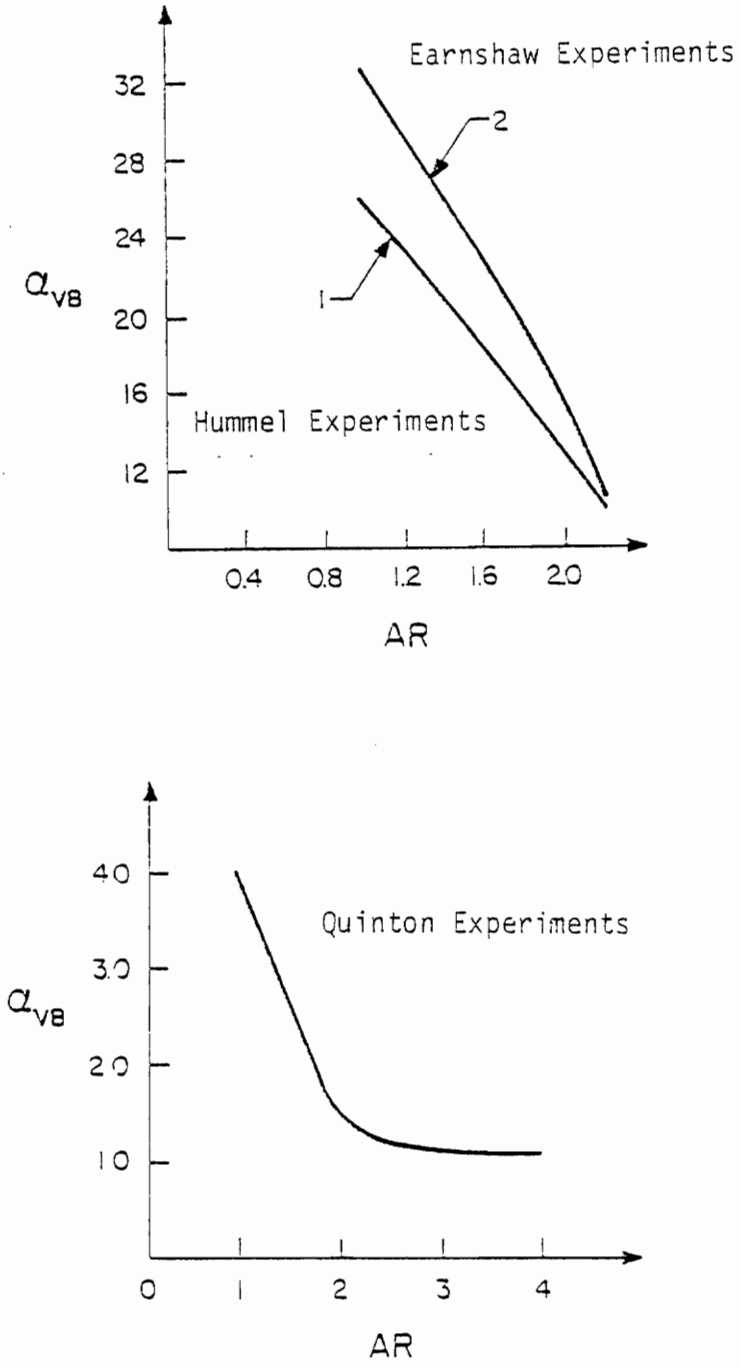

Figure 7. Vortex breakdown angle.

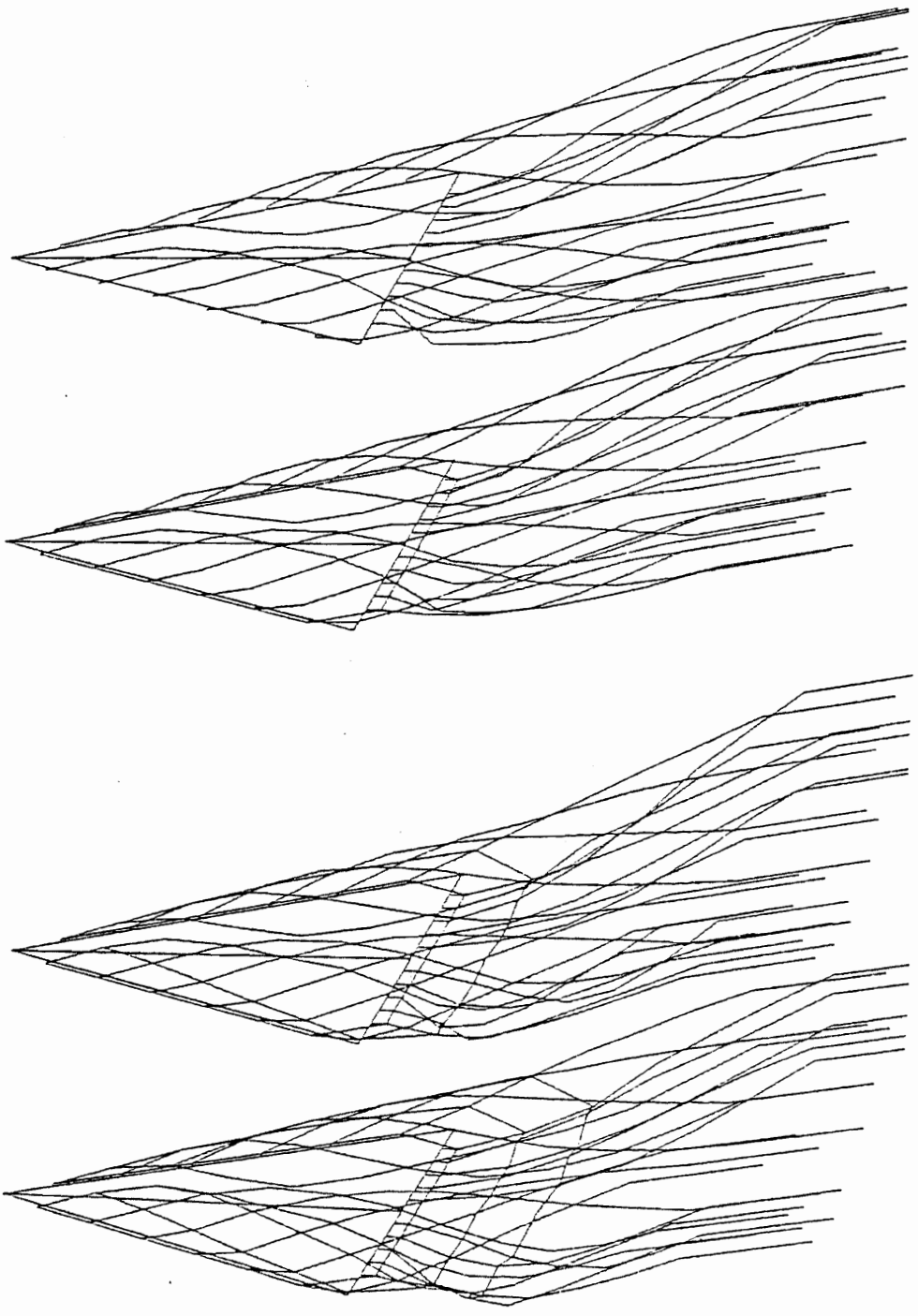

Figure 8. Solution of the unsteady wake for a delta wing (AR = 1, $\alpha = 15° + 4 \sin \frac{\pi t}{6}$, 6 x 6 lattice).

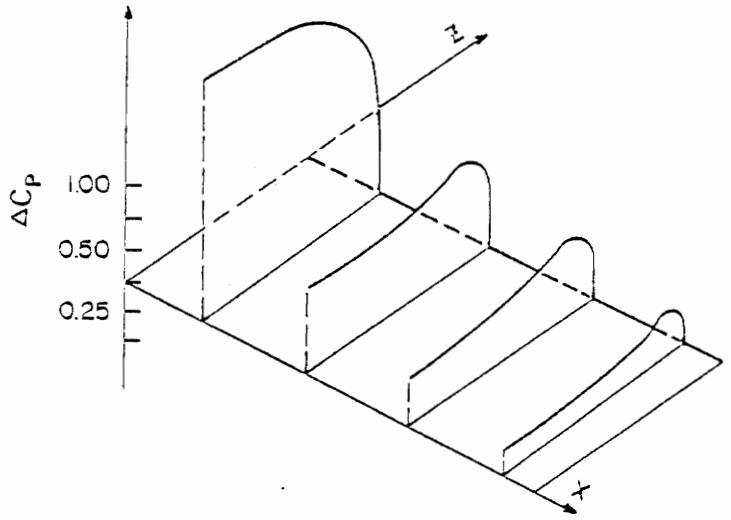

Figure 9. Transient pressure-coefficient distribution for a rectangular wing, AR = 1, α = 15 + 4 sin $\frac{\pi t}{6}$, t = 4, 4 x 4 lattice.

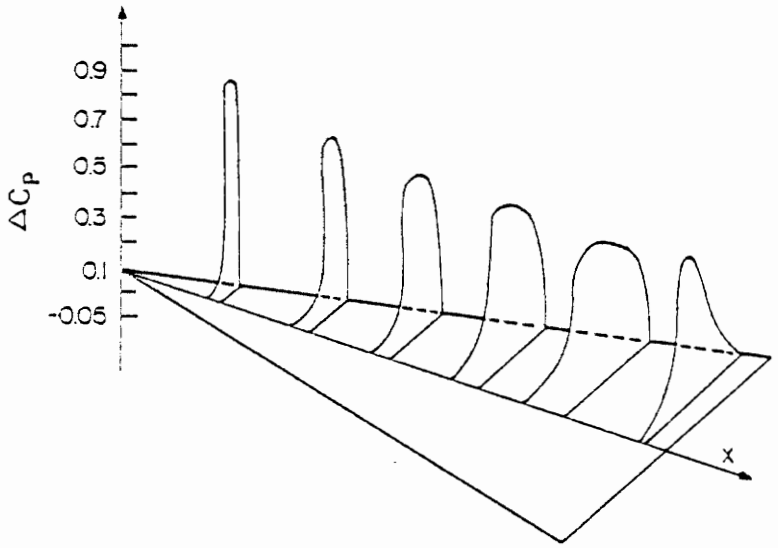

Figure 10. Transient pressure-coefficient distribution for a delta wing AR = 1, α = 15° + 4 sin $\frac{\pi t}{6}$, t = 3, 6 x 6 lattice.

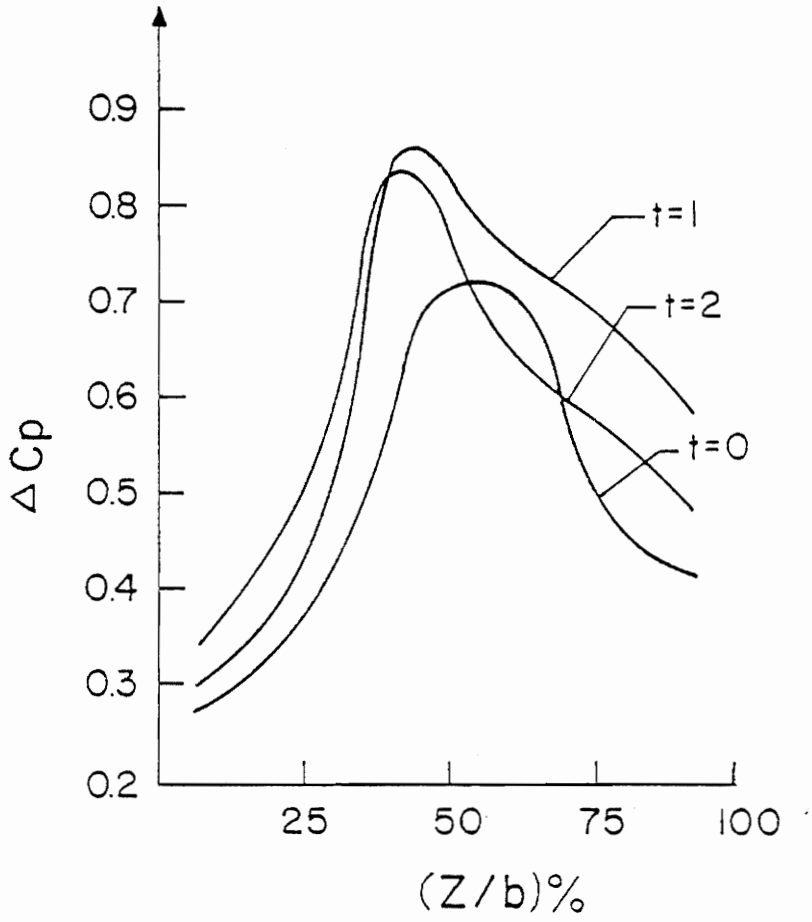

Figure 11. Spanwise variation of the pressure-coefficient distribution for a delta wing, AR = 1, $\alpha = 15° + 4 \sin \frac{\pi t}{6}$, x/c_r = 83% 6 x 6 lattice.

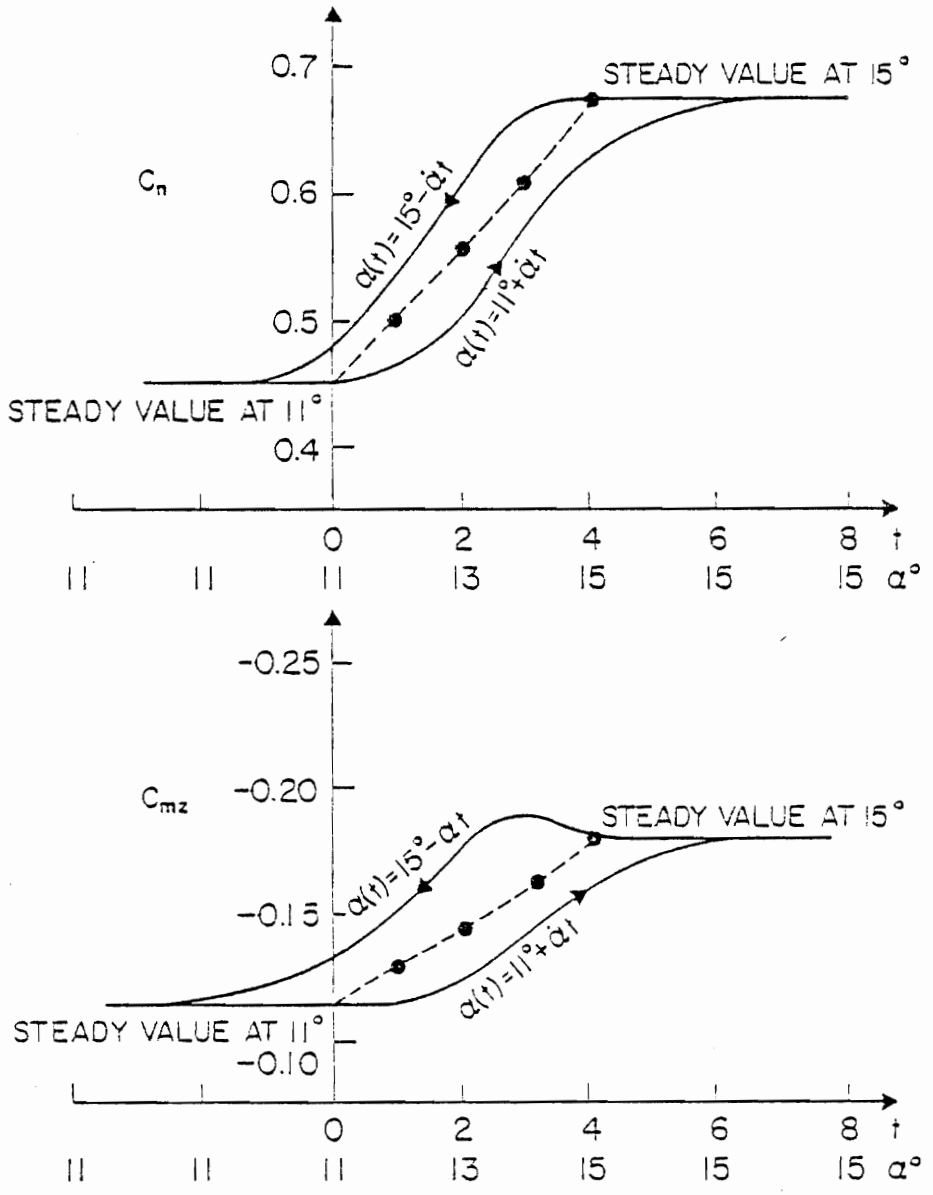

Figure 12. Variation of the normal-force and pitching moment coefficients with increasing and decreasing angle of attack.

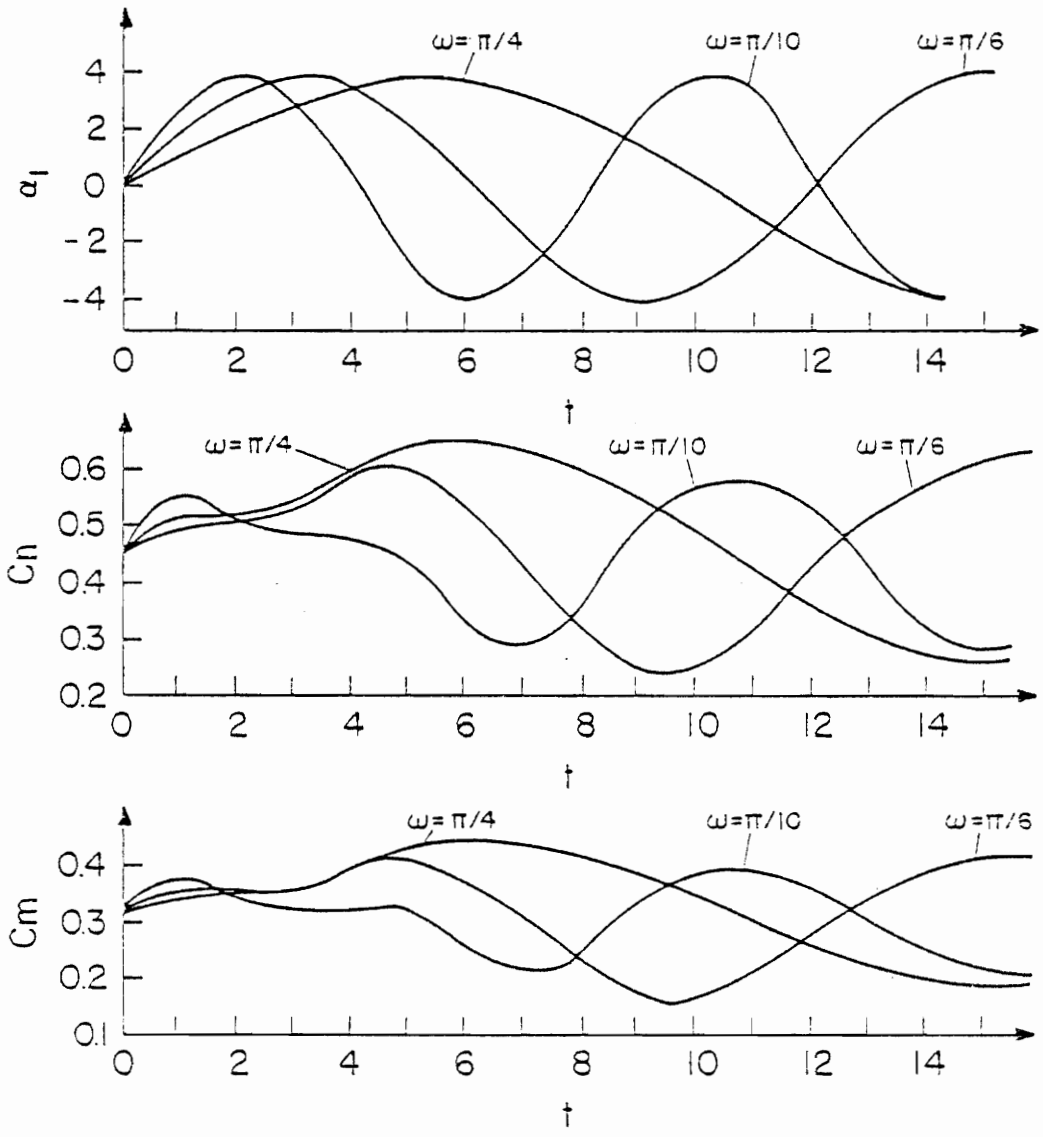

Figure 13. Variation of the pitching-moment and the normal-force coefficients for a delta wing, AR = 1, $\alpha = 15° + 4 \sin\omega t$, 4 x 4 lattice.

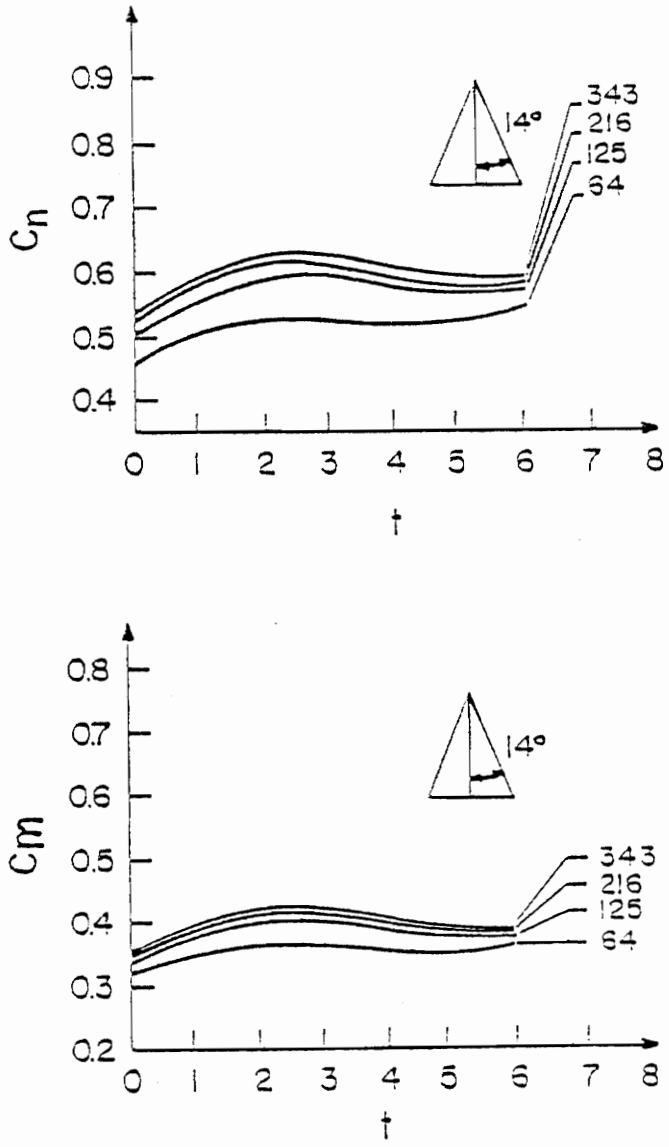

Figure 14. Variation of the normal force and pitching moment coefficients for a delta wing with increasing number of elements, AR = 1, $\alpha = 15° + 4 \sin \frac{\pi t}{6}$.

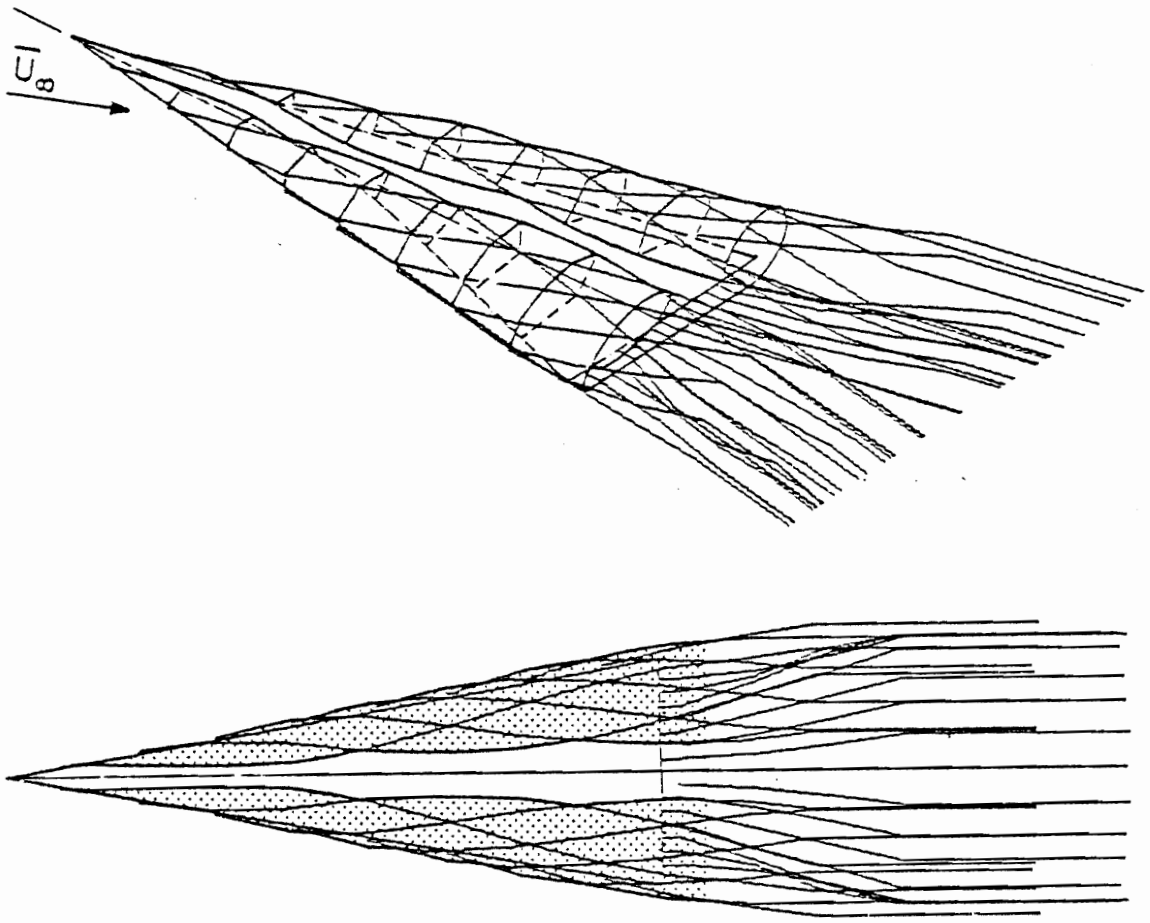

Figure 15. Wake shape of a delta wing in a steady symmetric flow, $\alpha = 15°$, $\beta = 0.0$, 8 x 8 bound lattice, AR = 0.7.

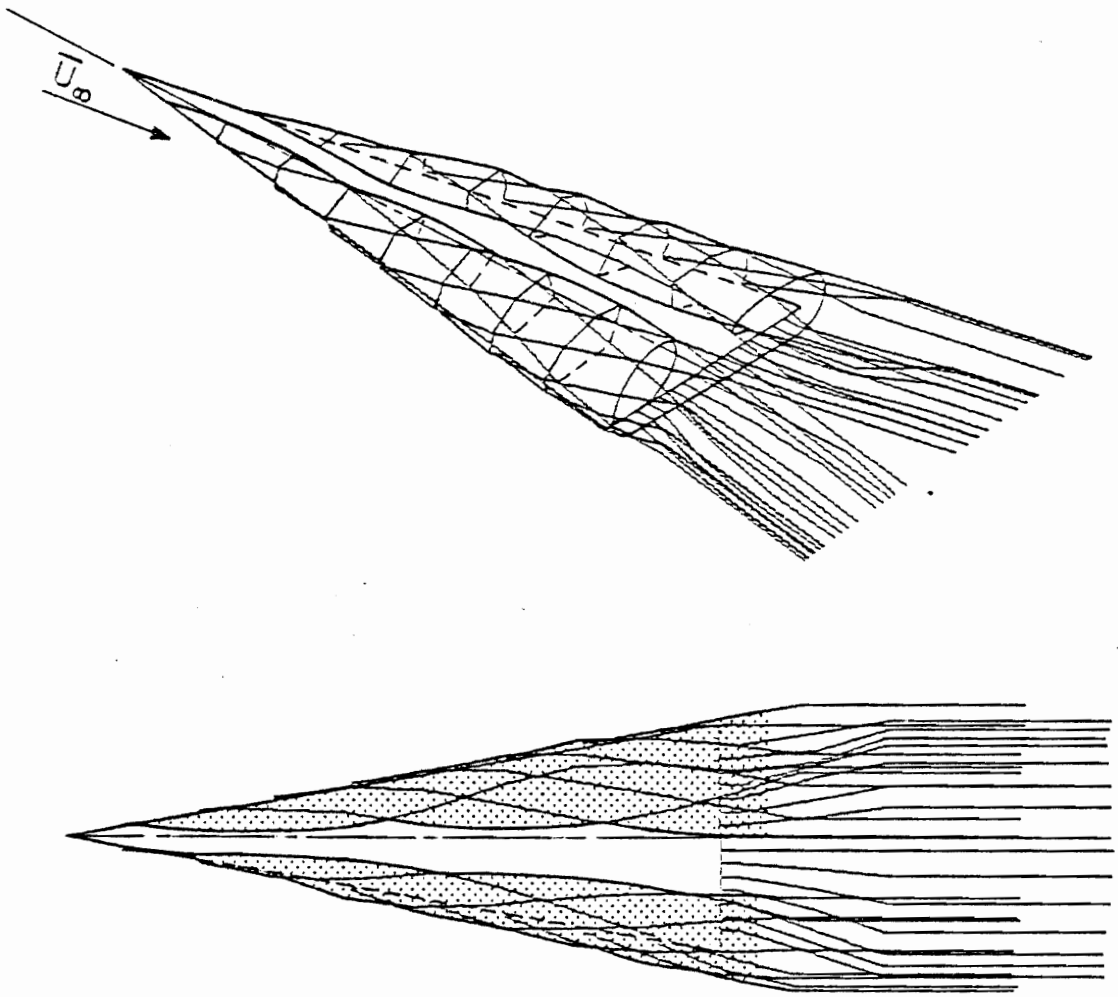

Figure 16. Wake shape of a yawed delta wing in a steady flow, α = 15°, β = 5°, 8 x 8 bound lattice, AR = 0.7.

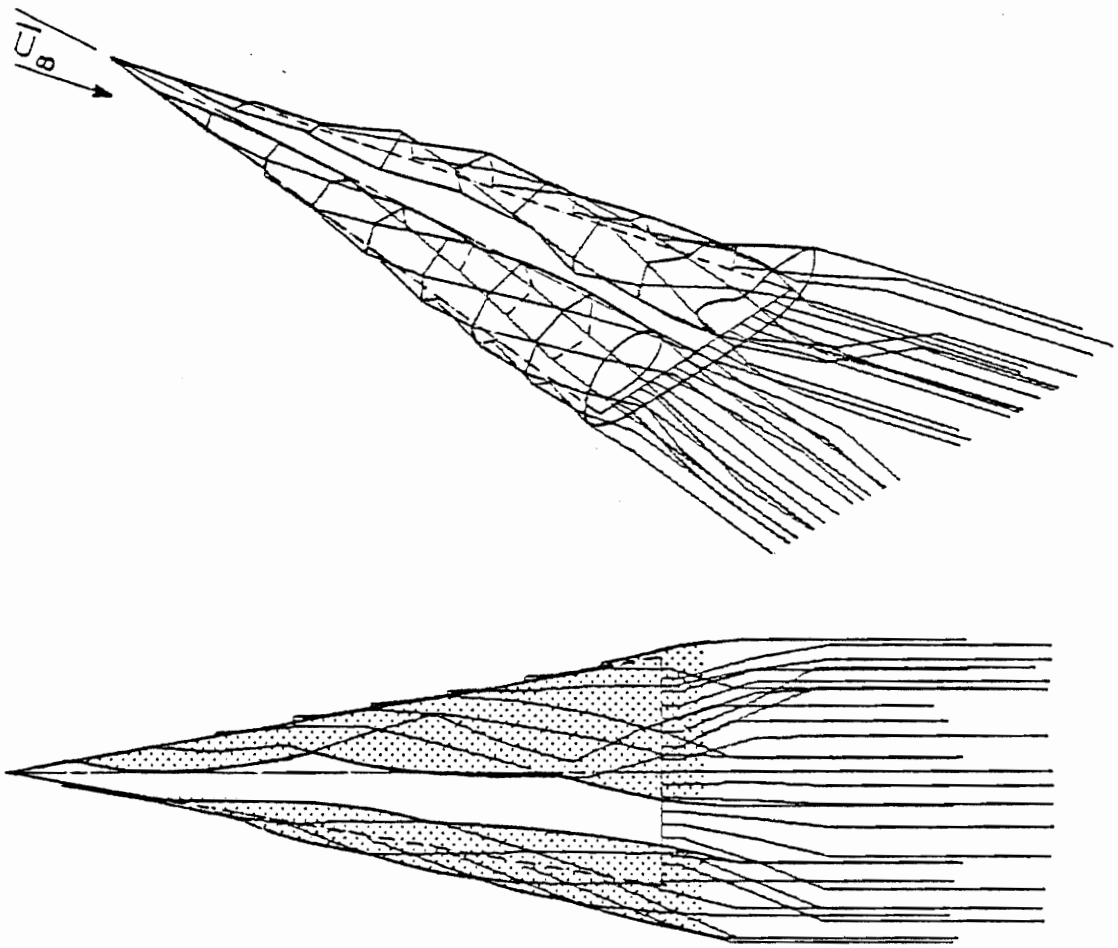

Figure 17. Wake shape of a yawed delta wing in a steady flow, α = 15°, β =10°, 8 x 8 bound lattice, AR = 0.7.

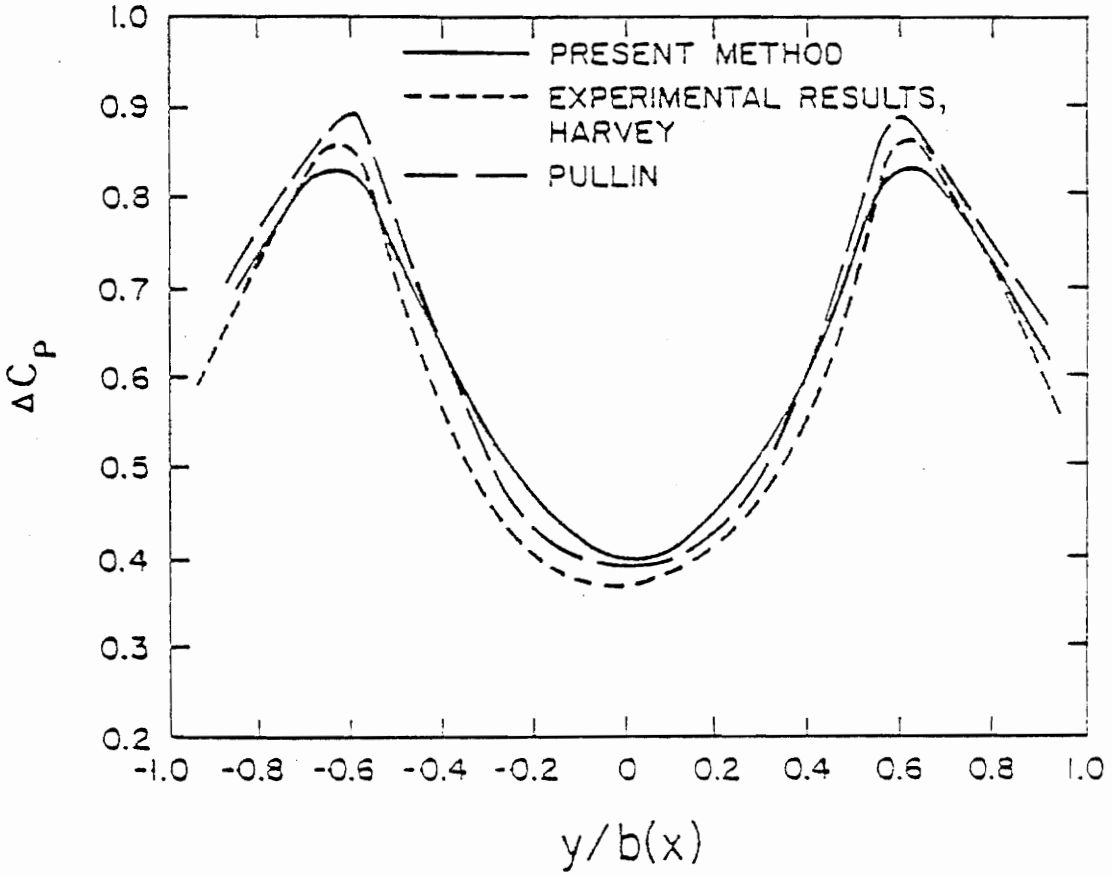

Figure 18. Net spanwise pressure distribution on a delta wing, α = 15°, β = 0, 8 x 8 bound lattice, AR = 0.7, x/c_r = 0.395.

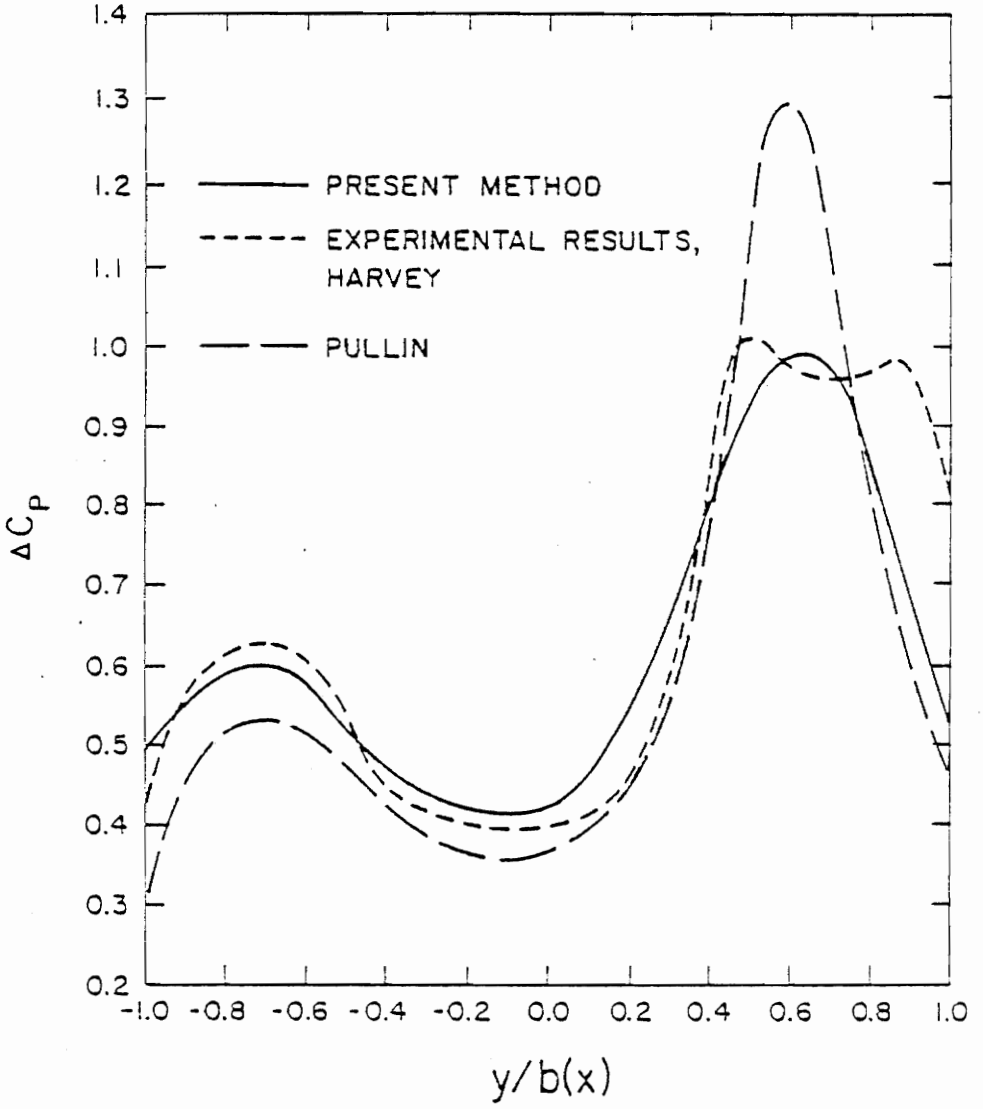

Figure 19. Net spanwise pressure distribution on a yawed delta wing, α = 15°, β = 5°, 8 x 8 bound lattice, AR = 0.7, x/c_r = 0.395.

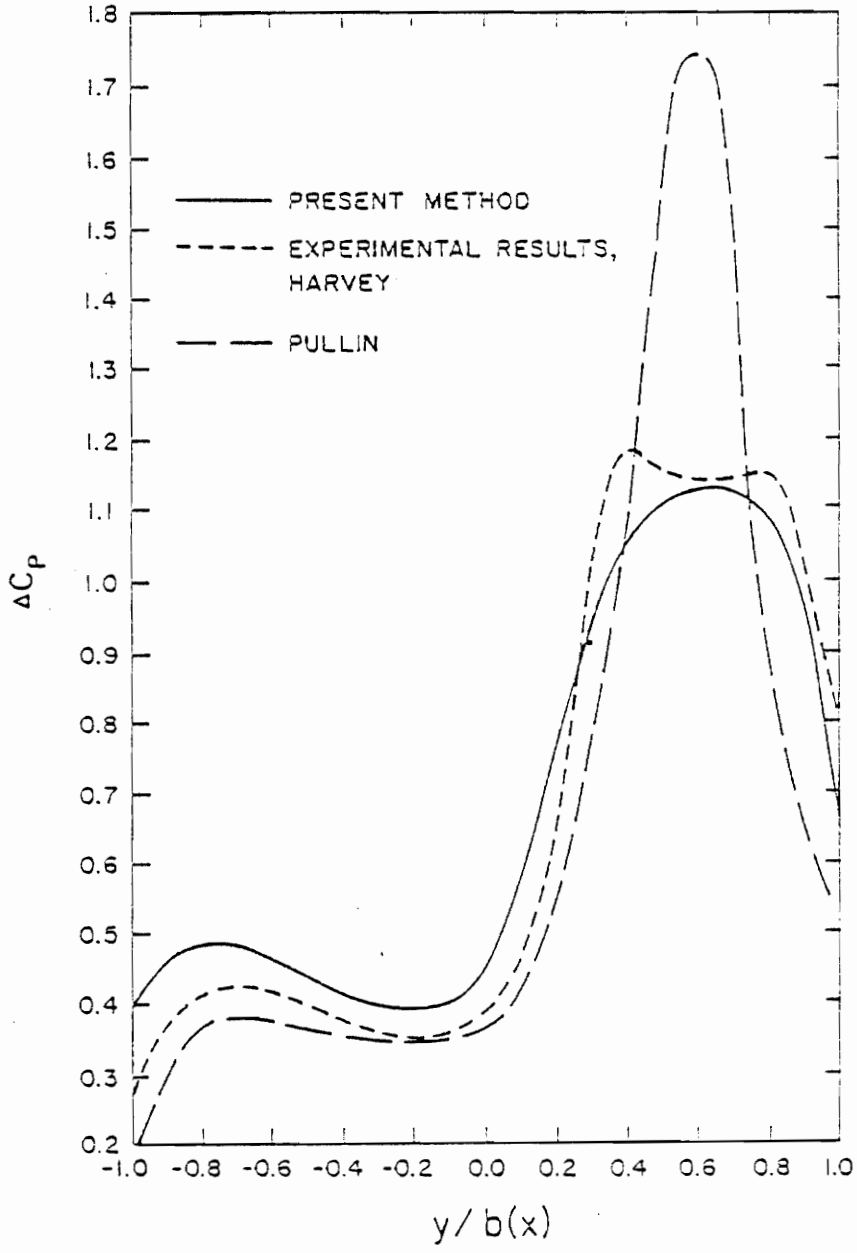

Figure 20. Net spanwise pressure distribution on a yawed delta wing, α = 15°, β = 10°, 8 x 8 bound lattice, AR = 0.7, x/c_r = 0.395.

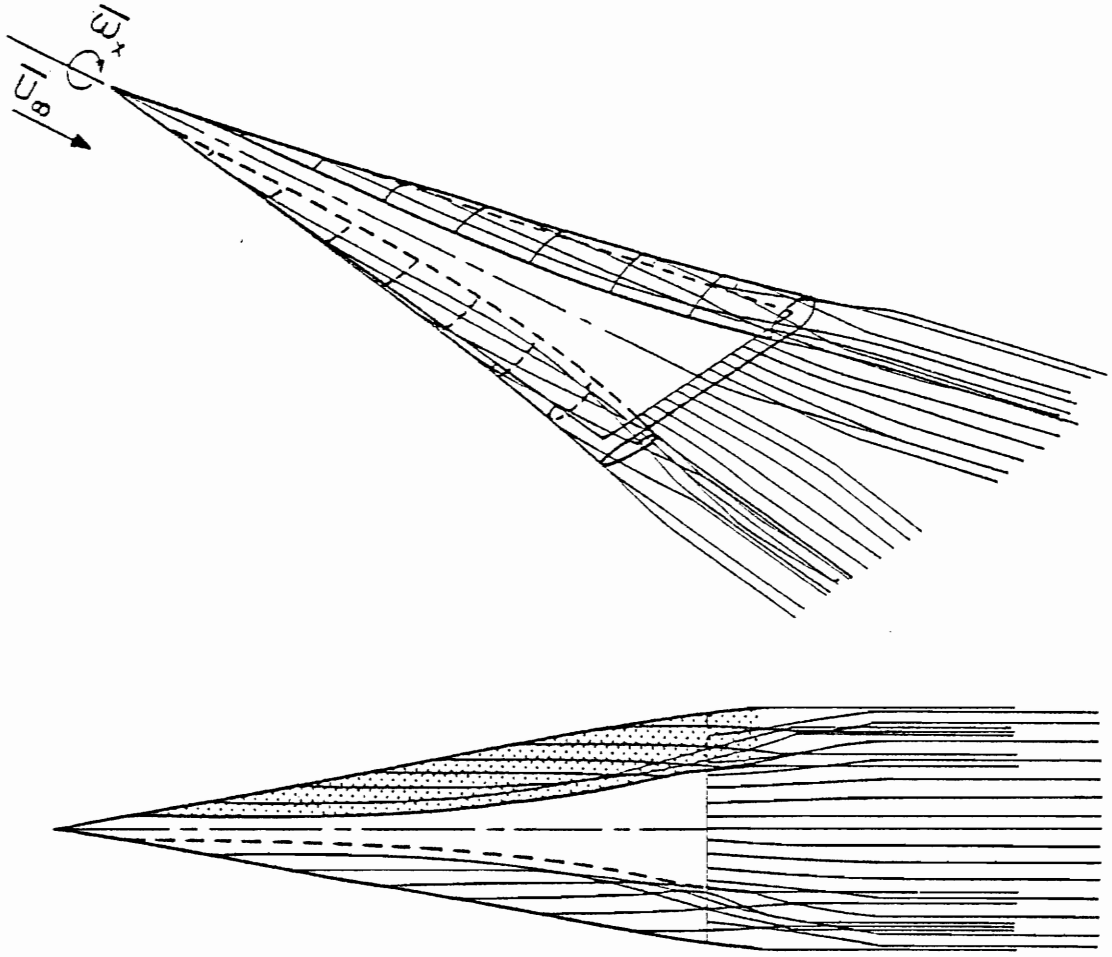

Figure 21. Wake shape of a steadily rolling delta wing, $\omega_x = -0.2$, $\alpha = 0°$, 8 x 8 bound lattice, AR = 0.7.

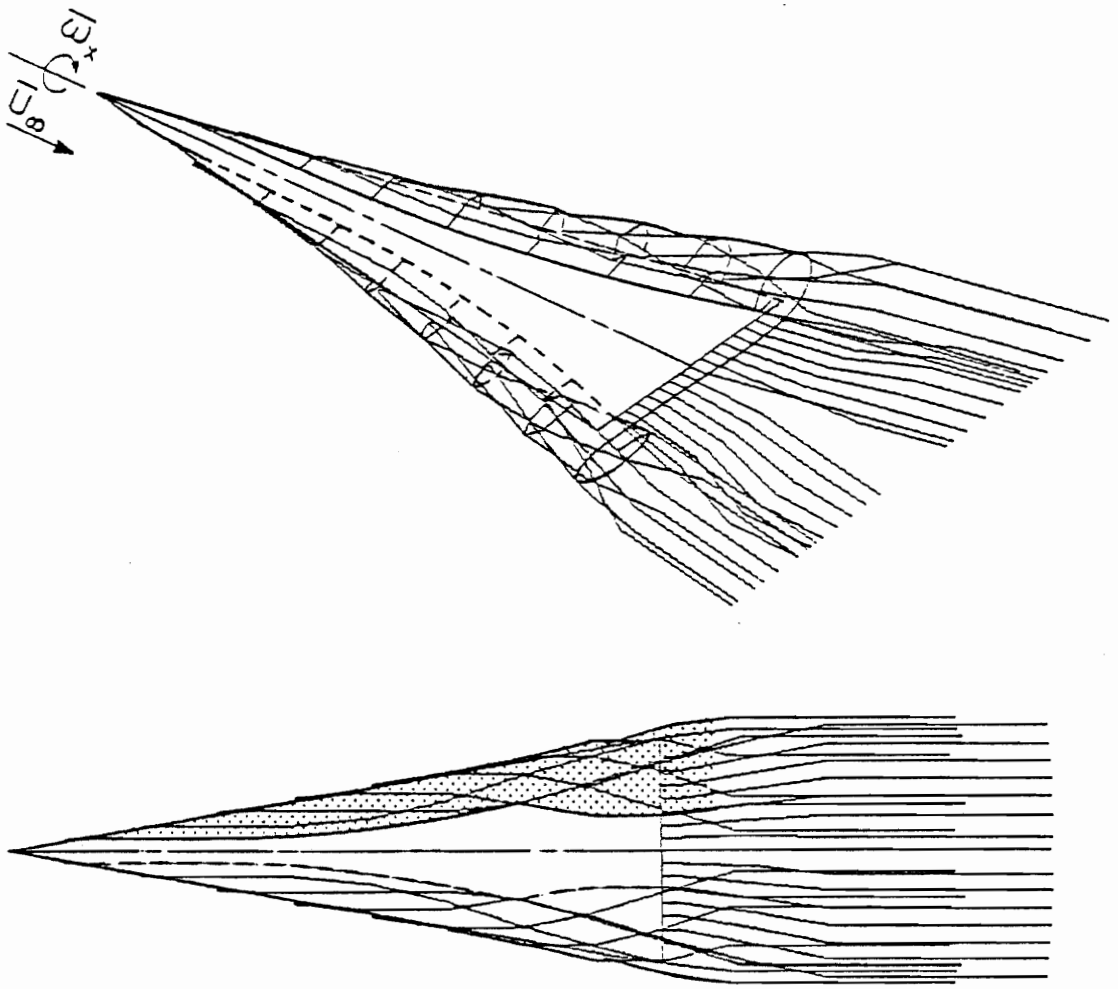

Figure 22. Wake shape of a steadily rolling delta wing, $\omega_x = -0.4$, $\alpha = 0°$, 8 x 8 bound lattice, AR = 0.7.

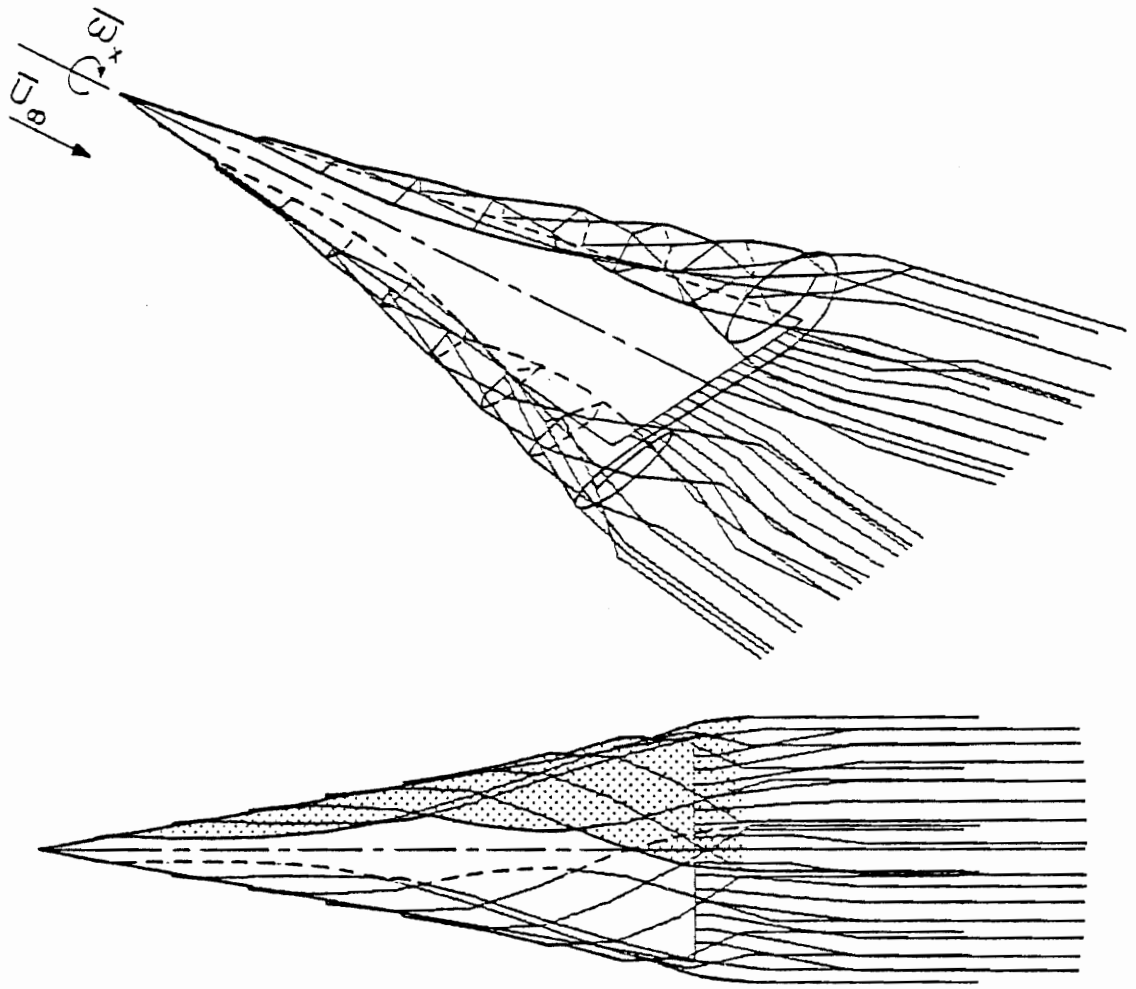

Figure 23. Wake shape of a steadily rolling delta wing, $\omega_x = -0.6$ $\alpha = 0$, 8 x 8 bound lattice, AR = 0.7.

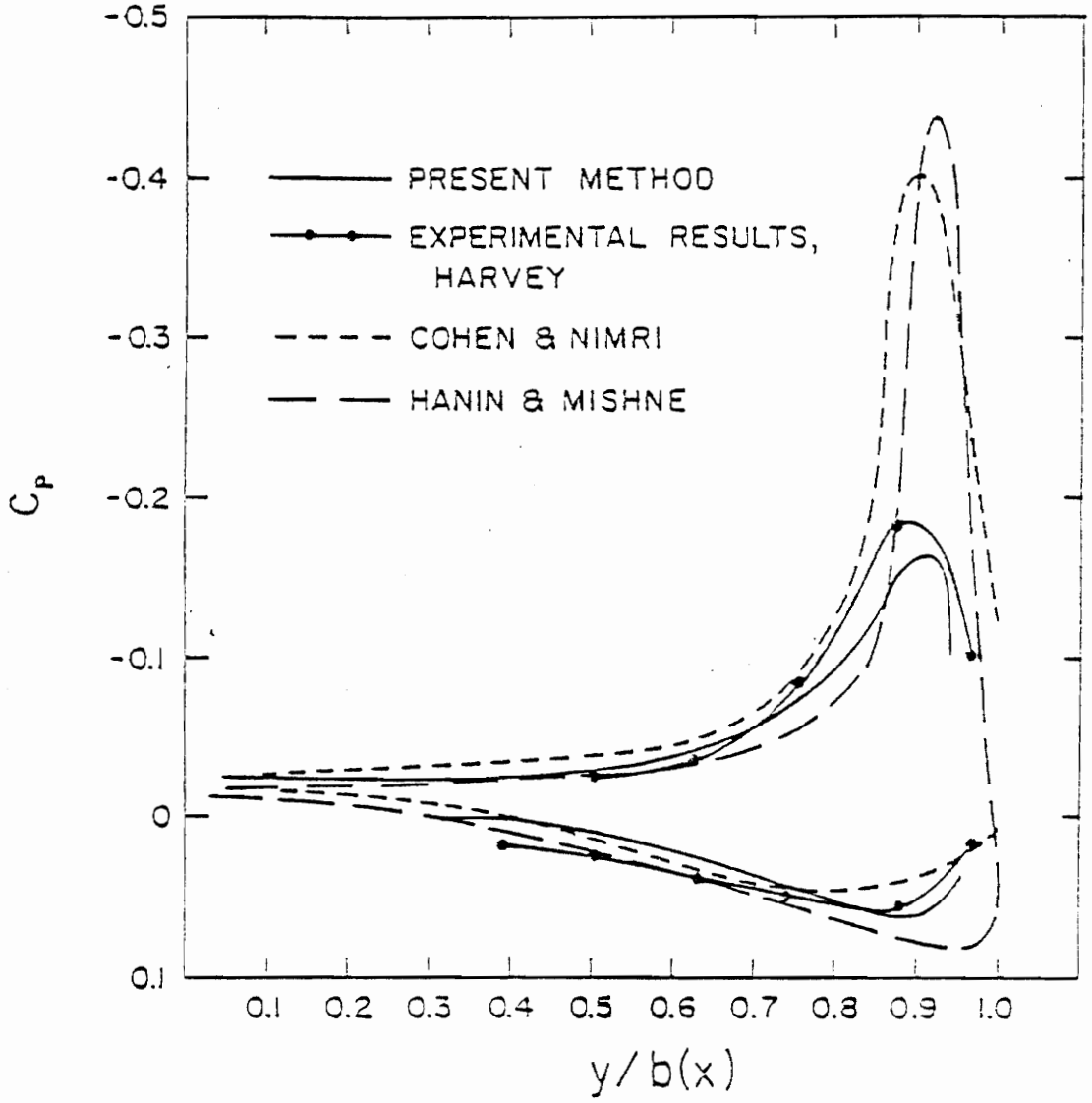

Figure 24. Upper and lower, spanwise pressure distribution on a steadily rolling delta wing, ω_x = - 0.2, α = 0, 8 x 8 bound lattice. AR = 0.7, x/c_r = 0.778.

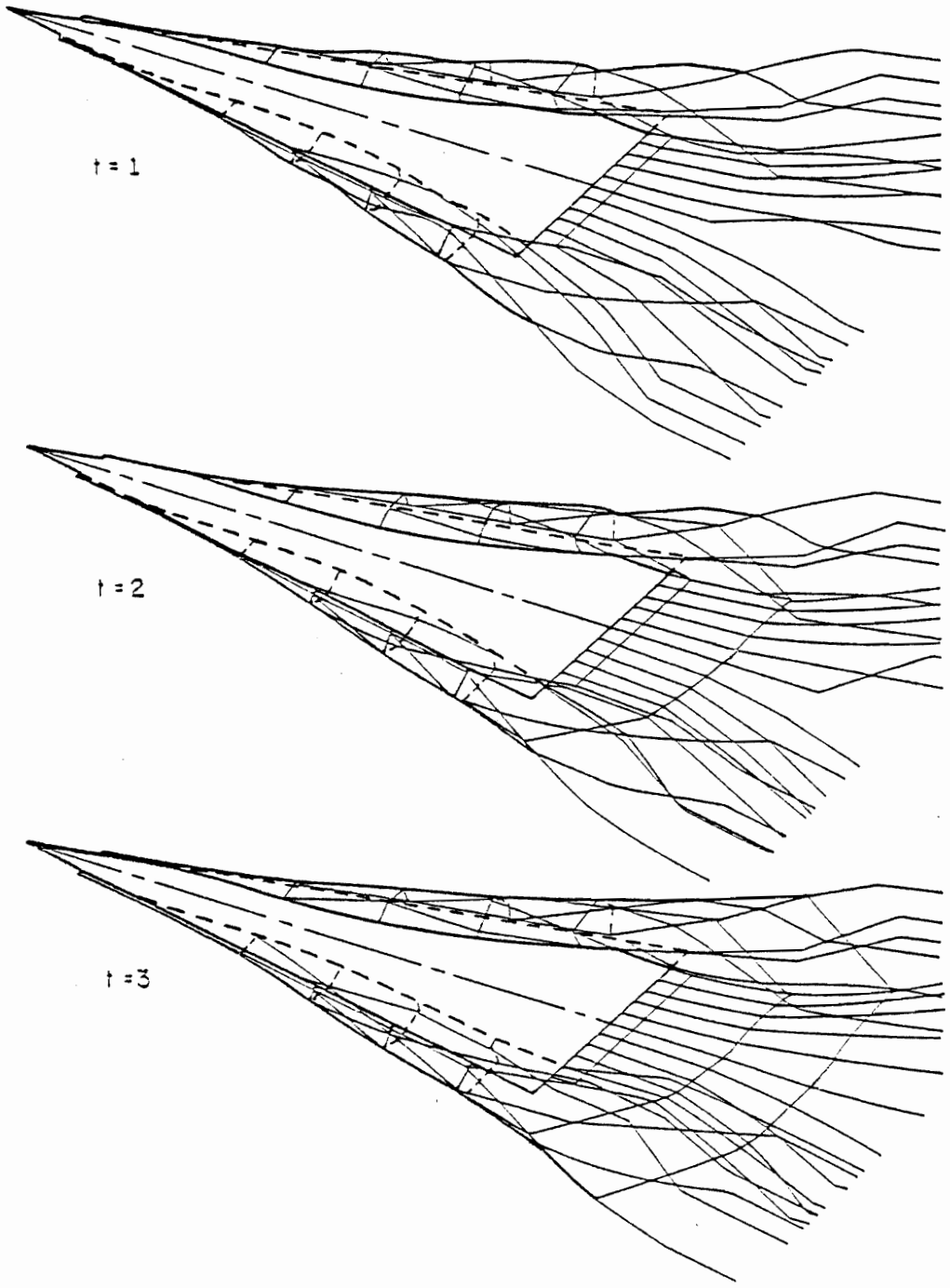

Figure 25. Wake shape of an unsteadily rolling delta wing, ω_x = -0.6 - 0.1 sin(πt/6),α = 0°, 6 x 6 bound lattice, AR = 0.7.

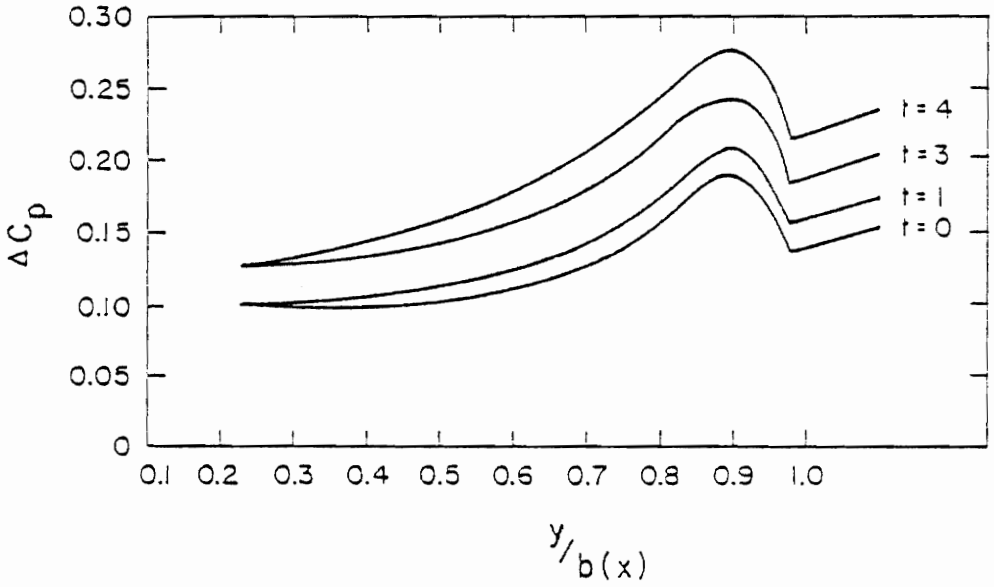

Figure 26. Variation of the net spanwise pressure distribution with time on an unsteadily rolling delta wing, $\omega_x = -0.4 - 0.1 \sin(\pi t)$, $\alpha = 0°$, 6 x 6 bound lattice, AR = 0.7, x/c_r = 0.65.

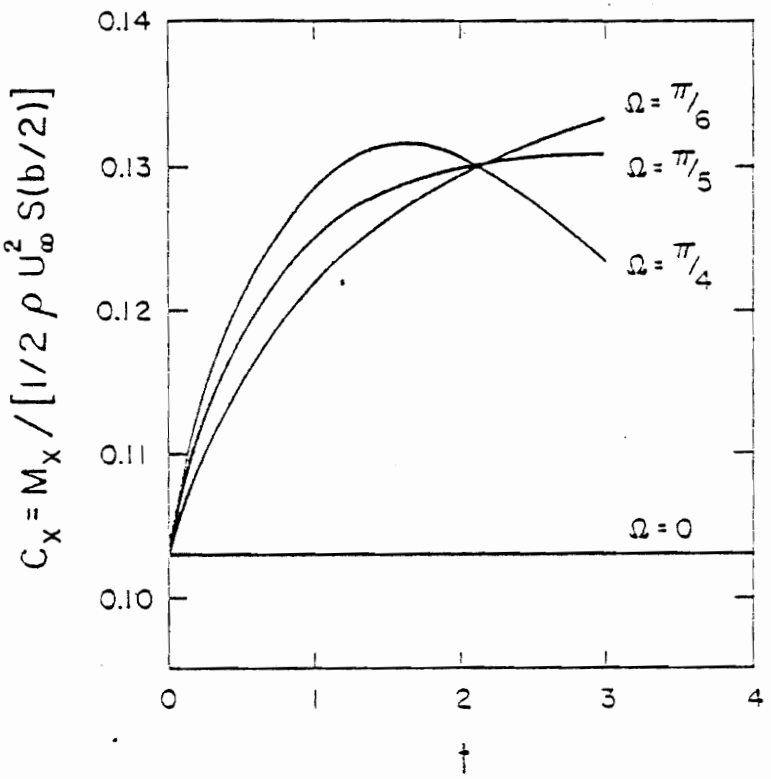

Figure 27. Variation of the rolling-moment coefficient with the frequency of rolling velocity of an unsteady rolling delta wing, $\omega_x = -0.4 - 0.1 \sin\Omega t$, $\alpha = 0°$, 6 x 6 bound lattice, AR = 0.7.

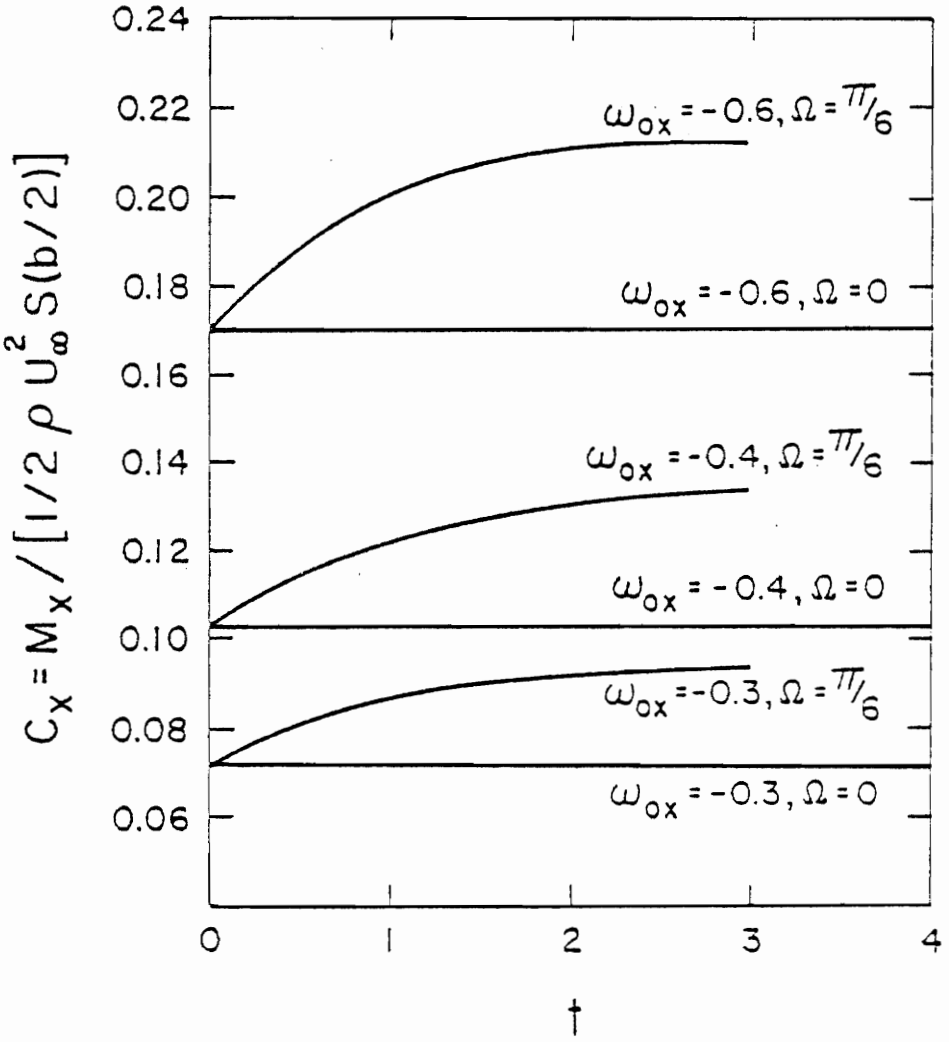

Figure 28. Variation of the rolling-moment coefficient with the mean rate of roll of an unsteadily rolling delta wing, $\omega_x = \omega_{ox} - 0.1 \sin t$, $\alpha = 0°$, 6 x 6 bound lattice, AR = 0.7.

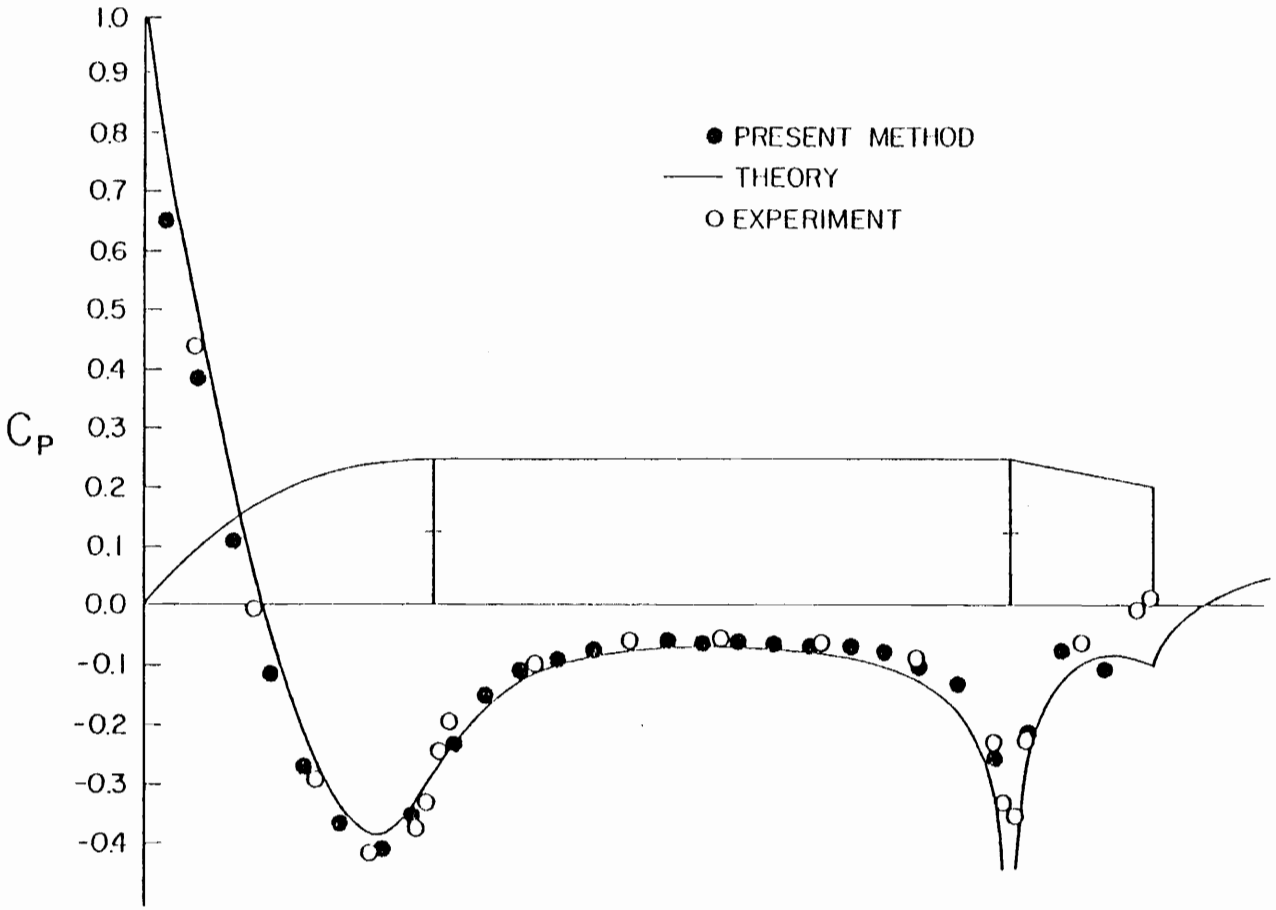

Figure 29. Pressure distribution on a tangent-ogive, $\alpha = 0$, $M = 0.4$, $\lambda = 3.5$, 488 elements, comparison with Woodward (Theory) and Fox (experiments).

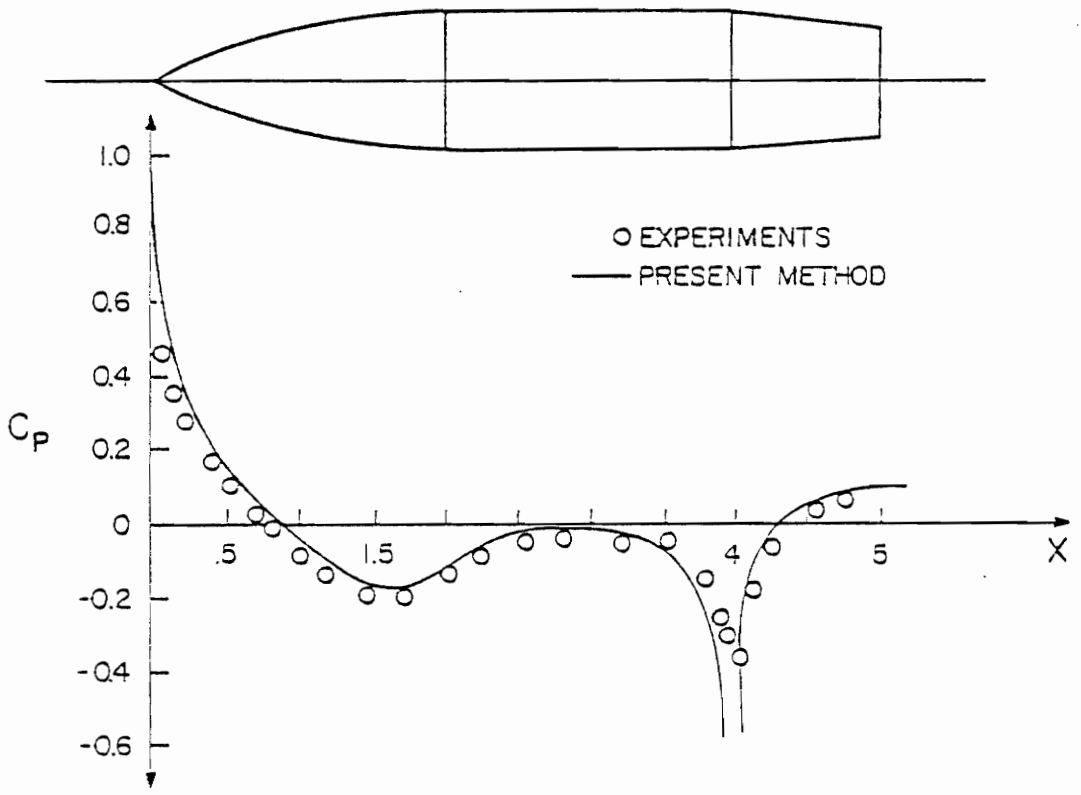

Figure 30. Pressure distribution on a tangent-ogive, α = 0, M = 0.37 λ = 5, 376 elements, comparison with Fox (experiments).

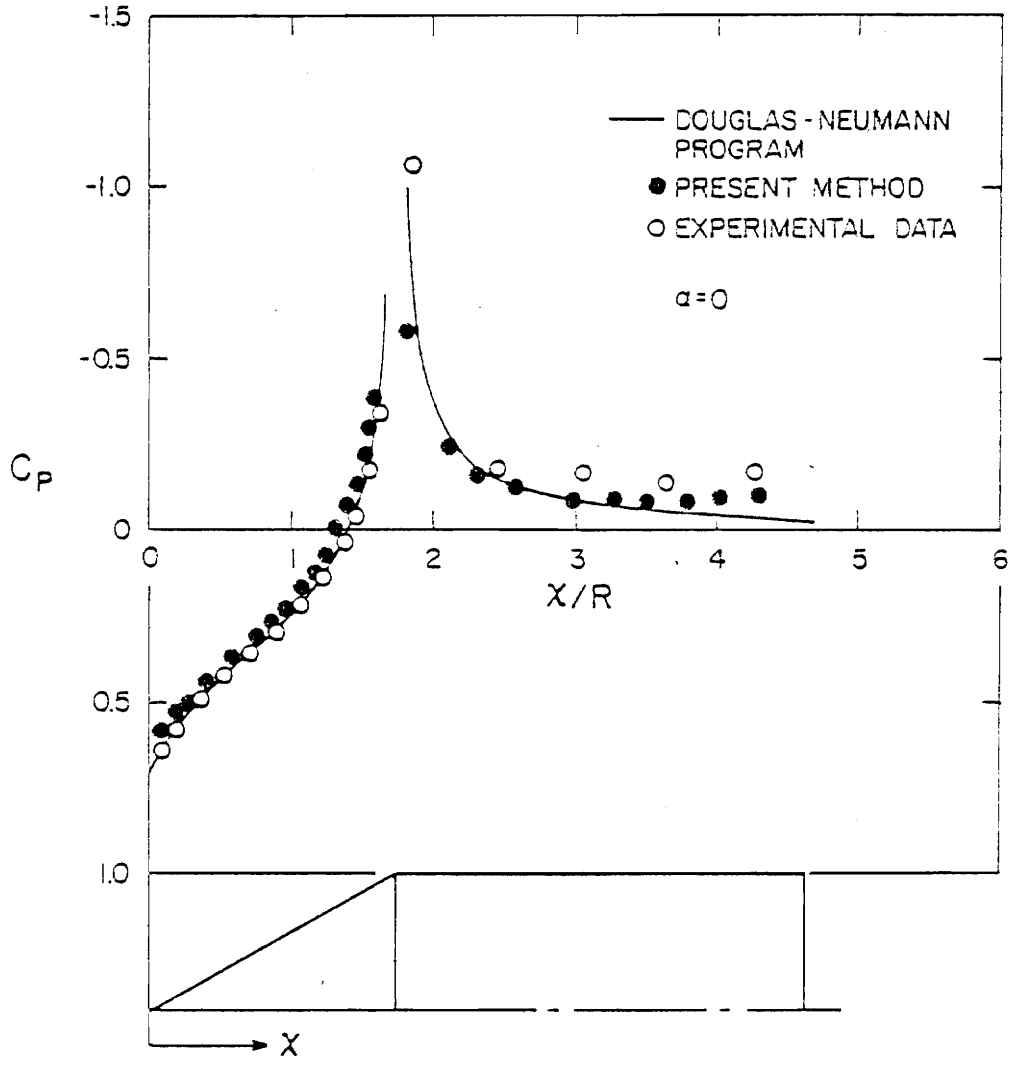

Figure 31. Pressure distribution for a cone-cylinder, α = 0, λ = 2.25.

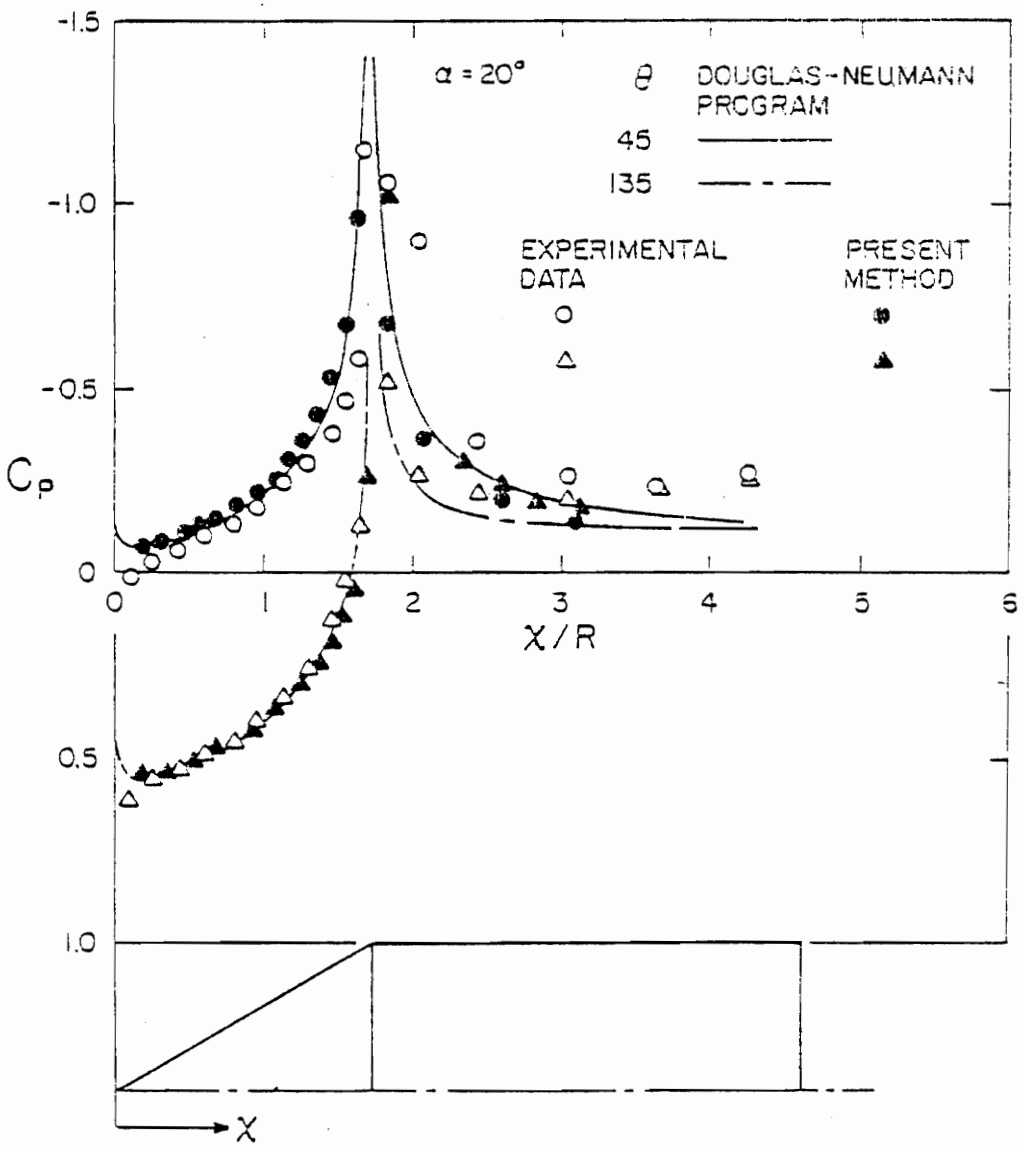

Figure 32. Pressure distribution for a cone-cylinder at an angle of attack.

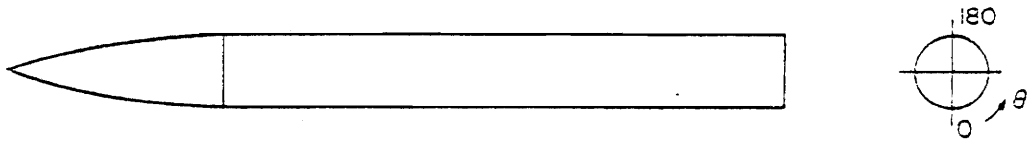

M = 0.3
Re = 0.44 X 10^6
α = 10°
λ = 10.78

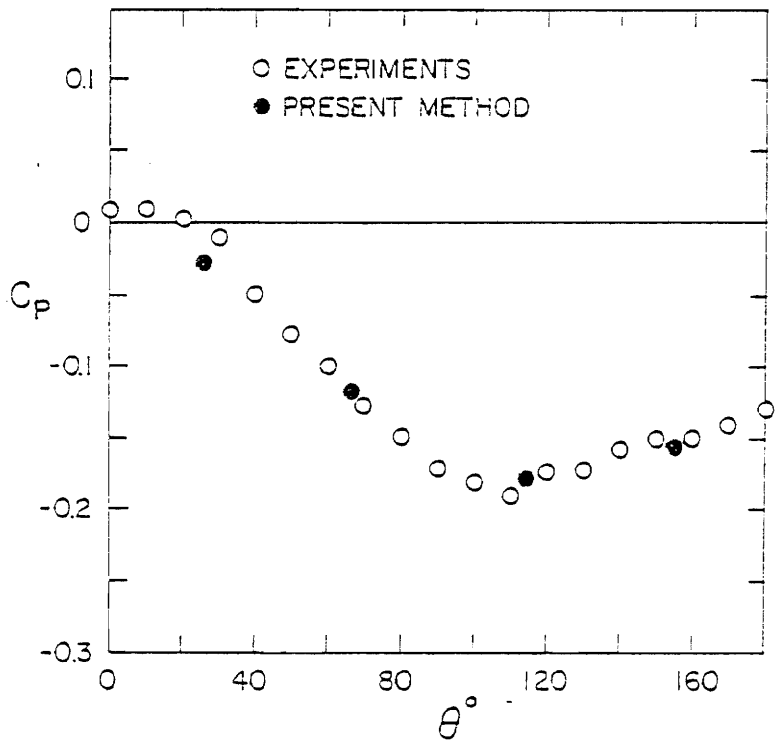

Figure 33.a. Pressure distribution for a tangent-ogive, $\frac{x}{d}$ = 2.

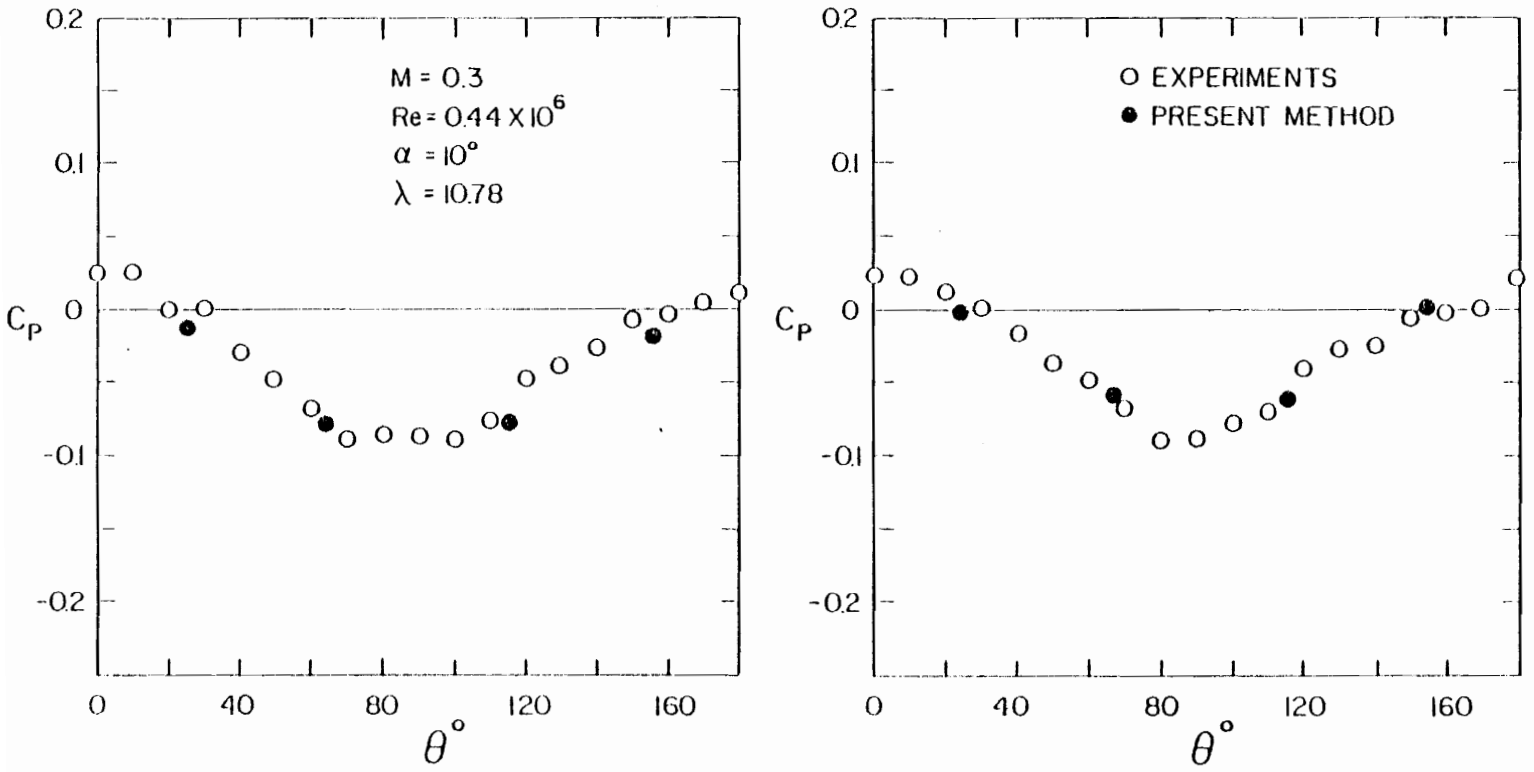

Figure 33.b. Pressure distribution for a tangent-ogive, $\frac{x}{d}$ = 4.5,6

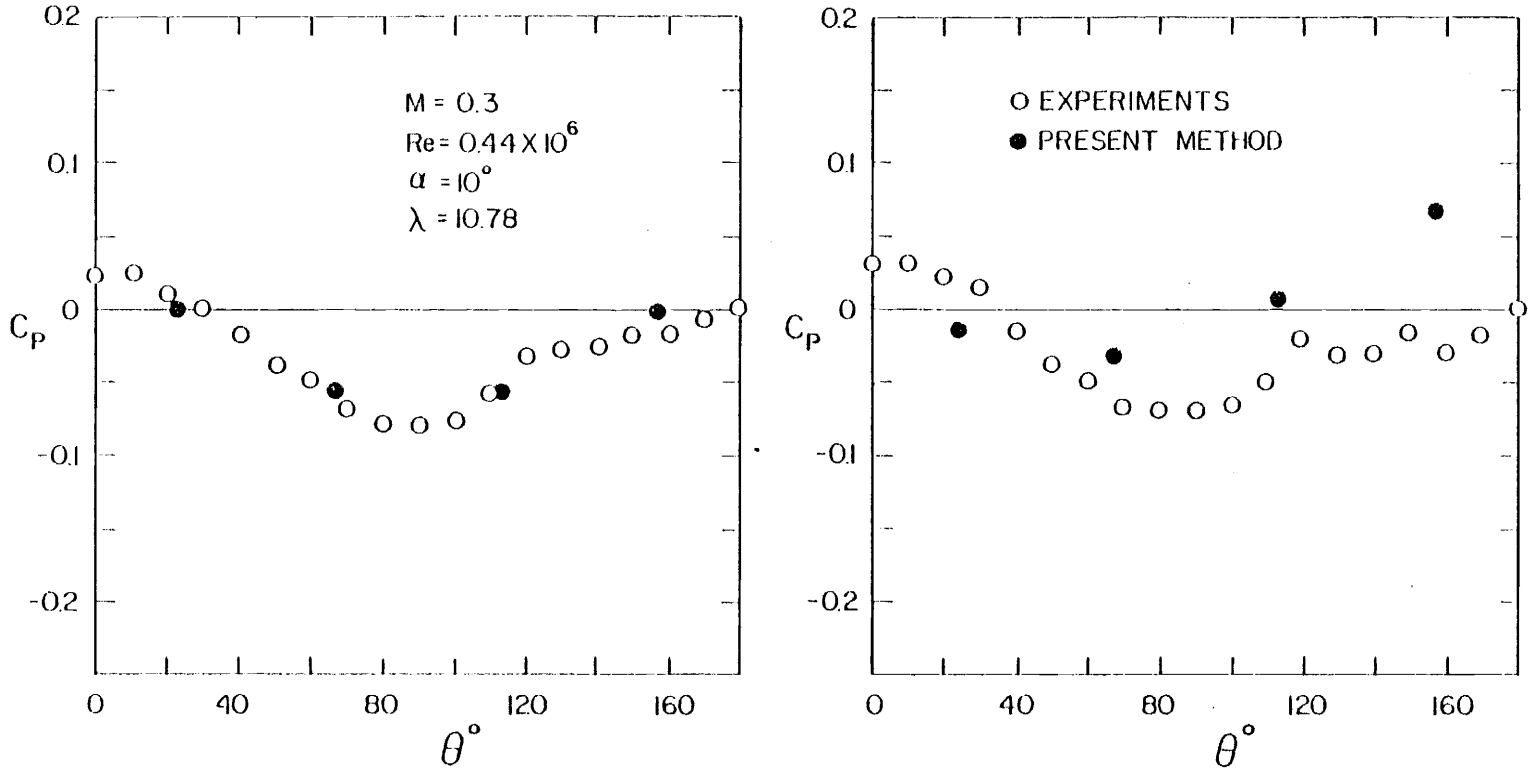

Figure 33.c. Pressure distribution for a tangent-ogive, $\frac{X}{d}$ = 7.5, 10

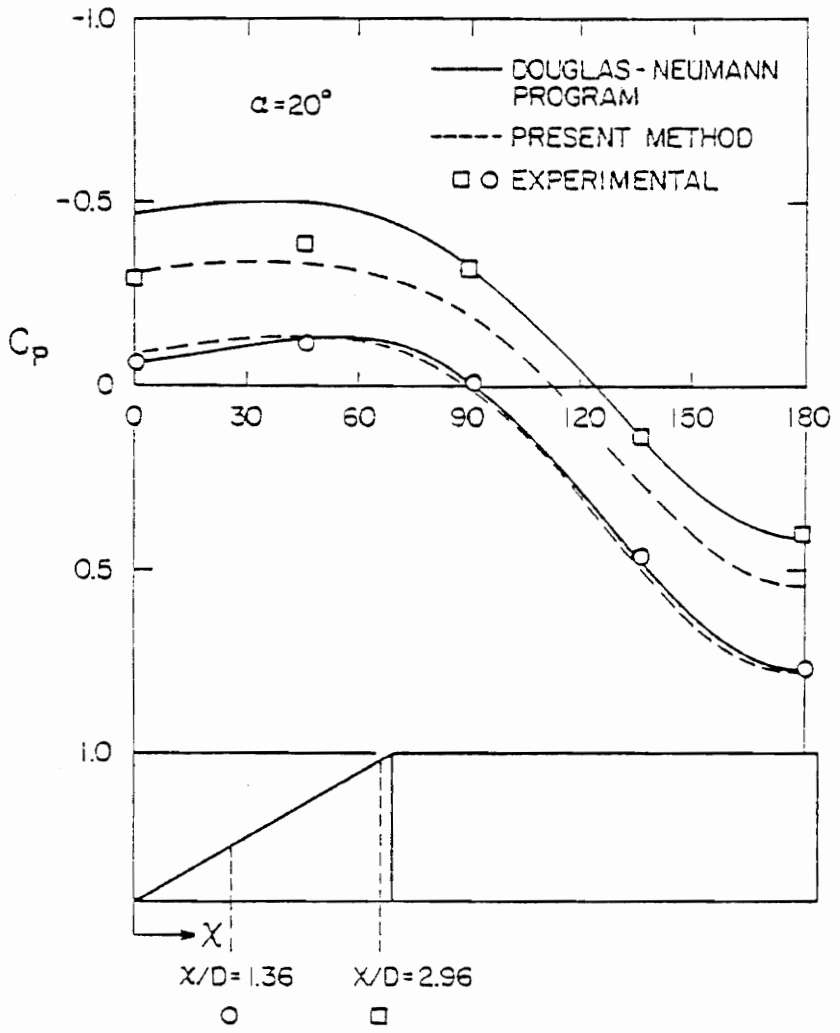

Figure 34. Pressure distribution for a cone-cylinder.

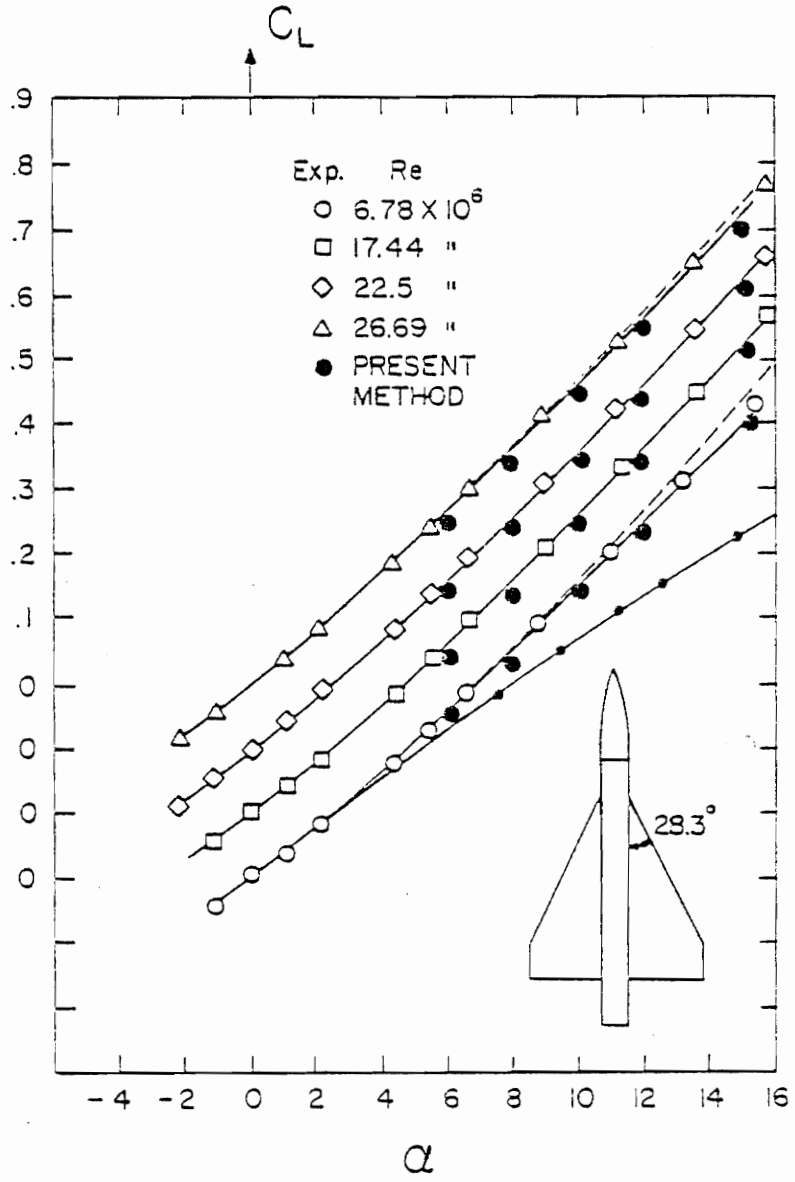

Figure 35. Lift coefficient vs. angle of attack for a wing-body combination, M = 0.3, —.—.— linear results, — — — suction analogy.

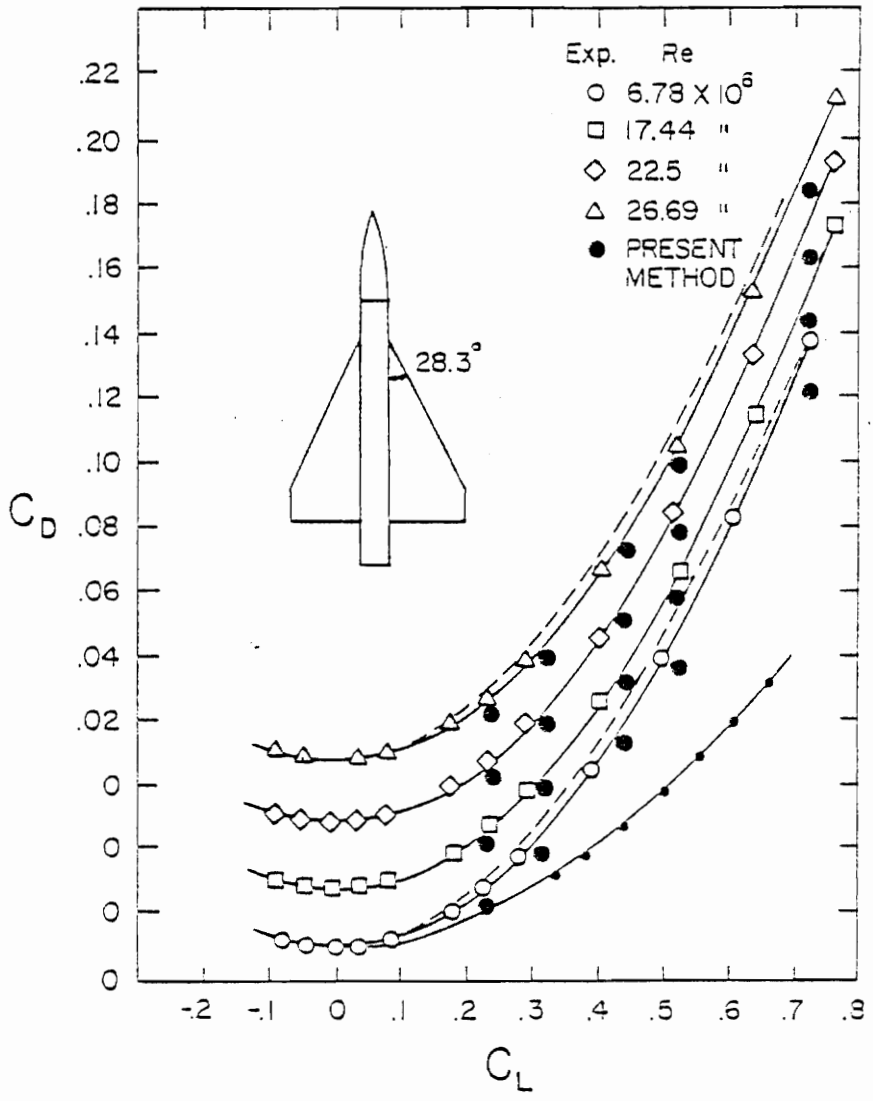

Figure 36. Induced drag coefficient vs. lift-coefficient for a wing-body combination, M = 0.3, —.—.— linear results, — — — suction analogy.

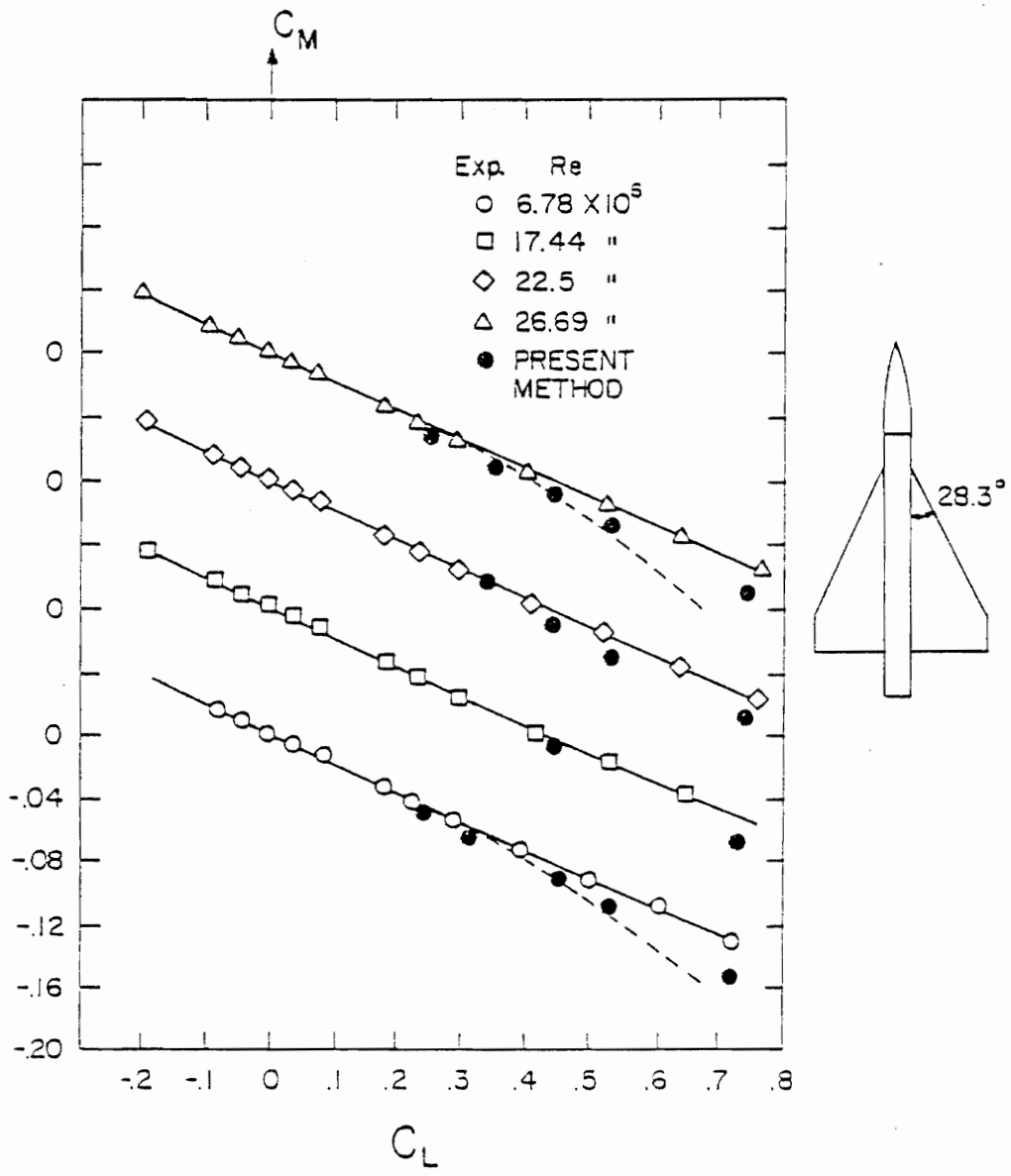

Figure 37. Pitching-moment coefficient vs. lift coefficient for a wing-body combination, — — — suction analogy.

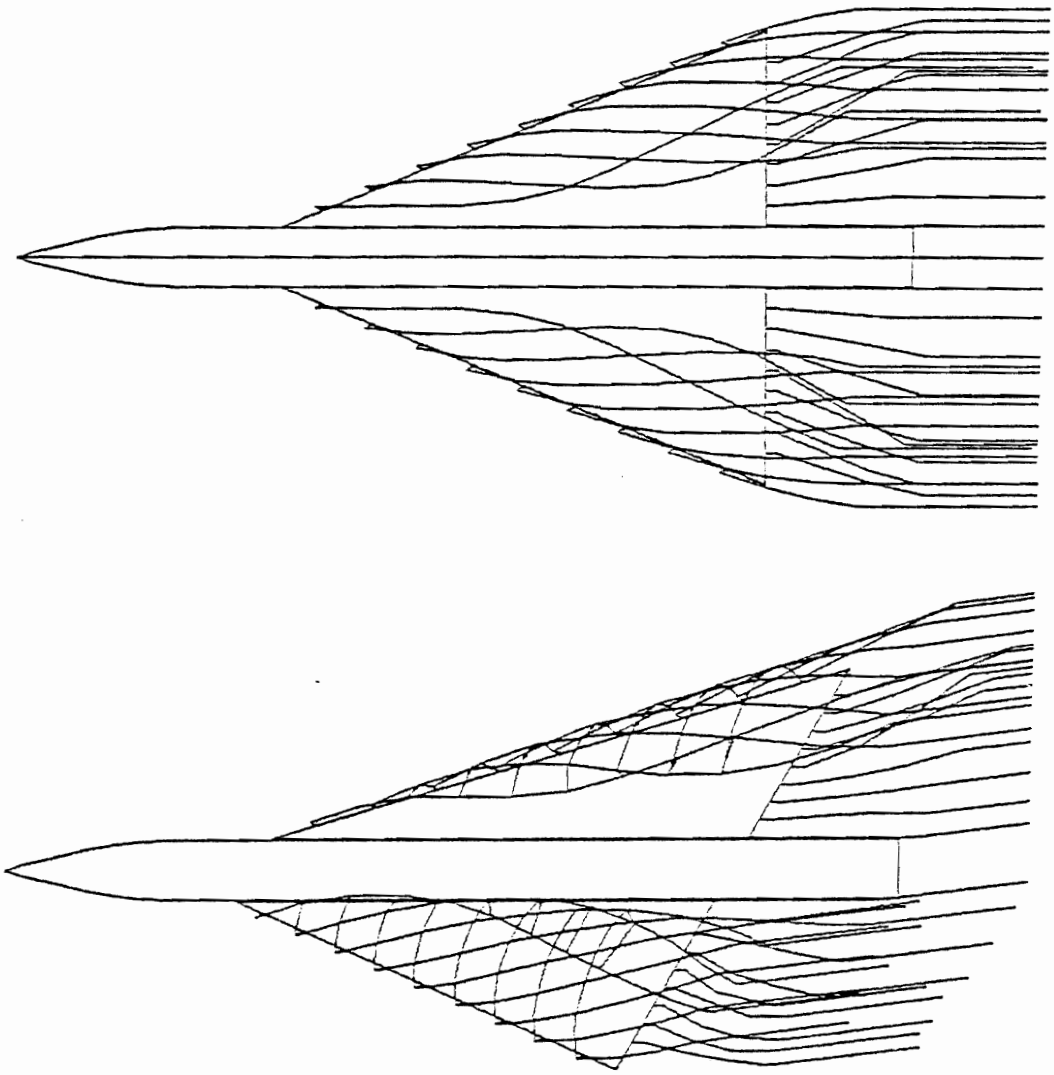

Figure 38. Wake shape for a wing-body combination, α = 12°, ε = 22.5° λ = 13.83.

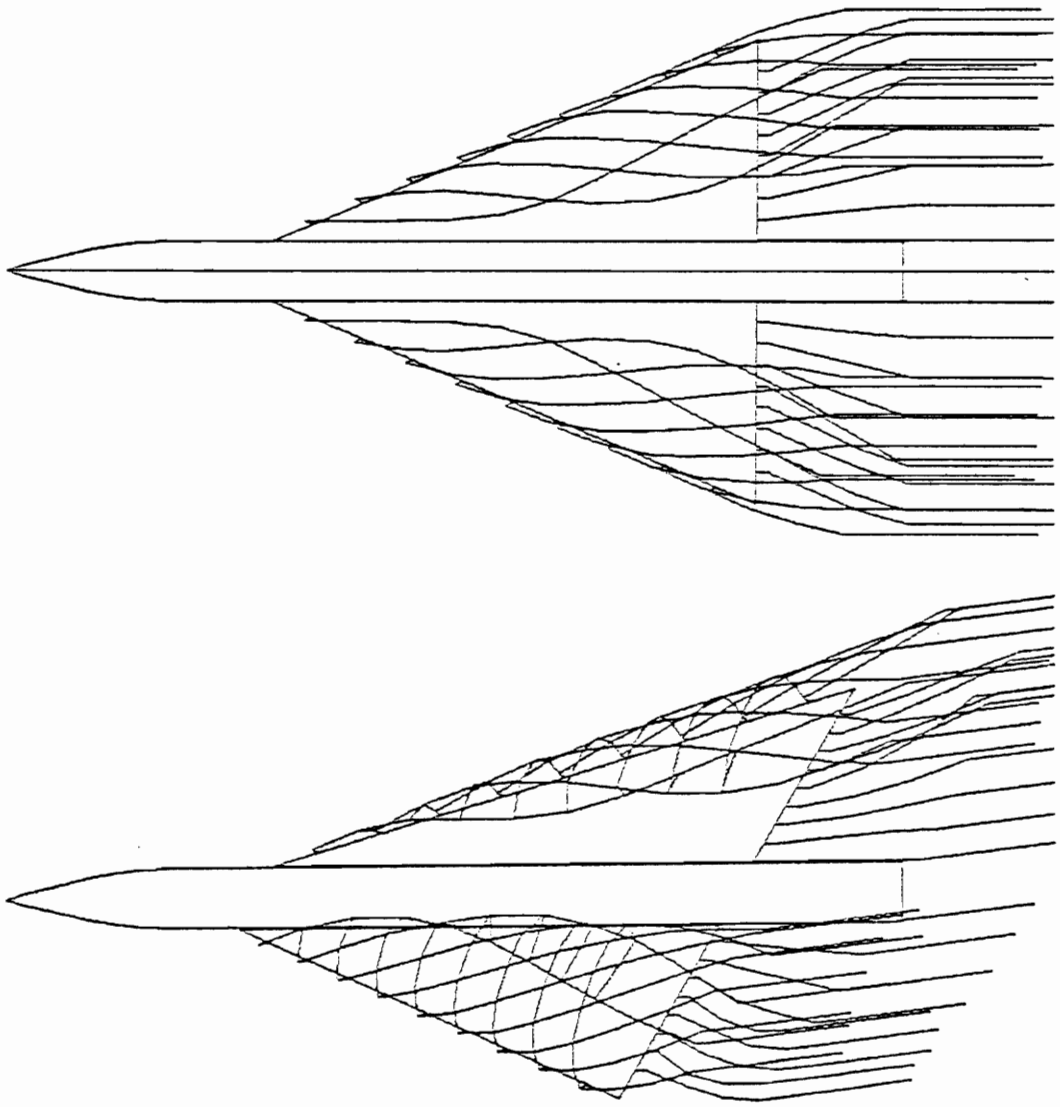

Figure 39. Wake shape for a wing-body combination, α = 15°, ε = 22.5 λ = 13.83.

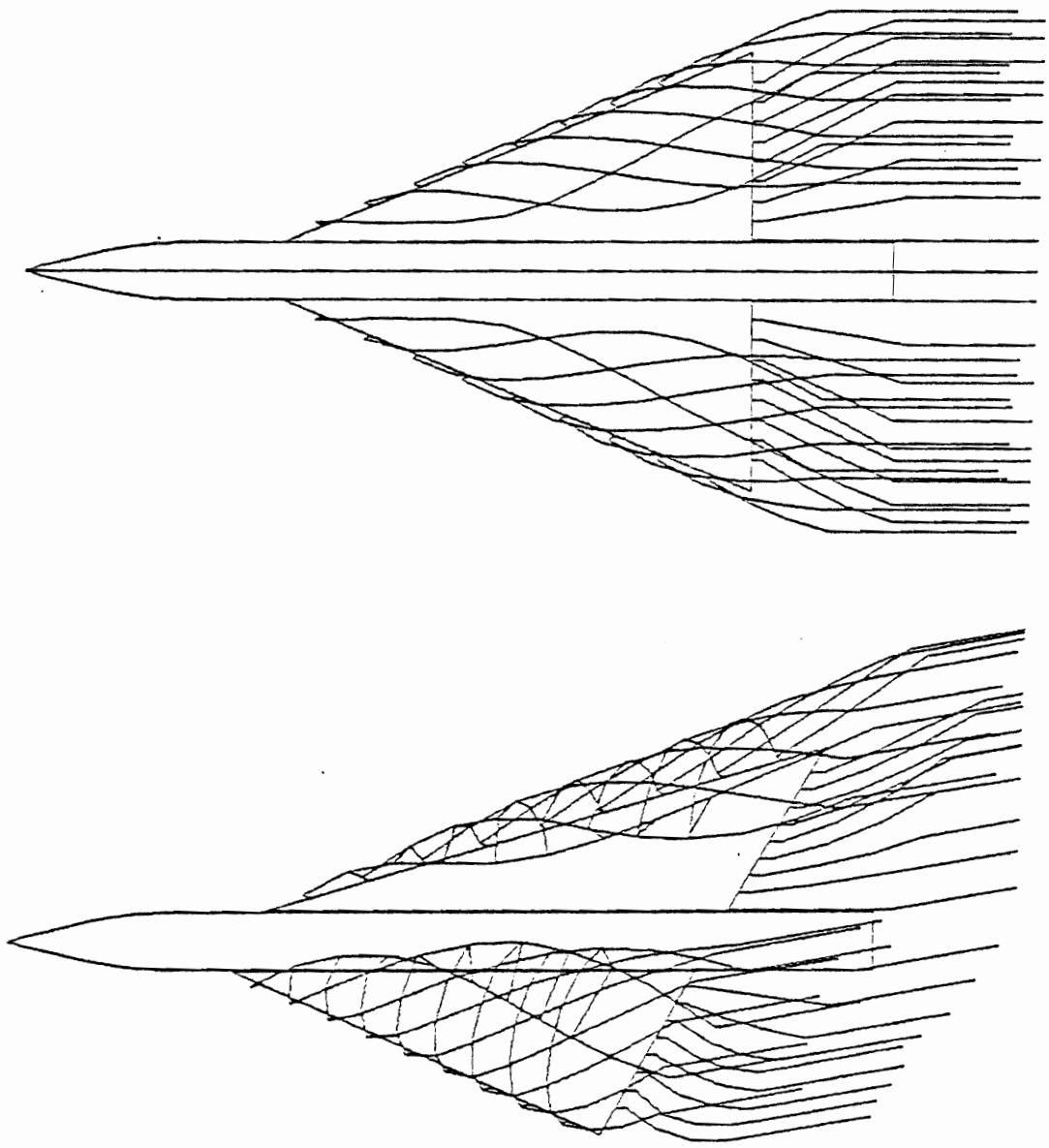

Figure 40. Wake shape for a wing-body combination, $\alpha = 20°$, $\varepsilon = 22.5°$ $\lambda = 13.83$.

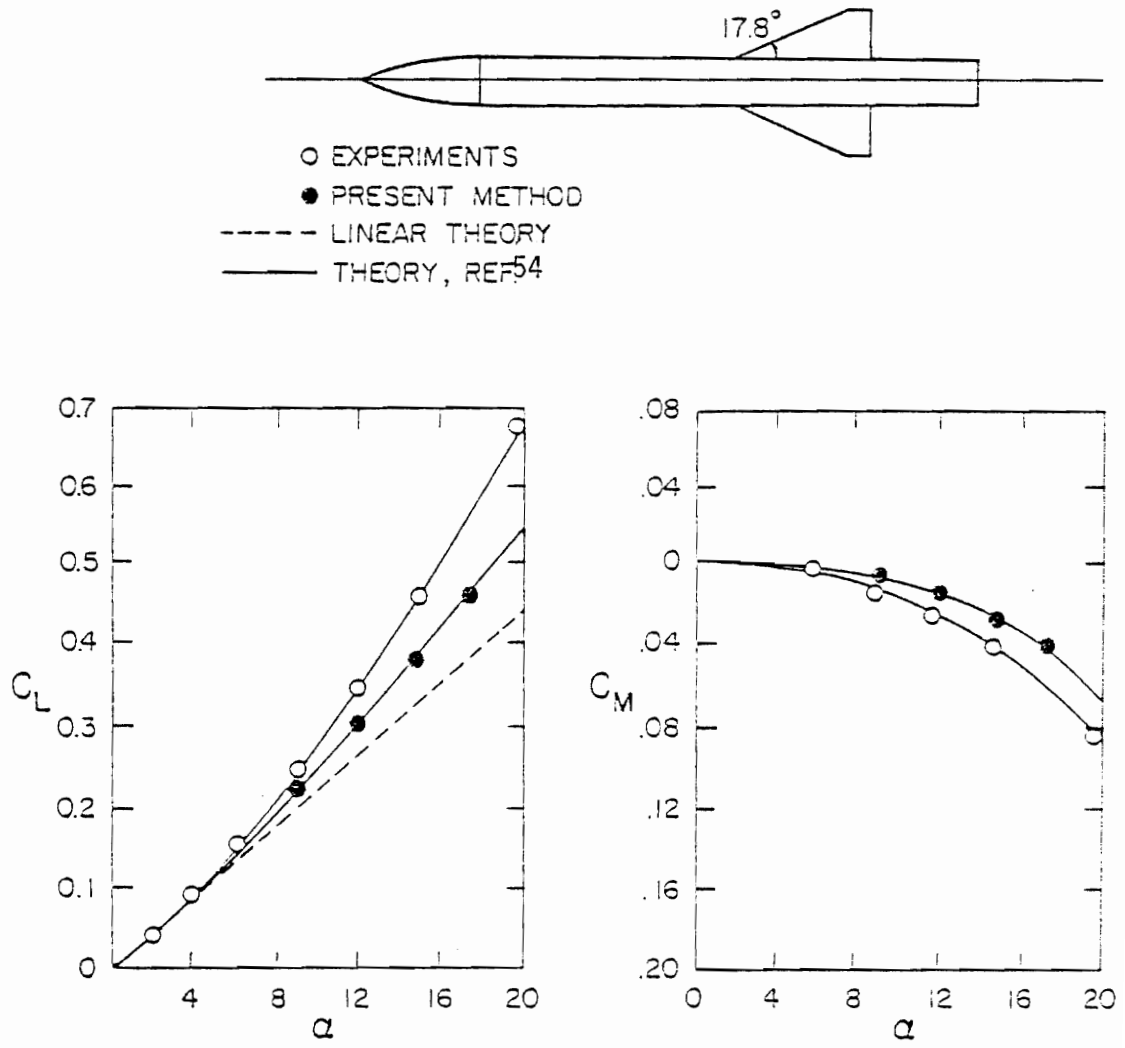

Figure 41. Lift and pitching-moment coefficients for a wing-body combination vs. angle of attack, $\lambda = 10$, comparison with Otto (theory and experiment).

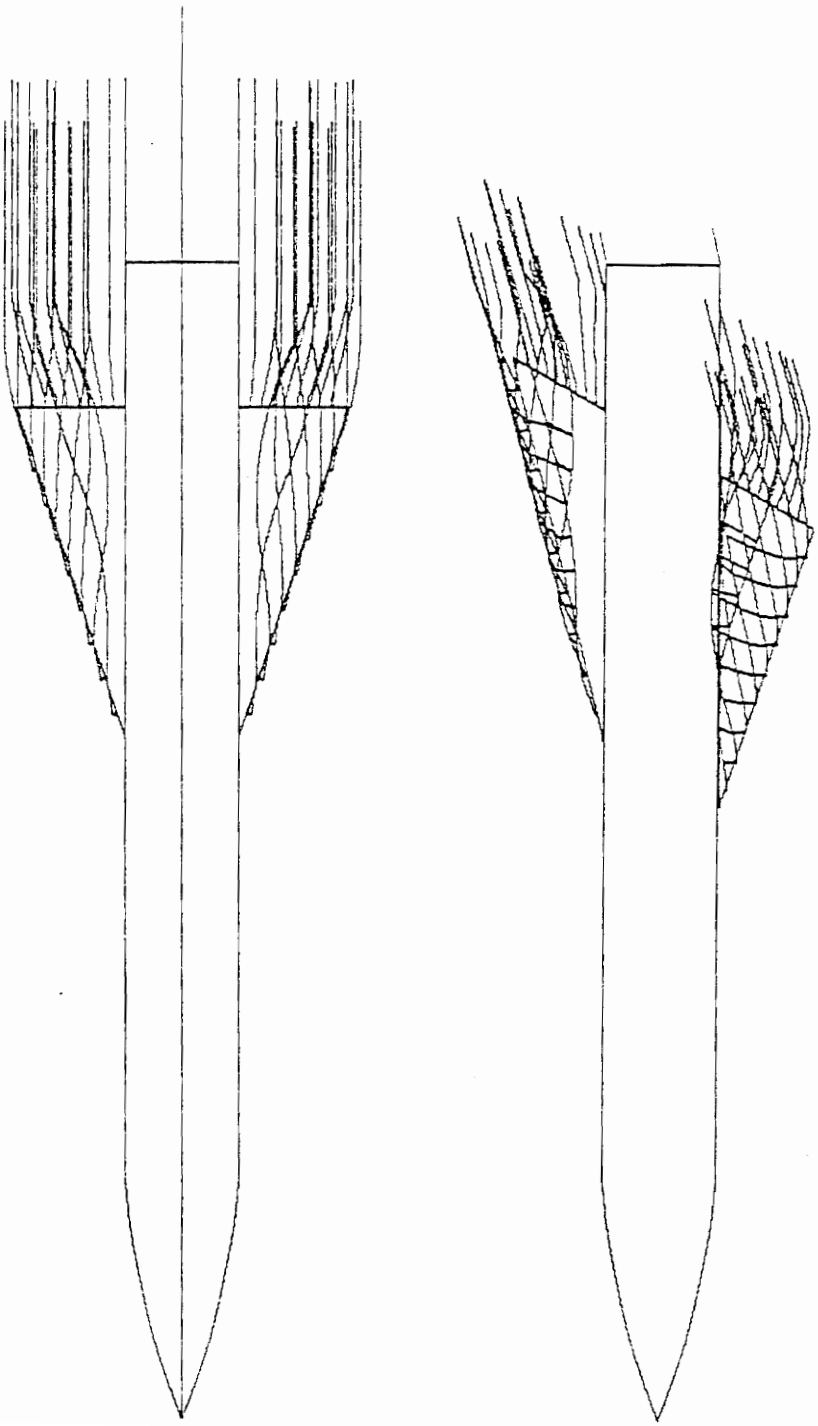

Figure 42. Wake shape for a wing-body combination, $\alpha = 9°$, $\lambda = 10$.

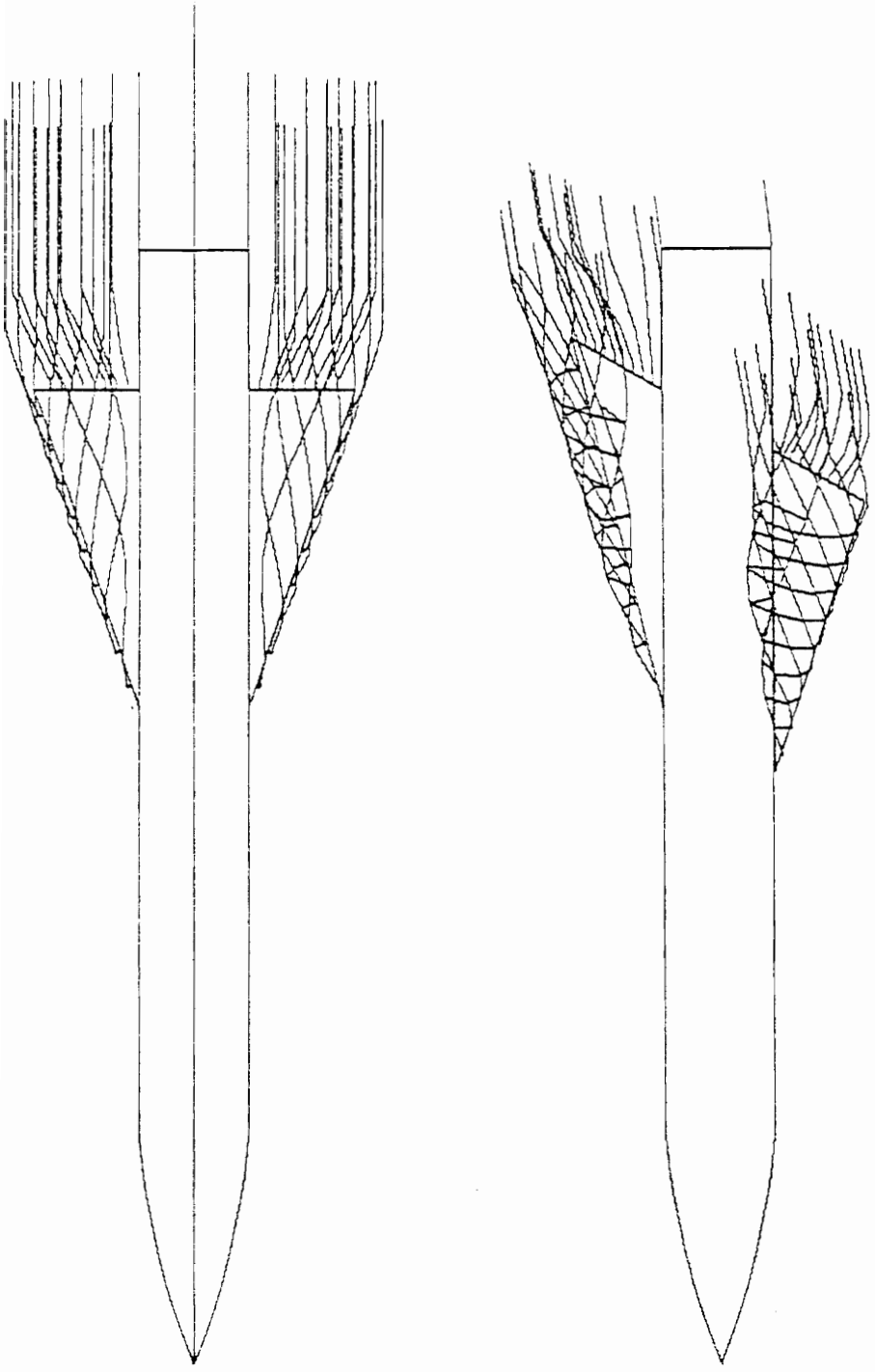

Figure 43. Wake shape for a wing-body combination, $\alpha = 17°$, $\lambda = 10$.

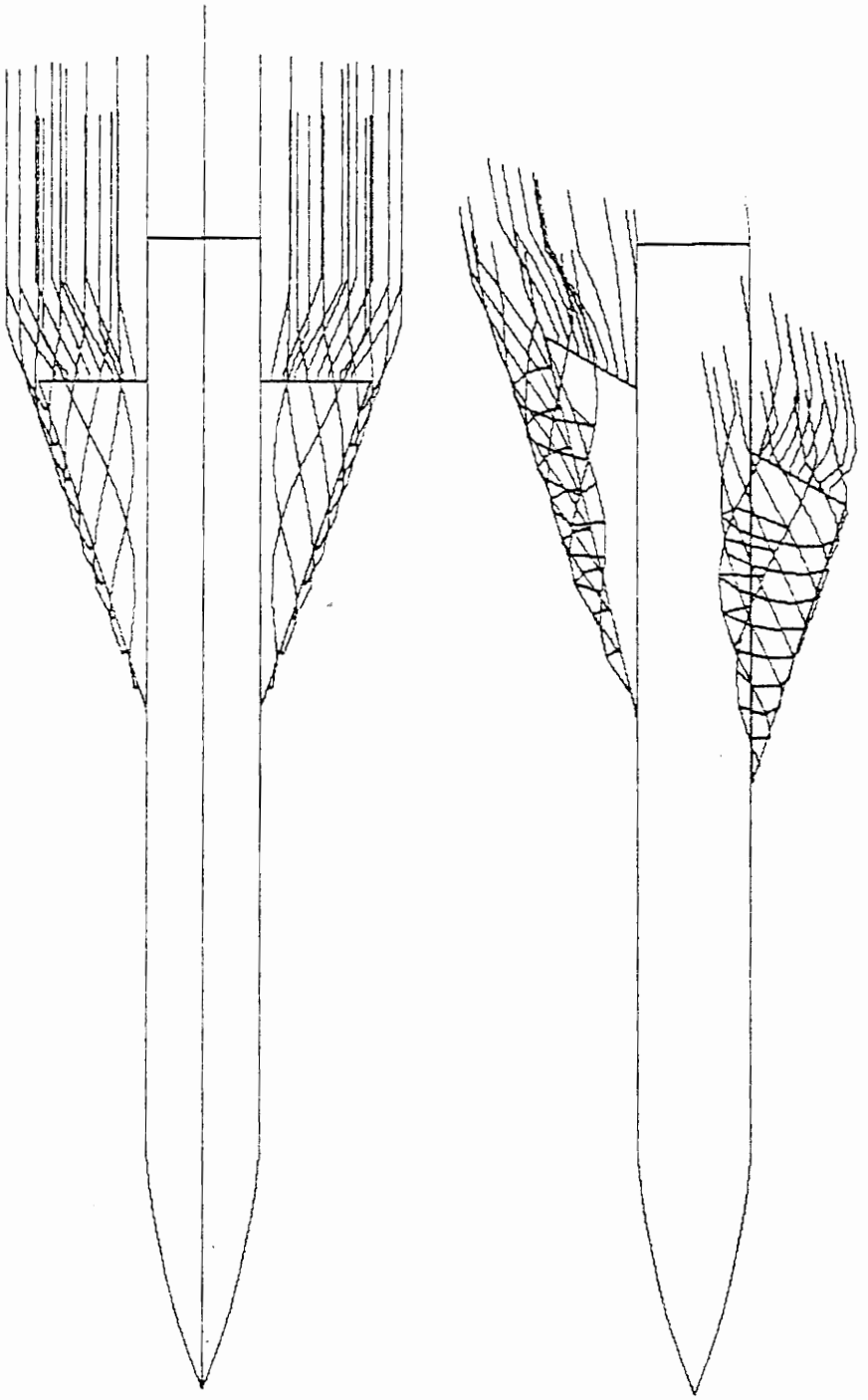

Figure 44. Wake shape for a wing-body combination, $\alpha = 20°$, $\lambda = 10$.

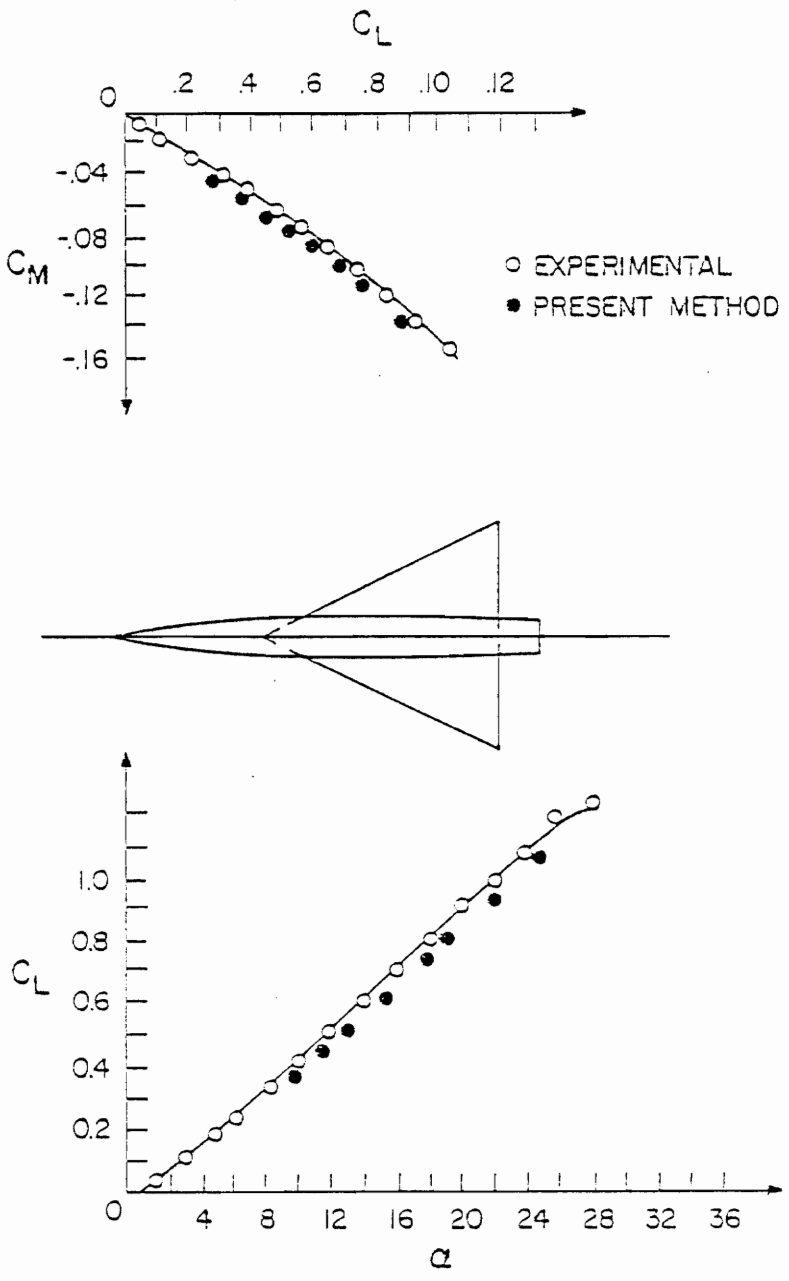

Figure 45. Lift and pitching-moment coefficients vs. angle of attack for a wing-body combination, AR = 2, λ = 9.86.

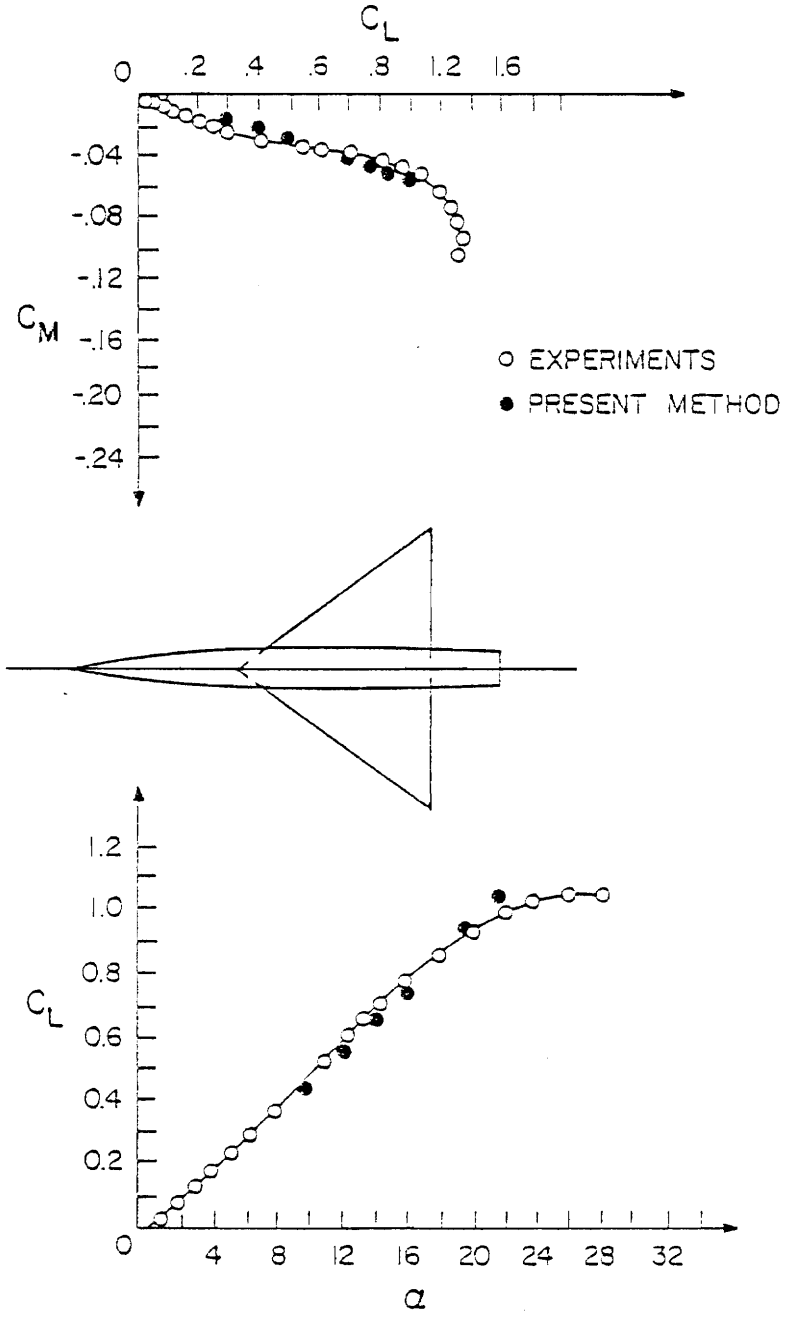

Figure 46. Lift and pitching-moment coefficients vs. angle of attack for a wing-body combination, AR = 3, λ = 9.86.

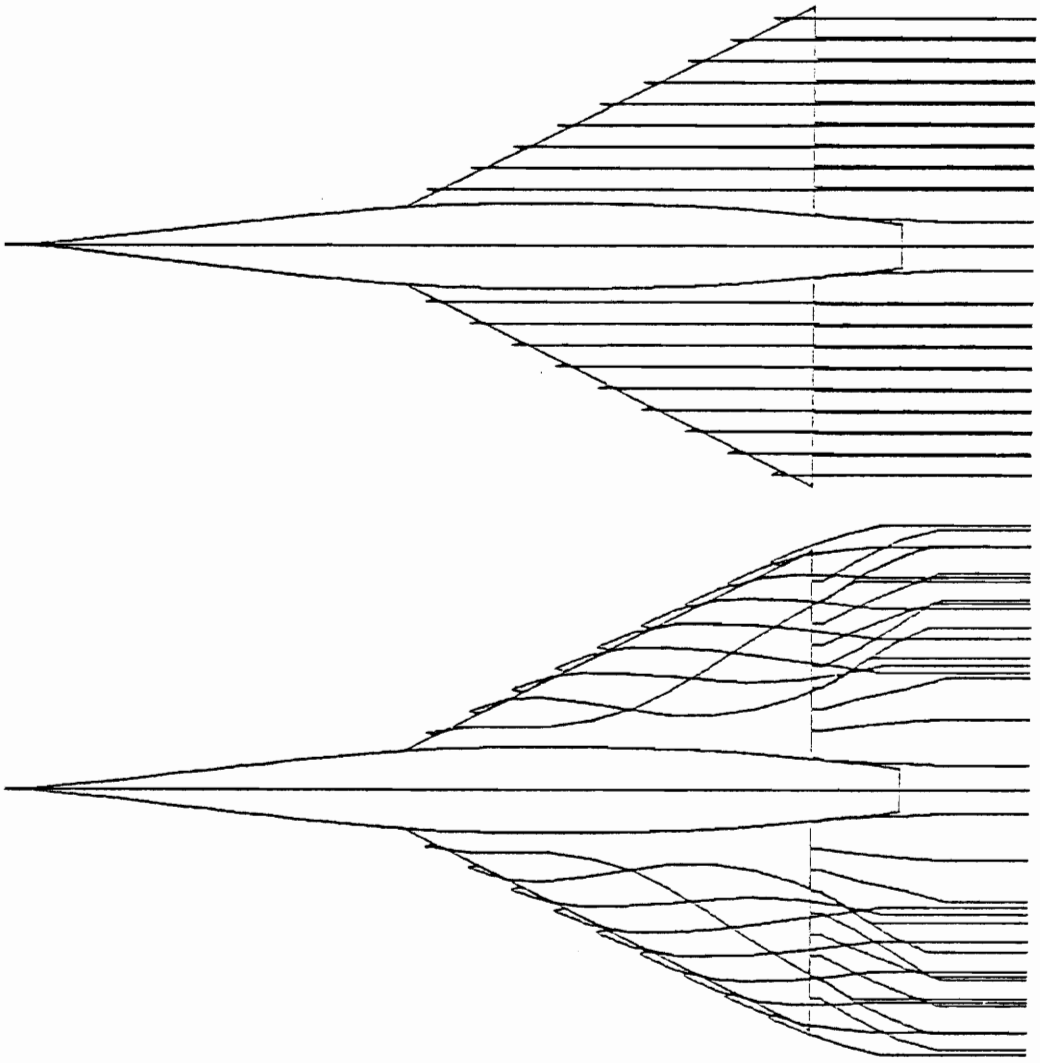

Figure 47. Wake shape for a wing-body combination initial guess vs. converged shape, α = 16°, AR = 2.

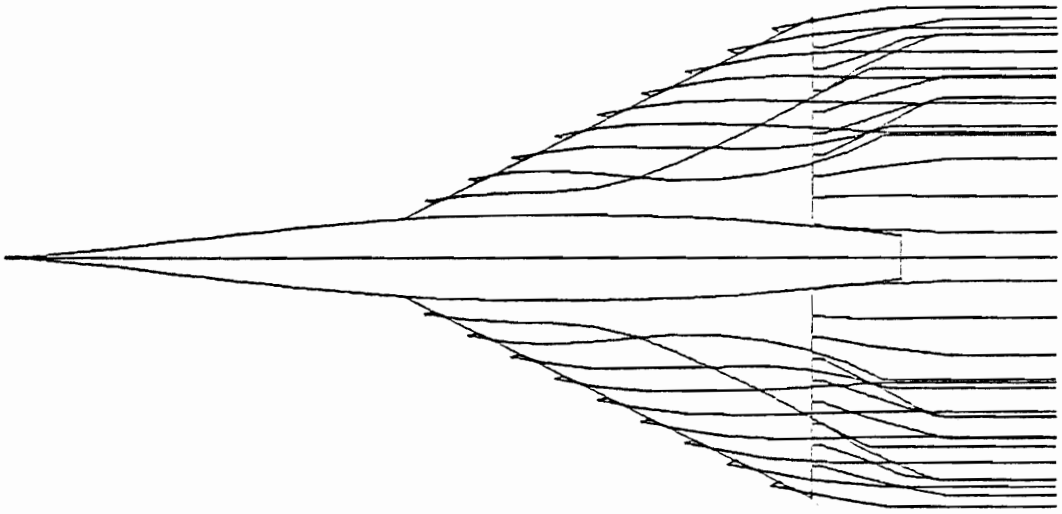

Figure 48.a. Wake shape for a wing-body combination, AR = 2, α = 12.15°.

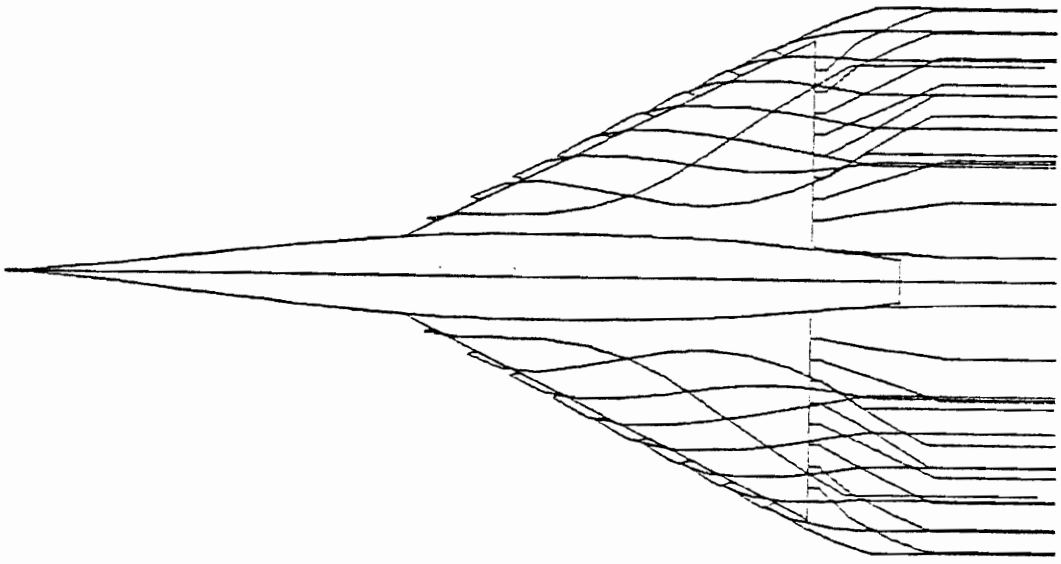

Figure 48.b. Wake shape for a wing-body combination, AR = 2, α = 20°

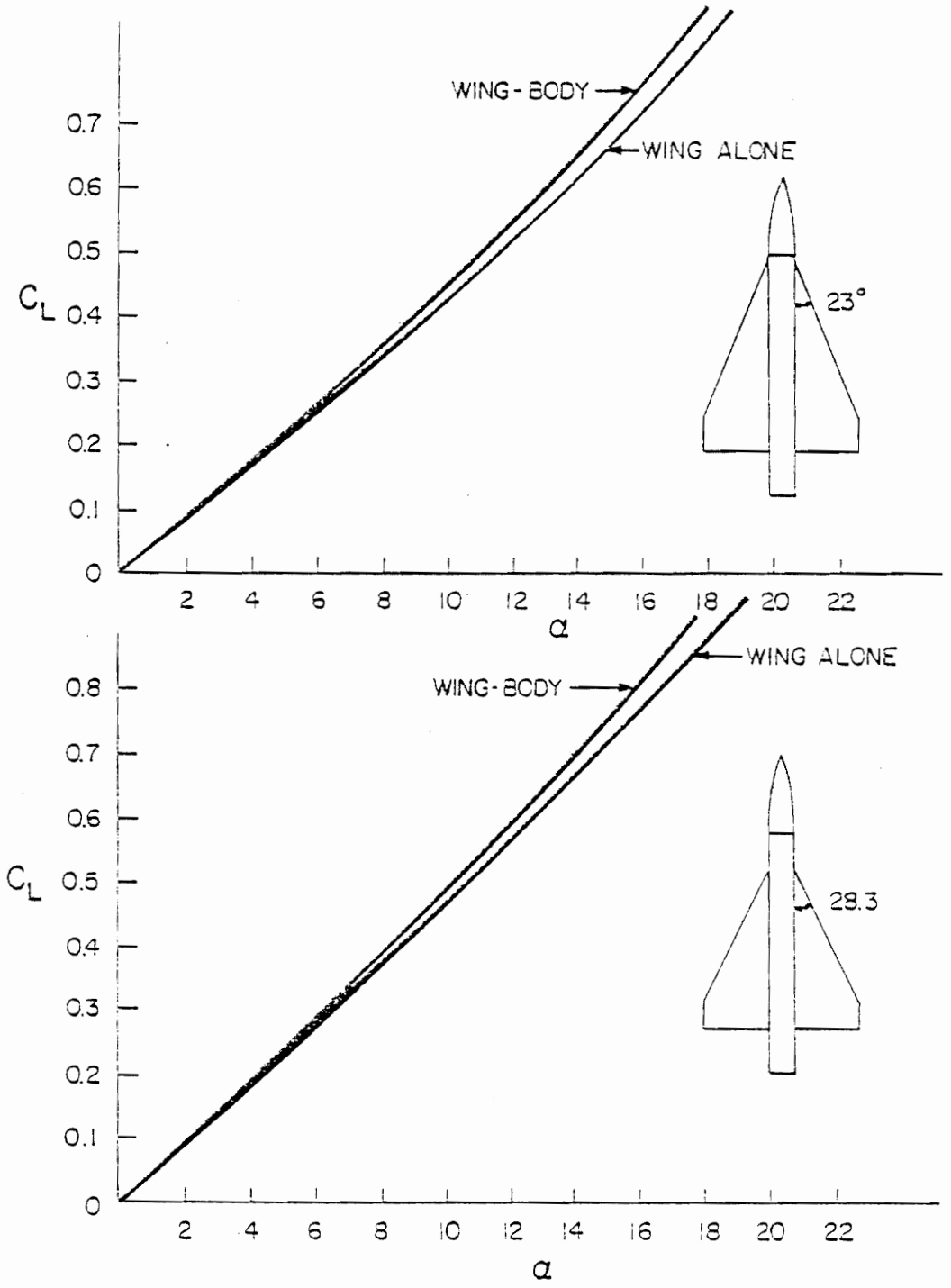

Figure 49. Effect of body on the lift and pitching-moment coefficients for two wing-body combinations, λ = 13.83.

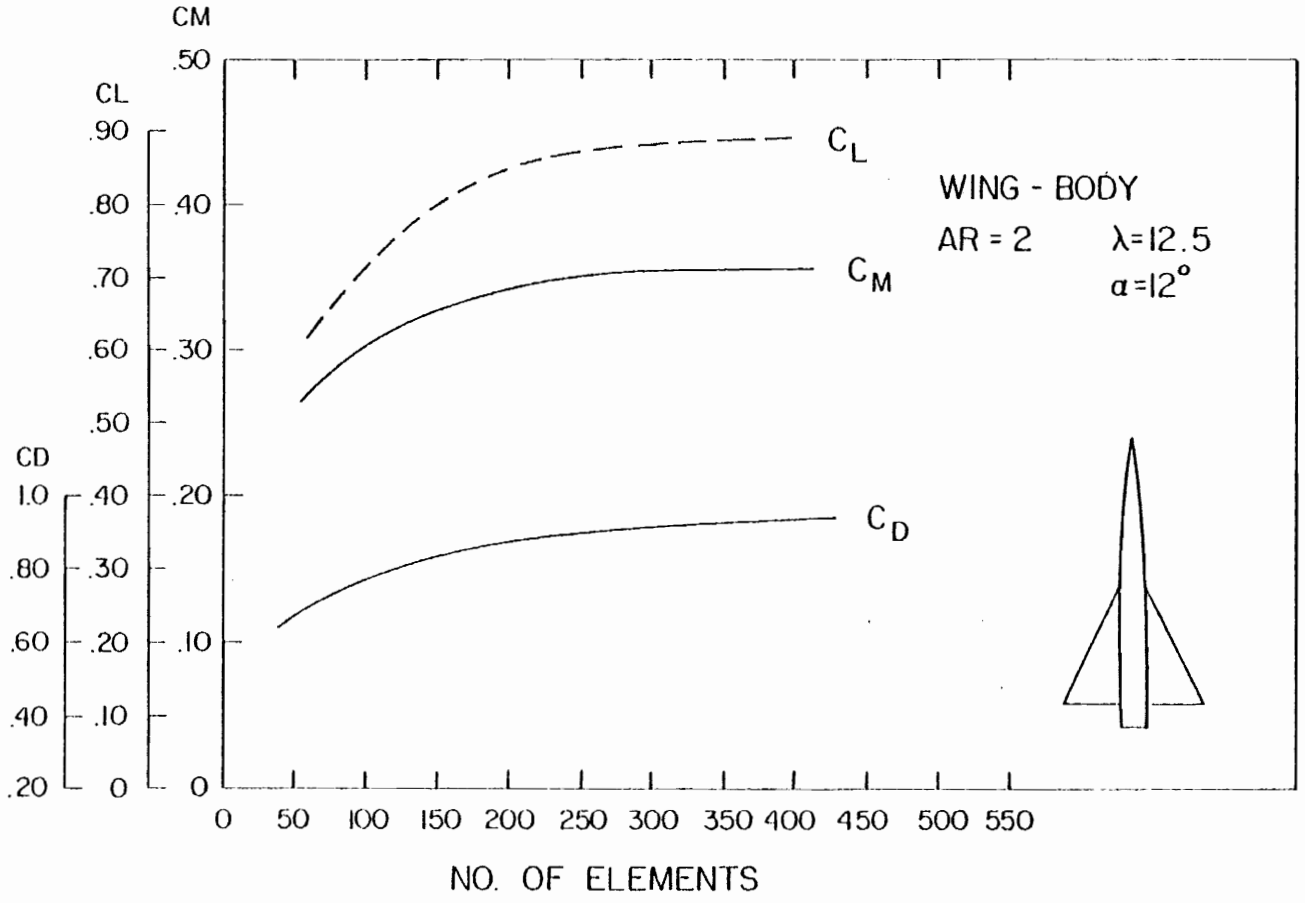

Figure 50. Convergence of the total loads for a wing-body combination.

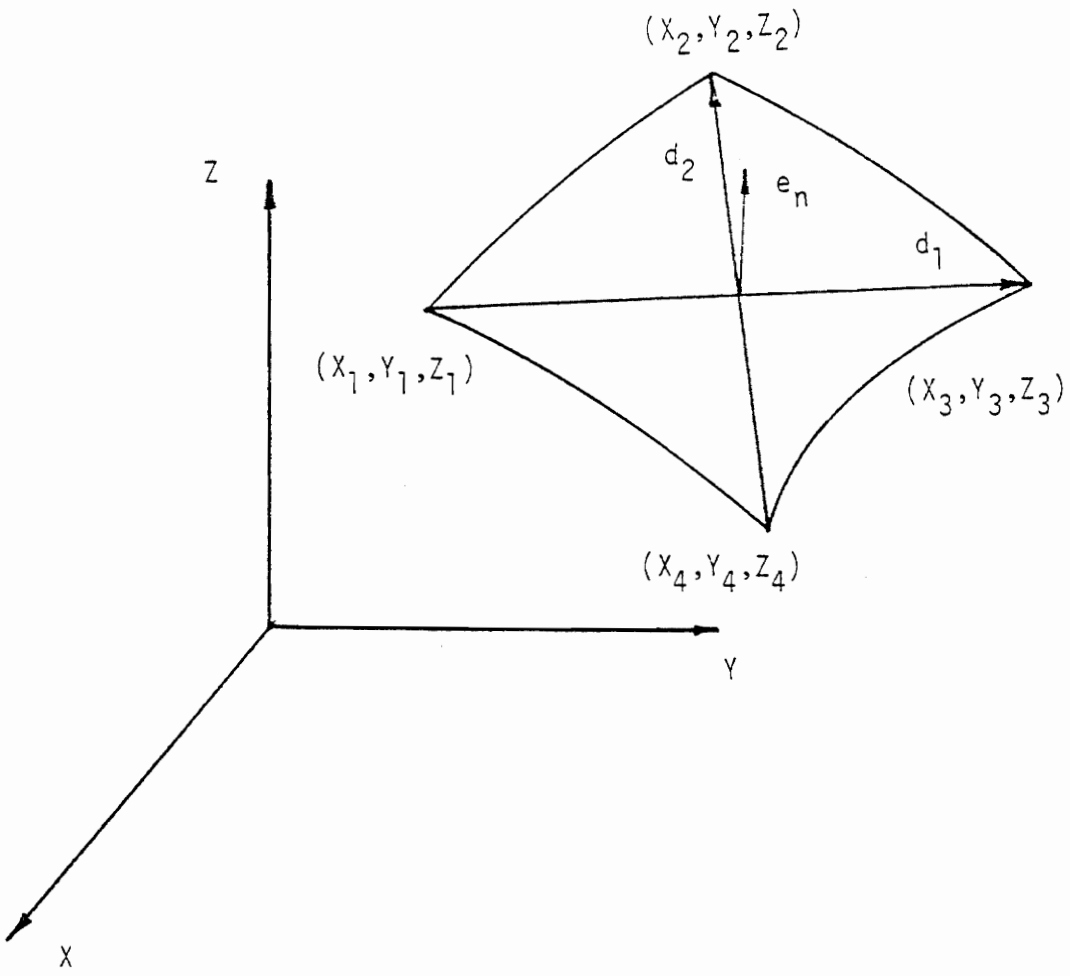

Figure 51. Panel geometry.

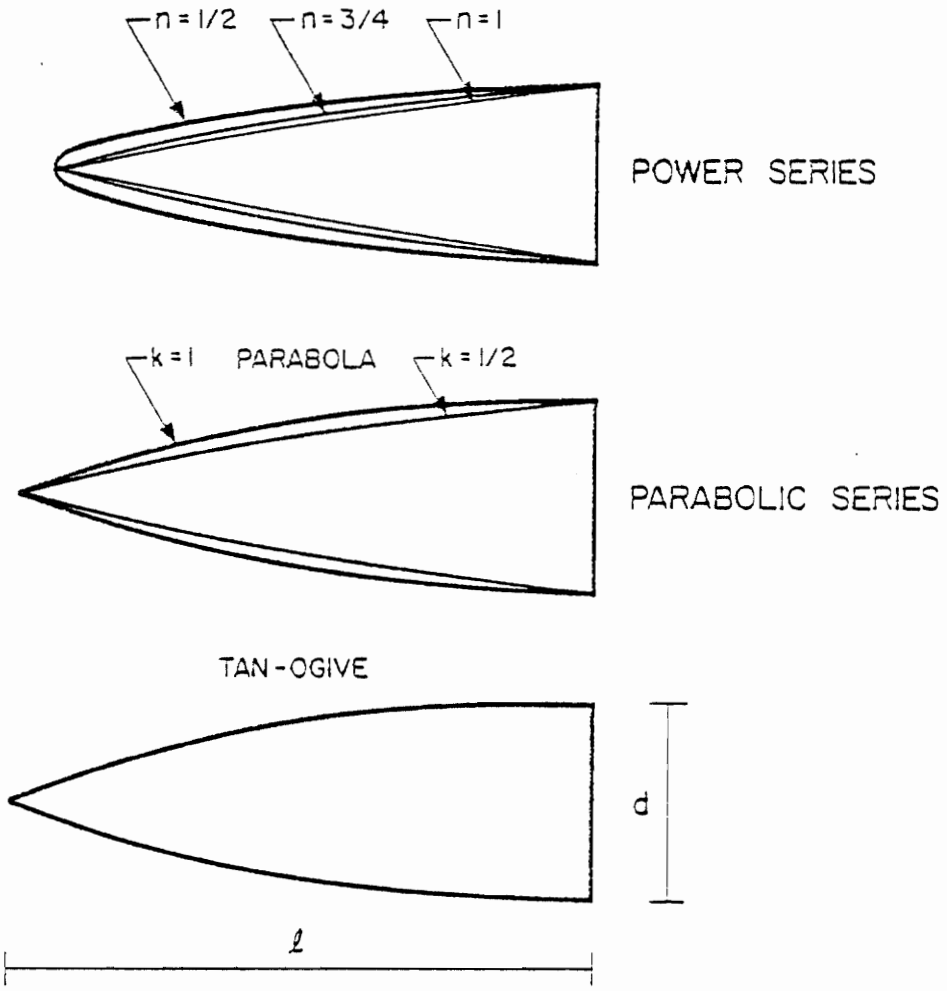

Figure 52. Different body-nose shapes.

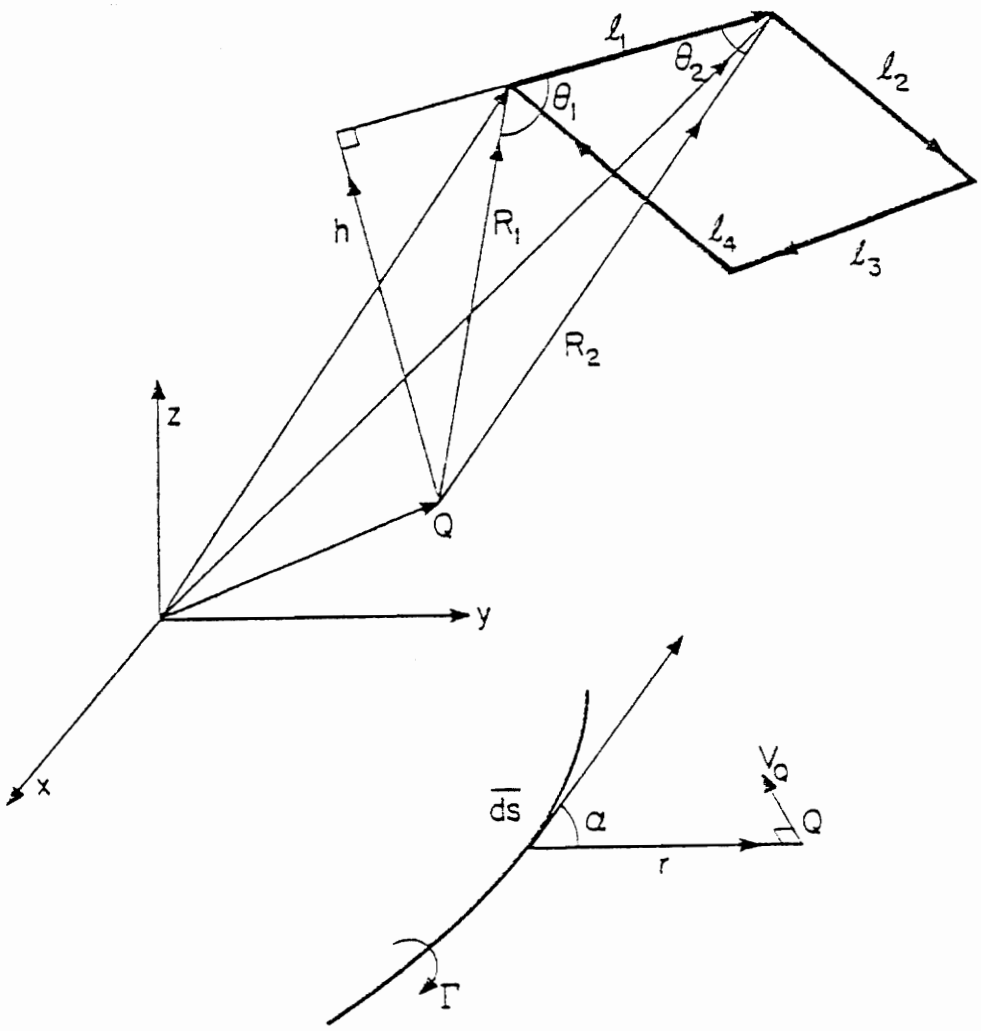

Figure 53. Parameters for the induced velocity calculation.

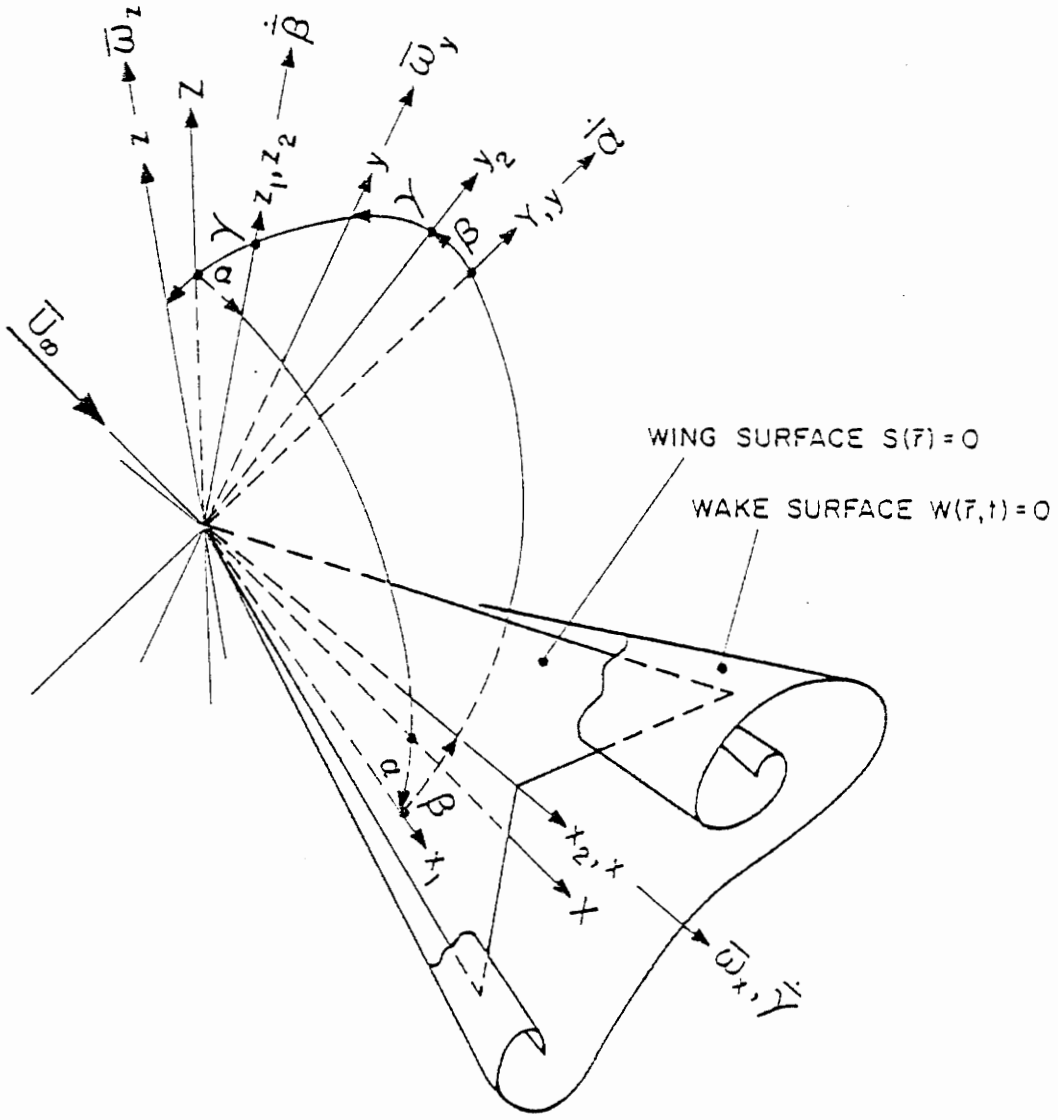

Figure 54. Wing-fixed frame of reference (xyz) and Euler's angles (α,β,γ).

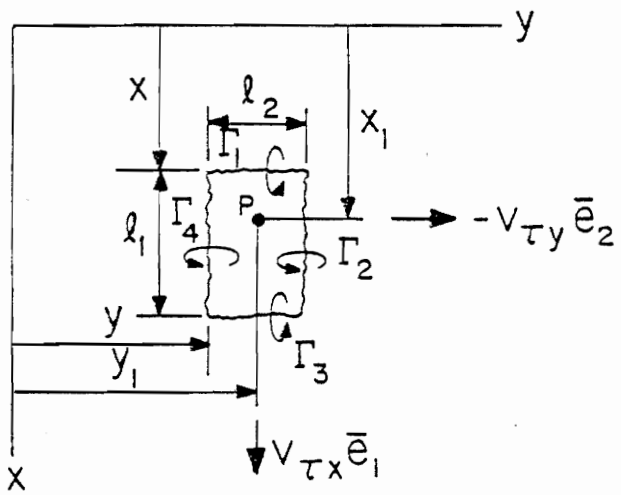

Figure 55. Induced tangential velocities.

VITA

The author was born in Cairo, Egypt in February 1947. He attended public schools in Cairo, Egypt from 1952 until 1963. In September 1963 he enrolled at Cairo University where he received his B.S. in Aeronatical Engineering in June 1968. During the period from 1969 until 1974 he worked at Helwan Aircraft Factory as a research engineer. In September 1974 he enrolled at Virginia Polytechnic Institute and State University where he received his M.S. degree in Engineering Science and Mechanics in March 1976 and has since been working toward his Ph.D. degree.

The author is a member of AIAA and the Sigma Xi North American Research Society.

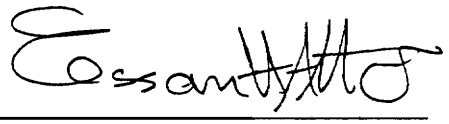

ESSAM H. ATTA

NONLINEAR AERODYNAMICS OF WINGS AND WING-BODY COMBINATIONS

by

ESSAM H. ATTA

ABSTRACT

A modified vortex lattice method is developed to solve for the nonlinear three-dimensional unsteady incompressible flow over delta wings. Symmetric motions (pitching, heaving) and asymmetric motions (roll, yaw) are considered. Then the method is generalized to treat the nonlinear three-dimensional steady flow for bodies and wing body combinations. Numerical examples include variety of shapes and comparison with existing experimental data and other numerical methods over a wide range of angle of attack shows good agreement. For bodies alone the results deteriate downstream of the separation region, while for wing-body combinations the agreement with the experimental data is good as long as the body separation effect is not large. The developed computer codes should provide a useful tool in the design of aircraft and missiles.